2012

FUNCTIONALIZED SILICA MATERIALS AND MIXED-MATRIX MEMBRANES FOR ENVIRONMENTAL APPLICATIONS

Noah Daniel Meeks
University of Kentucky, noahmeeks@uky.edu

STUDENT AGREEMENT:

I represent that my thesis or dissertation and abstract are my original work. Proper attribution has been given to all outside sources. I understand that I am solely responsible for obtaining any needed copyright permissions. I have obtained and attached hereto needed written permission statements(s) from the owner(s) of each third-party copyrighted matter to be included in my work, allowing electronic distribution (if such use is not permitted by the fair use doctrine).

I hereby grant to The University of Kentucky and its agents the non-exclusive license to archive and make accessible my work in whole or in part in all forms of media, now or hereafter known. I agree that the document mentioned above may be made available immediately for worldwide access unless a preapproved embargo applies.

I retain all other ownership rights to the copyright of my work. I also retain the right to use in future works (such as articles or books) all or part of my work. I understand that I am free to register the copyright to my work.

REVIEW, APPROVAL AND ACCEPTANCE

The document mentioned above has been reviewed and accepted by the student's advisor, on behalf of the advisory committee, and by the Director of Graduate Studies (DGS), on behalf of the program; we verify that this is the final, approved version of the student's dissertation including all changes required by the advisory committee. The undersigned agree to abide by the statements above.

Noah Daniel Meeks, Student

Dr. Dibakar Bhattacharyya, Major Professor

Dr. Stephen Rankin, Director of Graduate Studies

FUNCTIONALIZED SILICA MATERIALS AND MIXED-MATRIX MEMBRANES FOR ENVIRONMENTAL APPLICATIONS

DISSERTATION

A dissertation submitted in partial fulfillment of the requirements for the degree of Doctor of Philosophy in the College of Engineering at the University of Kentucky

By

Noah Daniel Meeks

Lexington, Kentucky

Director: Dr. Dibakar Bhattacharyya, Alumni Professor of Chemical Engineering

Lexington, Kentucky

2012

ABSTRACT OF DISSERTATION

FUNCTIONALIZED SILICA MATERIALS AND MIXED MATRIX MEMBRANES FOR ENVIRONMENTAL APPLICATIONS

Functionalized silica materials are synthesized for various environmental applications. The overall objective is functionalization with sulfur-containing moieties for mercury sorption and as a platform for nanoparticle synthesis. The first objective is quantifying this functionalization for various silica platforms. The second objective is development of effective mercury sorbents, for both aqueous mercury and elemental mercury vapor. Third, those sorbents are incorporated into mixed matrix membranes (MMM) for aqueous mercury sorption. Fourth, functionalized silica materials are developed as platforms for the synthesis of reactive metal nanoparticles (NP) for the degradation of trichloroethylene.

Thiol -functionalized silica is used as a sorbent for aqueous mercury, and a novel functionalized material (thiol-functionalized silica shell surrounding a carbon core) has been developed for this application. Total capacity and kinetics of aqueous mercury sorption were determined. The silica-coated carbon was functionalized with thiol and sulfonate moieties for regeneration under mild conditions. Finally, the sorbent particles were incorporated into polysulfone to form a mixed matrix membrane (MMM) for toxic metal capture under convective-flow conditions. High loadings (up to 50% particles, base particles of ~80 nm) were achieved in the MMM. The particles are well-dispersed which can lower mass transfer resistance to the sorption sites. The MMM also imparts several practical advantages such as ease of sorbent handling.

Silica functionalized with tetrasulfide silane is used for mercury vapor sorption. Sorption kinetics and dynamic capacity depend upon pore structures of the functionalized material. The particles are thermally stable and exhibit a glass transition in the tetrasulfide silane coating, with high total sorption capacity achieved by addition of copper sulfate. Temperature effects on mercury sorption indicate a chemisorptive mechanism.

Silica particles functionalized with sulfonate moieties were used as a platform for the synthesis of dispersed iron nanoparticles. These NP are applied for degradation of trichloroethylene (TCE), a persistent, toxic, and widespread pollutant. The particles were stabilized against agglomeration. Natural product reducing agents, such as ascorbic acid,

adsorb to the particle surface and can protect against oxidation. These particles were demonstrated for the reductive as well as oxidative degradation of TCE.

KEYWORDS: mercury, iron nanoparticles, silanization, trichloroethylene, mixed matrix membranes

Noah D. Meeks

Student's Signature

March 20, 2012

Date

FUNCTIONALIZED SILICA MATERIALS AND MIXED-MATRIX MEMBRANES FOR ENVIRONMENTAL APPLICATIONS

By

Noah Daniel Meeks

Dibakar Bhattacharyya

Director of Dissertation

Stephen Rankin

Director of Graduate Studies

March 20, 2012

Date

Acknowledgements

I would like to thank Professor Dibakar "DB" Bhattacharyya for his patient counsel, advice, and research direction over the past years. He has taught me so much, not only about chemical engineering, but about professionalism and research practice. Although I have sometimes learned slowly, his efforts have not been completely in vain. His dedication to graduate student education and the chemical engineering profession is unparalleled.

I also thank my dissertation committee for their service and the assistance they have given in various capacities through my time as a graduate student: Professor Stephen Rankin, Director of Graduate Studies; Associate Professor Thomas Dzuibla; Professor David Atwood; and Professor John Selegue. I especially thanks Prof. Rankin and Prof. Selegue for their classes on advanced materials and transition metal chemistry; and Profs Rankin, Dzuibla, and Selegue for assistance provided to our group in their labs.

Besides those of my committee, many other professors have shaped and contributed to my graduate education through both teaching courses and research advice. I am especially appreciative of our Department Chairman, Prof. Douglass Kalika, as well as Professors A.K. Ray, Tate Tsang, Barbara Knutson, John Balk, Kim Anderson, and Richard Eitel, with whom I have taken classes and/or used their lab facilities.

Many DB Lab group members have helped me through the years, especially Dr. David Meyer early in my graduate studies. Working in the DB Lab has given me the opportunity to work alongside some very skilled scientists for which I am grateful, especially our current post-doctoral fellow, Dr. Vasile Smuleac, as well as my classmate and labmate, Dr. Scott Lewis.

I also thank those organizations which have financially supported my research: J.M. Huber Corporation, NEI Corporation, and National Institute of Environmental Health Sciences. Analytical support has been given by Tricia Coakley and John May of UK Environmental Research Training Laboratory; Dr. Jia Ye, Dr. Alan Dozier, and Larry Rice of UK Electron Microscopy Center; and the mercury vapor detector is generously loaned by the U.S. Environmental Protection Agency.

Finally, I want to thank my family, and especially my parents, Doug & Dr. Piper Meeks, for their encouragement and love through this process. I have learned much about practical environmental solutions from my father, and mother gave me a great deal of advice on finishing the dissertation process based on her own experience as well.

Table of Contents

List of Tables

List of Figures

1. Objectives

The development of new functionalized materials for various chemical engineering applications, especially environmental applications, is an important research area. As both public concerns are heightened and regulatory standards are tightened, new materials are needed which incorporate chemical functionalities toward increased performance. This dissertation describes the synthesis, characterization, and application of various functionalized silica platforms, with specific objectives listed below. Many of these objectives are driven by inadequacies of current technology.

The layout of this dissertation is given as follows. There are five results and discussion chapters (Ch 4-8) which describe experimental results, put them in the context of previous work and scientific advancement, and include specific conclusions. Prior to that, there are background and experimental chapters. Chapter 2 ("Background") is divided into five sections, each of which gives background information corresponding to the results and discussion chapters of the same names as each section. Chapter 3 contains the experimental details, which is similarly divided into five corresponding sections. At the end of the document, there is a final Chapter 9 which briefly summarizes the key conclusions and scientific advancements.

The five results and discussion chapters are briefly described here with the objectives following. Chapter 4 discusses the silica functionalization fundamentals including the reactions and determining the extent of functionalization. Chapter 5 discusses aqueous mercury sorption using a functionalized silica-carbon black platform. Chapter 6 discusses the use of these functionalized silica platforms in mixed matrix membranes for aqueous mercury sorption. Chapter 7 describes elemental mercury vapor

sorption using functionalized silica and functionalized copper-doped silica. Chapter 8 describes the use of functionalized silica as a platform for reactive metal nanoparticle synthesis, for application towards the dechlorination of trichloroethylene, a persistent and prevalent groundwater contaminant, and also describes some alternative synthetic methods for environmentally important reactive and catalytic nanoparticles.

The specific objectives are as follows:

Chapter 4: Functionalization Fundamentals

- to quantify the extent of silica functionalization for an environmental application with various silica types
- to quantify the extent of silica functionalization with silanes for two different environmental applications
- to describe the nature of the functionalized silane layers on silica particles
- to demonstrate the role that silica functionalization plays in mercury vapor sorption

Chapter 5: Aqueous Mercury Sorption

- to characterize functionalized silica-carbon particles for potential mercury sorption applications
- to quantify equilibrium sorption of mercury using functionalized particles
- to demonstrate the role of solution pH and sorbent agglomerate size play in sorption capacity and kinetics
- to demonstrate regenerable functionalization schemes and propose future strategies for their optimization

Chapter 6: Mixed matrix membranes (MMM) for mercury sorption

- to synthesize silica-polymer MMM using the phase-inversion method
- to analyze MMM behavior including flux and sorption capacity at various sorbent loadings

Chapter 7: Elemental Mercury Vapor Sorption

- to describe the synthesis of functionalized silica for the sorption of elemental mercury vapor, for potential power plant applications
- to quantify the total and "dynamic" sorbent capacity
- to describe the effect of temperature on sorbent
- to determine the sorption products and test for disposal compatibility

Chapter 8: Silica as a Platform for Nanoparticle Synthesis

- quantify sulfonate functionalization of silica
- synthesize iron nanoparticles (Fe NP) on a sulfonate-functionalized silica particle platform
- to describe alternative strategies for Fe NP synthesis using "green" reducing agents
- to show reactivity toward environmentally-important compounds such as TCE, using both oxidative and reductive approaches

2. Chapter Two: Introduction

This chapter introduces the specific environmental applications for which functionalized silica materials have been used and gives some background information for the various sections of this dissertation. The five sections of this chapter correspond to the five sections of Chapter 3 (experimental), and then to each respective discussion chapter (4-8).

The various silica materials used are described in Table 2.1. Some of these materials are unfunctionalized silica, which were functionalized in the lab as described in Chapter 3 and discussed in the respective chapters. Others were functionalized by the manufacturer and the sulfur content is given in the table, with further discussion in the respective chapters. Sulfur-containing silanes used for functionalization are described in Table 2.2.

2.1 Fundamentals of Silylation

2.1.1 Silica Particle Synthesis

Synthetic silica particles, which is the only type considered in this study, are prepared through one of three basic methods, reviewed by Vansant[1]: sol-gel, precipitation, or thermal method. Sol-gel method synthesis involves the acid- or base-catalyzed hydrolysis of the silica precursor (such as $Si(OH)_4$ or $Si(OR)_4$) followed by condensation into primary particles. These then gradually aggregate to produce a viscous solution and eventually a disordered polymeric hydrogel (when water is the condensation byproduct) or alcogel (when an alcohol is a byproduct). The formation of various sol-gel structures is impacted by factors such as silica precursor structure, pH, reactor composition, water content, etc.[2] This gel is often highly porous as it has arisen by the

Table 2.1 Silica morphology and composition.

*for sorbents functionalized by the manufacturer
**Ludox colloidal particles are non-porous, but capillary condensation occurs due to interparticle spacing in dried agglomerates of colloidal particles.
***SCC-3 sorbent used in a variety of agglomerate size ranges (Figure 5.1)

Silica designation	Description	BET surface area (m^2/g)	BJH average pore diameter (nm)	Agglomerate diameter (μm)	Weight % S*	Chapter
Silica A	silica gel	206	9.6	3.7	NA	4
Silica B	silica gel	484	2.9	3.3	NA	4
Si-1	silica gel	344	2.9	20	6	7
Silica D	silica gel	585	NA	3.7	NA	8
Ludox	dried colloidal silica	76	7.1**	NA	NA	4, 5, 8
SCC-0	silica-coated C	209	NA	45-850	<0.38	5, 6
SCC-1	thiol-coated C	126	NA	45-850	4.1	5, 6
SCC-2	thiol-silica-coated C	132	NA	45-850	3.0	5, 6
SCC-3**	thiol-silica-coated C	83	NA	45-850	3.7	5, 6

Table 2.2 Silanes used for silica functionalization.

acronym	structural formula	CAS #	molar mass
MPTMS	$Si(OCH_3)_3CH_2CH_2CH_2SH$	4420-74-0	196.34
S4	$(CH_3CH_2O)_3SiCH_2CH_2CH_2SSSSCH_2CH_2CH_2Si(OCH_2CH_3)_3$	40372-72-3	538.95
THSPS	$Si(OH)_3CH_2CH_2CH_2SO_3H$	70942-24-4	202.26

random aggregation of colloidal primary particles. In contrast to sol-gel silica, precipitated silica is prepared by the addition of salts or an increase in pH to the colloidal solution, so that particles precipitate at various stages of aggregation. Thermal or pyrogenic silica is prepared by oxidation of highly pure $SiCl_4$ in the presence of H_2. If the primary particles link into chains, this produces fumed silica. Oxidation in an arc furnace produces non-porous secondary particles called arc silica, and oxidation in plasma gives solid colloid-sized particles.

2.1.2 Silica Morphology Characterization

Synthetic silica is often characterized by the presence of a number of pores, which are described as macropores (> 50 nm diameter), mesopores (2 – 50 nm), or micropores (< 2 nm), according to IUPAC designation.[3] Nitrogen at its saturation temperature and pressure (77 K at 1 atm) can be used to determine the pore and surface characteristics of an unknown silica (and many other materials) based on adsorption isotherms; N_2 adsorbs as a liquid at less than its saturation pressure inside of pores, and the isotherm of this adsorption gives key insights into the nature of the pore morphology. Inside macropores, multilayer adsorption occurs, and capillary condensation only occurs at relative pressure near unity (as the effective pore diameter has narrowed due to the multilayer adsorption of nitrogen). Micropores gradually fill with liquid by capillary condensation, but they are completely filled at relative pressures much less than unity. Mesopores also experience multilayer adsorption as do macropores, but capillary condensation occurs at much lower relative pressures because the pores are narrower. Mesopores also demonstrate a hysteresis as desorption of N_2 occurs at lower relative pressures than adsorption, due to the geometry of the pore mouth ("ink bottle effect").

Smaller pore diameter allows for condensation within the pores at lower relative pressures, which can be described by the Kelvin model of pore condensation, given as[4]

$$\ln\frac{P}{P_s} = -\frac{2\gamma\bar{V}}{rRT}, \qquad (2.1)$$

where P/P_s is relative pressure, γ is surface tension of adsorbed liquid, r is pore radius, R is gas constant, T is temperature, and $\bar{V}$ is the molar volume of adsorbed liquid. Kelvin's model was modified by Barrett, Joyner, and Halenda[5] to render the classic BJH model of pore size distribution, assuming all cylindrical pores. They considered that in larger pores multilayer adsorption first takes place to shrink the effective pore diameter; capillary condensation then occurs after the radius has shrunken by the thickness *t* of the adsorbed multilayer. The BJH model is given[4] as

$$\ln\frac{P}{P_s} = -\frac{2\gamma\cos\theta}{RT(\rho^l - \rho^g)(r_p - t)}, \qquad (2.2)$$

where θ is contact angle of adsorbate against the pore wall (a measure of fluid-wall vs. fluid-fluid interactions), ρ^l is liquid density of the bulk adsorbate, ρ^g is the vapor density of the adsorbate (both at the adsorption temperature), and r_p is the actual pore radius.

High surface area, which arises from the porous structure, is an important parameter in the use of synthetic silica. The most common method of calculating surface area is the Bruanuer, Emmett, and Teller (BET) model,[6] which assumes that multilayer adsorption takes place by one layer adsorbing to a previously adsorbed layer. BET method assumes a homogeneous surface, no interaction among adsorbate molecules in the same layer, a heat of adsorption is equal to the heat of condensation except in the first

layer, that the conditions of condensation do not change after the first layer, and that there are infinite layers at the saturation pressure. In general, these assumptions are not regarded to be completely accurate for synthetic silica particles, but the model has been commonly used so that the BET model is regarded as a standard method of characterizing surface area. The BET equation is given as[1]

$$\frac{1}{W\left(\frac{P}{P_S}-1\right)}=\frac{1}{W_m C}+\frac{C-1}{W_m C}\left(\frac{P}{P_S}\right), \qquad (2.3)$$

where W is mass of adsorbate at a certain relative pressure, W_m is the mass of absorbate required to impart monolayer surface coverage, and C is a constant. A plot of $\frac{1}{W\left(\frac{P}{P_S}-1\right)}$ vs. $\left(\frac{P}{P_S}\right)$ yields a straight line of intercept $\frac{1}{W_m C}$ and slope $\frac{C-1}{W_m C}$, making the determination of both W_m and C straightforward. The BET surface area (S_{BET}) can then be determined using

$$S_{BET}=\frac{W_m N_A A_c}{M}, \qquad (2.4)$$

where N_A is Avogadro's number, M is the adsorbate molecular mass, and A_c is the adsorbate cross sectional area. For N_2, A_c has conventionally been taken (based on packing arrangements) to be 0.0162 nm^2. (Although a recent study[7] contrasting surface areas calculated from SEM images and those from N_2 led to the proposal that for adsorption on silica, a more accurate value is A_c = 0.0135 nm^2.)

The extent to which silica can be functionalized and used as an adsorbent is related to its specific surface area and pore structure. However, functionalization of

higher surface area silica does not necessarily lead to more functional groups because microporous surface area may not be accessible to larger silanes, and functional groups near pore openings may block further diffusion of silane into the pores.[8] Similarly, functionalized silica with a higher total specific surface area do not necessarily have the highest chemisorptive capacity, as silanes may block pore openings for the adsorbate or microporous surface area will have no chemisorptive sites because it was not functionalized. The type of surface area, whether microporous, macroporous, or mesoporous, plays an important role in determining the specific number of functional groups and the adsorption capacity than the total surface area.

2.1.2 Quantification of Surface Hydroxyl Groups

The silica surface is covered with surface hydroxyl groups, known as silanol (SiOH) groups, which undergo silylation reactions with a number of compounds to yield functionalized silica particles. The quantification of silanol groups, often reported as silanol number α_{SiOH} (number SiOH/nm^2 surface area), is an important part of studying silylation reactions. Silanol number is dependent upon temperature and atmosphere, as silica is first dehydrated (removal of physisorbed water) and then dehydroxylated (condensation of surface silanol groups to form siloxane (Si-O-Si) bridges) upon heating. Methods of experimentally determining α_{SiOH} are either based on direct measurement of the groups, or reaction of silanol with some other compound and measurement of that probe compound. Direct measurement methods include infrared spectroscopy, with various O-H stretching vibrations assigned to 3750-3400 cm^{-1}; and Si-O-H bending assigned[9] to 970 cm^{-1}. However adsorbed water also is assigned to many of the bands (except at 970 cm^{-1}) making measurement impossible without complete drying, which

would alter the morphology of the silica (pore collapse) and possibly dehydroxylate some silanol. It is therefore difficult to directly compute α_{SiOH}, but comparisons of the same silica material after having undergone the same thermal and solvent treatment can be used to quantify percentage of the silanol groups that have reacted. Methods of indirect silanol measurement include silanol adsorption of chlorodimethylsilane[10] or pyridine[11], and quantifying this adsorption using a variety of techniques. Many different values have been reported for the silanol number of various silica samples treated at different conditions. However Zhuravlev[12] reviewed many types of silicas with a wide range of morphologies, and found that for fully hydroxylated silicas, the silanol number was near constant at 4.6 SiOH/nm^2.

2.1.3 Silylation (Functionalization) Reactions

Silica materials (gels, colloids, glasses, etc) are easily functionalized with nearly any desirable surface functionality for a variety of applications. The heart of silica surface functionalization involves the formation of covalent bonds between silica surface hydroxyl groups (silanol groups) and the Si center of a chloro- or alkoxysilane molecule (Figure 2.1). The resulting surface Si-O-Si-R linkages provide good thermal and chemical stability[13] (also due to the coatings which potentially increase hydrophobicity [14,15]). These silylation reactions have been used to form functionalized silica particles for chromatography columns,[16, 17] catalysts,[18,19] advanced drug delivery,[20] as well as functionalized sorbents. Silica functionalization of ordered mesoporous materials has been recently reviewed.[21]

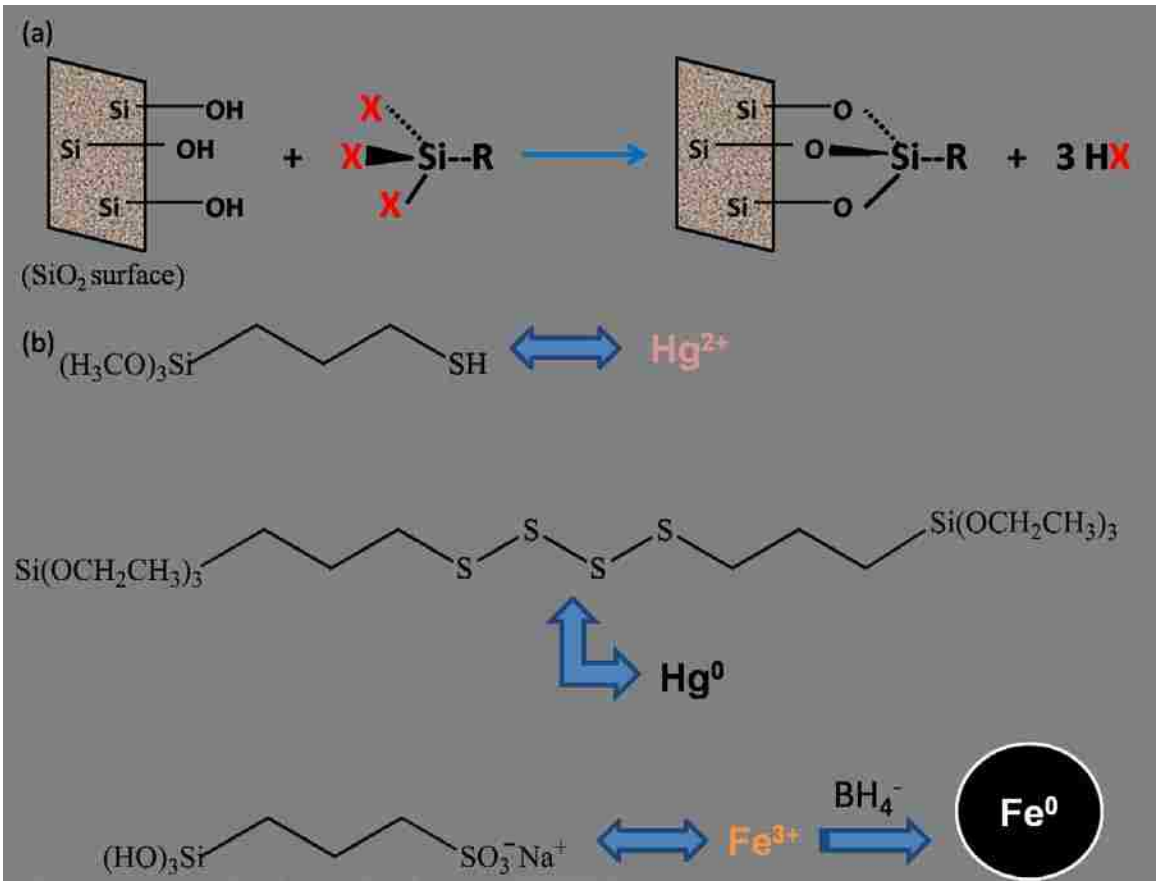

Figure 2.1 General functionalization schemes.
(a) Schematic reaction of silica surface functionalization. X represents halide, hydroxide, or alkoxide leaving group. (b) Silanes used in this study for silica functionalization, and the associated environmental applications for sorption or as a platform for nanoparticle synthesis.

Two different routes to achieve the functionalized particles are available (Figure 2.2). Silylation can be done at the monomer level, and then the functional monomers are co-condensed with silica precursors to form functional particles[22, 23] or the silanol groups of already-formed silica particles can be functionalized. The latter strategy (sometimes called grafting) is used in this study. Two silylation mechanisms have been proposed.[24,25] The first is the widely accepted sol-gel mechanism, in which moisture (either added or adsorbed to silica particles stored under atmospheric conditions) hydrolyzes the chloro- or alkoxy- leaving groups of the silane, followed by condensation with surface silanol groups.[26, 27] One recent study[28] has shown that it is even possible to exploit this mechanism in a solventless silylation process. The second mechanism that has been proposed is a direct one-step nucleophilic substitution mechanism believed to operate during vapor phase silylation in a dry atmosphere.[29]

2.2 Aqueous Mercury Sorption

2.2.1 Adsorption of Aqueous Mercury

The efficient removal of aqueous mercury from contaminated water is a well-known challenge, due to toxicity of mercury[30] throughout the ecosystem. Various approaches have addressed this challenge, including precipitation, adsorption/ ion exchange, photocatalytic remediation,[31] phytoremediation,[32] and bioremediation[33] by genetically modified organisms (GMO).[34] Phytoremediation is used for contaminated soils and for large contaminated groundwater plumes, and often results in volatilization of elemental mercury into the atmosphere. Bioremediation and photocatalytic remediation are useful only to reduce organic mercury compounds to the elemental state, but the metal must still be recovered from the ecosystem, and in situ application of GMO

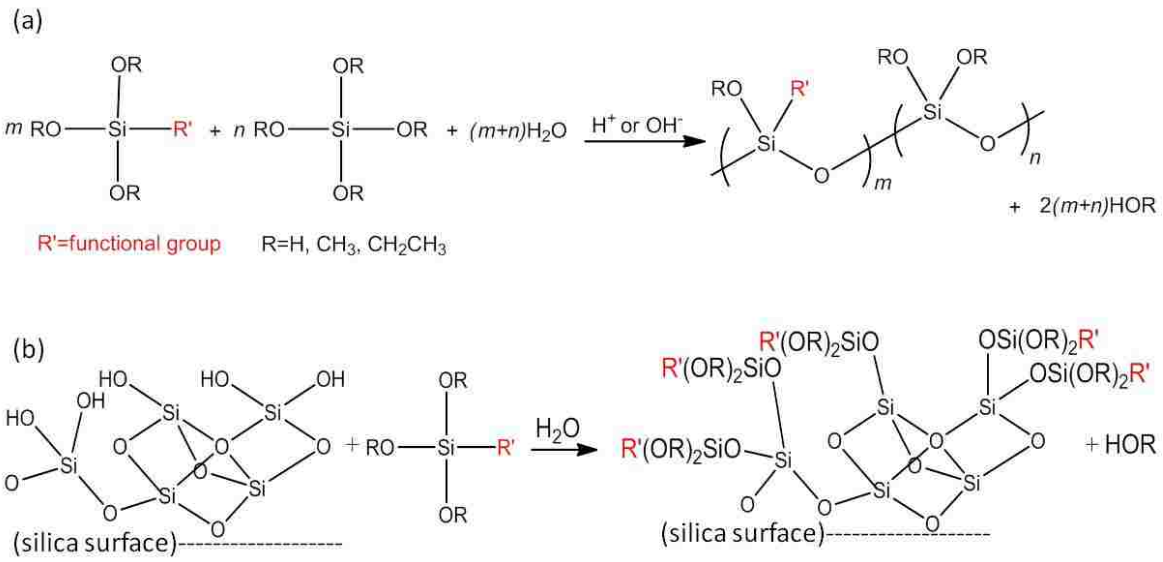

Figure 2.2 Two approaches for silica functionalization.
(a) condensation of silane monomers (b) surface functionalization or grafting after silica particle has been synthesized.

raises ecological concerns. Precipitation[35] has been shown effective for mercury removal, including the precipitation of mercury at very low concentrations.[36] In many situations, the solid precipitate must be removed in a secondary step such as ultrafiltration. Reviews of mercury removal from water have been recently published.[37]

Adsorption and/or ion exchange have become the preferred techniques, in cases where ex situ treatment is feasible, because the mercury is sequestered onto a sorbent particle. Activated carbon has been used but the capacity is low due to the physisorptive mechanism, prompting the development of materials with specific functionalized surfaces for mercury chemisorption.[38] Amines, amides, imines, and sulfur-containing functional groups on a variety of surfaces (metal oxides, fly ash, carbon, polymers, and gold) have been proposed.

2.2.2 Regeneration of Aqueous Mercury Sorbents

Another challenge for mercury removal is the regeneration of sorbent particles. Previous studies used a regenerating solution that dissolves mercury even from a very strong coordination, such as concentrated nitric acid[39], perchloric acid, or hydrochloric acid[40], or a more dilute acid mixed with thiourea[39, 41]. In another study where a urea moiety was the active sorption site, hot acetic acid was shown effective towards regeneration. A previous study in our lab indicated that functional groups such as cysteine and cystine can be regenerated at very mild conditions (pH = 3).[42] In this study, a different approach is used than previous work. Rather than modifying the regenerating solution for better removal of mercury, the sorbent itself is modified to allow for desorption of mercury under mild conditions. In this approach, both thiol and sulfonate

moieties are used. The mercury is less strongly adsorbed by the thiol moieties due to steric effects from the neighboring sulfonate moieties.

2. 3 Membrane Applications for Sorption

One limitation of using engineered sorbent particles is the mass transfer of sorbate. This challenge is not unique to mercury removal and affects many separation processes. Convective flow through engineered membranes often demonstrates more efficient mass transfer than packed beds. However, functionalizing a membrane with an appropriate chemisorptive moiety remains a challenge, so we demonstrate a mixed matrix membrane (MMM) approach. MMMs incorporate the adsorbent particle within an inert polymer matrix, so that the effectiveness of chemisorptions on the sorbent particle is combined with the efficiency of membrane operations. Recent work has shown MMM, including polysulfone/silica MMM[43], effective for various gas separations[44], and our lab has demonstrated the application of polysulfone/silica MMM for high-value aqueous silver recovery applications.[45]

The use of MMM with this sorbent bring a number of advantages for mercury sorption. First, the membrane serves as a platform for the efficient dispersion of the sorbent particles, which allows more active sorption sites to be occupied by sorbate mercury ion. Second, by having the membrane in a polymeric matrix, there is no additional filtration unit operation required after sorption. The contaminated feed is passed into the MMM, and the mercury is retained within the MMM, while the mercury-lean permeate exits the membrane unit. Third, the contaminated particles are retained within the polymer matrix for facile disposal. The sorption capacity and effectiveness of the MMM are seen in the various breakthrough curves which are dependent upon

membrane parameters (thickness t, pressure P, porosity ε, tortuosity τ) as well parameters important for conventional sorption (pH, temperature T, sorbent loading). Another advantage is the ability to use milled sorbent particles (shown to have a higher initial sorption rate). These must be incorporated into MMM as the pressure drop would be too large to use these fine particles in a packed column.

2.4 Elemental Mercury Vapor Sorption

The growing needs of electrical energy for developing nations, coupled with efforts to move away from a petroleum-based energy supply, has led to the global construction of many new coal-fired power plants. This has exacerbated environmental concerns about the release of elemental mercury into the atmosphere, which is harmful not only through direct inhalation by humans, but which re-enters the ecosystem through various routes. Many mercury species present are removed in existing pollution-control devices. Oxidized mercury is often removed in the electrostatic precipitator (ESP), and particle-bound mercury can be removed in baghouse filter devices. However, about 60% of the mercury is elemental vapor (Hg^0), for which additional control technology is needed.[46]

2.4.1 Sorption Using Sulfur-functionalized Silica

The conventional method of mercury control is activated carbon sorption due to the high specific surface area. This is a well-known sorbent which is used for the removal of many contaminants and distasteful compounds from water, as well as the primary sorbent for removal of contaminants from gases. However, activated carbon for mercury vapor sorption has some drawbacks. First, the physisorptive mechanism inherently decreases the capacity at higher temperatures, which would typically be

present in power plant applications. Second, other species present such as SO_3 interfere with the sorption onto activated carbon.[47] Some of the problems have been addressed with the use of brominated activated carbons, which oxidize the mercury at higher temperatures and alter the sorption mechanism. Finally, there are disposal issues with activated carbon which could eliminate an important cost-recovery route for the power plant operators. Typically, fly ash is removed in the baghouse filter and sold as a cement additive, but the addition of carbon renders its mechanical properties obsolete. Therefore, the development of a non-carbon sorbent (such as silica) is an important objective for the power industry to remove mercury and preserve a key cost-recovery stream.

2.4.2 Effect of Temperature on Sorption

The role of temperature in the efficacy of mercury capture by sorbents is a very important research area. In 1995, it was published[48] that Hg vapor capture on the surface of activated carbon in the presence of fly ash was heavily dependent upon temperature, with the maximum adsorption at about 200 °C. While the mechanisms of mercury capture on activated carbon and functionalized silica may be different, temperature is expected to play a role in both capture processes.

2.5 Reactive and Catalytic Nanoparticle Synthesis

2.5.1 Nanoparticle Synthesis Methods

The use of catalytic and reactive nanoparticles in various environmental applications is an emerging field; however, their use has been limited because of several practical difficulties. Among these, the major ones are NP aggregation and surface deactivation (through oxidation or passivation). This is especially true for magnetic and

electropositive zero-valent metal NP, such as iron.[49] Various methods for Fe NP synthesis have been described in literature,[50,51] one of the most common being the reduction of inorganic iron salts using sodium borohydride[52] (2.5).

$$Fe(H_2O)_6^{3+} + 3BH_4^- + 3H_2O \rightarrow Fe^0 + 3B(OH)_3 + 10.5H_2 \quad (2.5)$$

Naturally occurring reducing agents can be used in the place of borohydride, especially in the synthesis of iron nanoparticles with the co-reduction of a secondary metal. Recently, the use of ascorbic acid (vitamin C) has been proposed[53] for the co-synthesis of iron and palladium, eliminating the need for post-coating step for the formation of bimetallic NP. Our lab has also recently published the use of polyphenol reduced and stabilized iron particles supported on a functionalized membrane.[54]

Because surface chemistry of nanoparticles plays a prominent role in their application, attempts have been made to stabilize the nanoparticles through chelating ligands, which impede particle agglomeration.[55] The decreased agglomerate size and the presence of the adsorbed polyligands may enhance nanoparticle transport, in some important applications such as groundwater remediation.[56] Various ligands such as polysugars (interacts through hydroxyl groups), carboxymethyl cellulose (CMC)[57] (interacts through both hydroxyl and carboxylate groups), polystyrene sulfonate (PSS),[58] and PSS-containing block co-polymers,[59] have been successfully implemented in the stabilization of Fe NP. A variety of strategies for iron oxide NP stabilization have also been recently reviewed.[60] One study[61] demonstrated the use of metal-carbon bonds for stabilization in non-aqueous solvents, where decylbenzene attached to the surface acts as both a phase transfer agent from the aqueous phase (in which particle is synthesized) to the organic phase in which it is used. Another study[62] showed that non-metal

homogeneous nanoparticles may be stabilized by a lack of shear forces during particle formation.

2.5.2 Nanoparticles Synthesized on Platforms

While the chelating ligands do impede particle aggregation, Fe NP have also been successfully synthesized on various platforms for ease of application. Support membranes such as PVDF have been coated with poly(acrylic acid), and this functionalized membrane has been used to immobilize iron ions which are reduced to iron nanoparticles.[63] Activated carbon has been used to support Fe/Pd NP for the destruction of chloroorganics in aqueous[64] as well as DNAPL phases.[65]

A silica platform offers potential advantages over polymers or activated carbon, and it is a well-known support for catalysts. Recently, an ordered mesoporous silica (SBA-15) was optimized for the synthesis of Bi[66] and Co[67] NP by incorporation of precursor salt within the pores. Also Pt NP were formed by the reduction of a precursor salt onto colloidal silica,[68] and both Au[69] and Ti[70] NP have been co-precipitated into sol-gel silica. For Fe NP, some very elegant work[71] has recently been published demonstrating the synthesis of hydrophobized silica particles loaded with Fe NP. In this case, the hydrophobized silica particles are synthesized by direct co-condensation of silane precursors (and simultaneous evaporation of iron salts) in an aerosol-assisted heating process, with the iron salts subsequently reduced to Fe NP using borohydride. A subsequent study indicated the enhanced transport of these materials through simulated aquifers due to decreased aggregation.[72]

In addition to co-condensation of silanes, the silica surface is covered in silanol (SiOH) moieties (typically ~ 3 SiOH/nm^2) which can be easily functionalized by

silanization (also called grafting). This is another advantage of silica over other platforms. In this case, the silica is functionalized with sulfonate groups which provide a strong ion exchange platform for ferric/ferrous ions. Alternatively a weak ion exchanger such as carboxylate could be used with the ferrous ions only. Although not addressed in this study, multiple functional groups could also be used for the synthesis of hydrophobic/hydrophilic nanodomains. The ability to incorporate multiple functional groups onto a single platform is a further advantage of silica.

2.5.3 TCE Dechlorination

An important application of zero-valent iron is for the detoxification of trichloroethylene (TCE), a very prevalent groundwater pollutant which is both persistent and toxic. Physical as well as chemical oxidation and reduction have been demonstrated for remediation of TCE. A common physical strategy is air stripping,[73] which may or may not be followed by TCE sorption onto activated carbon. Oxidative strategies include biological oxidation or in situ chemical oxidation (ISCO) techniques, such as Fenton's reaction to generate hydroxyl radicals (OH•).[74] Our lab recently demonstrated the use of modified Fenton's reaction for ISCO; using citrate as a chelating agent for the ferrous/ferric ions to overcome difficulties of conventional Fenton's reaction.[75]

Reduction of TCE can occur by either direct electron transfer or by hydrogenation,[76] and both reactions have been carried out using various catalytic schemes. Although direct electrical current has been shown[77] effective towards TCE reduction, iron is commonly used as an electron-transfer catalyst. Hydrogenation has been carried out by traditional hydrogenation catalysts such as Pd, Ni, Pt, etc., where the hydrogen is supplied. Because the supply of hydrogen to contaminated underground

field sites is generally considered impractical, bimetallic catalysts have recently been developed, where a primary metal such as Fe reduces water to hydrogen through corrosion, thus supplying the needed reactant for a nearby hydrogenation catalyst located on the particle surface. Fe/Pd and Fe/Ni[78] bimetallic particles have been shown to be most efficient among various bimetallic combinations.[79] The high surface area to volume ratio of nanoparticles, and the high prevalence of edge defects on nanoscale particles, has been demonstrated to be more effective catalysts than microparticle catalysts.[80]

3. Chapter Three: Experimental Methods

This chapter details the experimental methods for all the subsequent chapters of the dissertation. Each section of this chapter corresponds to subsequent chapters in which results, discussion, and experimental conclusions are given for these experiments. The final chapter of this dissertation (Chapter 9) describes the overall conclusions and scientific advancements of the dissertation.

3.1 Functionalization Fundamentals

3.1.1 Materials Used

Silica particles having various structure parameters given in Table 4.1 were obtained from J. M. Huber Corporation (Havre de Grace, MD) for Silicas A and B; Ludox colloidal silica (TM-50) was obtained from Grace Davison (Columbia, MD). Sulfur-containing silane reagents used were 95% 3-mercaptopropyltrimethoxysilane (MPTMS) or 95% bis[3-(triethoxysilyl) propyl]tetrasulfide (S4); which were obtained from Sigma-Aldrich, Inc., (St. Louis, MO) and Gelest, Inc. (Morristown, PA), respectively. Basic information on these silicas are also given in Table 2.1 and on the silanes in Table 2.2 and Figure 2.1.

3.1.2 Silylation Procedure

Silica particles were functionalized by adding 2.5 g of particles and 0.9 mL of silane into a flask containing enough anhydrous ethanol to disperse the particles (*ca*. 50 mL). The mixture was heated to 80 °C to evaporate the ethanol, and the remaining moist silica was heated at 110 °C for at least 4 h in order to accomplish silylation. The particles were then washed with ethanol under vacuum filtration using a 0.45 μm filter membrane, and dried at 80 °C overnight.

3.1.3 Determination of Extent of Functionalization

Three methods are used to determine the extent of functionlization of the various silica particles using sulfur-containing silanes. First, Fourier transform infrared spectrometry (FTIR) was used: a small amount (ca. 5-10 mg) of the functionalized silica was ground with KBr and pressed into a pellet. A KBr pellet containing a similar amount of unfunctionalized silica was also prepared, and the spectra of both were acquired using a Thermo-Nicolet Nexus 470 spectrometer running Omnic software.

The second method of determining the extent of silylation is to use thermogravimetric analysis (TGA) to determine the silane weight percent of the functionalized particles. The TGA plots of the unfunctionalized particles are compared to those of the functionalized particles in order to properly account for the weight loss due to moisture evaporation in all the silica samples. The TGA experiments were carried out by loading *ca*. 20 mg sample into the TA Instruments Hi Res TGA 2950 equipped with an EGA furnace and heating to 1000 °C at a rate of 10 °C/min in a Pt pan under an air flowrate of 120 mL/min. The third method for determining the extent of functionalization is total sulfur analysis, which also operates by heating the sample. Instead of measuring the mass loss as in TGA, a small sample was heated in an Eltra Total Sulfur Analyzer which determines the mass percent of sulfur based on infrared analysis of the combustion products (sulfur oxides).

3.1.4 Characterization of Functionalized Particles

Nitrogen sorption isotherms were collected at 77 K for all functionalized and unfunctionalized samples using a Micromeritics Tristar 3000, and pore volume distributions were calculated by Tristar 3000 V 4.02 software using the BJH method.

Differential scanning calorimetry (DSC) analyses were conducted on MPTMS- and S4-functionalized Silica A particles to demonstrate that there is a cross-linked network on the S4-functionalized particles, but not on the MPTMS-functionalized particles. Approximately 5-10 mg of particles were heated to 130 °C then cooled to 30 °C in order to remove excess moisture. The same samples were re-heated to 300 °C at a rate of 5 °C/min in a Pt-Rh alloy pan under an N_2 atmosphere, and the heat flow was measured. The baseline DSC plot for an empty pan was subtracted.

3.1.5 Determination of Mercury Capture Efficiency

Mercury capture efficacy was determined using a packed bed experiment, which has been described in detail elsewhere.[32] A Vici-metrics mercury emitter cell (1454 ng Hg/min at 100 °C) was used as a mercury source, and it was diluted into a stream of nitrogen flowing 60 mL/min. The dilute mercury gas flowed through the packed bed which was held at 140 °C by immersion in a silicone oil bath. The outlet concentration of mercury was determined using a Model 400 Cold Vapor Mercury Analyzer from Buck Scientific. To confirm the results of the online-mercury analyzer, the packed bed was digested in 25 mL of a 4:1 mixture of 16 M nitric acid and 8 M hydrochloric acid. After overnight digestion, the mixture was diluted with deionized ultrafiltered (DIUF) water. The remaining solid particles were removed by syringe filtering through a 0.45 μm PVDF membrane. The concentration of mercury in the supernatant was determined by preparing standard solutions and analyzing using a Varian Vista Pro ICP-OES. The lowest detectable concentration for Hg^{2+} ion for this method is 0.5 ppm.

3.2 Aqueous Mercury Sorption

3.2.1 Sorbent Characterization

The thiol-modified sorbent is a proprietary composite particle from NEI Corporation. The composite has a carbon core with a thin heterogeneous shell of silica, functionalized through silane chemistry with 3-mercaptopropyltrimethoxy silane (MPTMS). Unless noted specifically (as in the case of the regenerable sorbents), the functionalization of these sorbents was done by the manufacturer. The sulfur content (as reported by NEI) is given in Table 2.2 for the various sorbents designated SCC-0, SCC-2, and SCC-3. The SCC-3 particles were also provided in three agglomerate sizes (designated aggregated, non-aggregated, and milled) with size ranges shown in Figure 5.1. These size ranges were determined by sieving the particles (with shaking) and measuring the mass fractions that pass through each sieve. All three agglomerate sizes are made up of the same base particles, as determined by dynamic light scattering (DLS) after sonication in ethanol. Thermogravimetric (TGA) data, as well as differential scanning calorimetry data collected simultaneously with the TGA data, were acquired. A few mg (10-20) of sorbents were loaded into a Pt-Rh pan, and the temperature was increased at 20 ºC/min to 1000 ºC (under air flow of 60 mL/min) as the relative sample mass was determined. Nitrogen sorption isotherms were acquired at 77 K after degassing under nitrogen at 120 °C for at least 8 h, and pore size distributions were also calculated. TEM images were obtained on a Jeol 2010F TEM with an accelerating voltage of 200kV.

The hydrolytic stability of the thiol moiety was determined by leaching tests and sulfur analysis using ICP. Specifically, 150 mg of sorbent was placed in a 40 mL EPA-certified sample vial, and DIUF water was added, and the pH was adjusted with 1% nitric

acid to pH of 5.5 – 6. Samples were shaken for 8 h, and then filtered through a 0.45 μm PVDF syringe filter. The concentration of the filtrate was determined using ICP (λ = 182 nm for S). Standard solutions up to 200 mg/L were prepared and for all calibrations, $R^2 \geq 0.99$. Duplicate runs of the same sample leachate were precise within 4%. Duplicate trials of each material were also done to confirm results.

3.2.2 Mercury Sorption using Thiol-functionalized material

The total capacity (Q) of these sorbents were determined by a material balance from the initial Hg concentration ($C_{Hg,0}$) and the supernatant concentration (C_{Hg}). The initial Hg solution was freshly prepared by dissolving solid $Hg(NO_3)_2$ in a few drops of concentrated nitric acid, diluting to the desired volume, and adjusting the pH using sodium hydroxide. The concentration of the final solution was determined using inductively coupled plasma (ICP). Sorbent particles were removed prior to ICP using Whatman polypropylene syringeless filter devices with PVDF membrane (450 nm pores). Duplicate and spiked ICP samples were used to insure quality control.

The number of accessible surface thiol sites was quanitified using Ag(I) sorption, as it is found in the +1 oxidation state and interacts with the thiol in a 1:1 ratio. Silver nitrate solution was prepared by dissolving $AgNO_3$ in a few drops of concentrated nitric acid, and diluting with DIUF water. Afterwards, samples were removed and filtered using a 0.45 μm PVDF filter. The concentration of the supernatant was analyzed using ICP (λ=328 nm), and the silver sorption capacity was calculated by a material balance ($C_{Ag,0} - C_{Ag}$).

Kinetics of sorption was also determined. In these experiments, a single batch of Hg solution was prepared (300-600 mL) and sorbent was added. Samples (less than 5

mL) were removed periodically and concentration was determined by ICP. The total sample volume removed was always <10% of the total volume to minimize error.

Real water testing of these sorbents was conducted using mercury-contaminated water from Oak Ridge National Laboratory (Sump I in basement of Building 4501). Both SCC-3 aggregated and SCC-3 non-aggregated columns were tested, with experimental parameters given in Table 3.1. Effluent mercury concentration was tested thrice weekly. Samples (10 mL effluent and 0.1 mL influent samples) were preserved by addition of nitric acid, prepared by addition of stannous chloride to reduce the Hg(II) to Hg(0), and analyzed by RA-915A Mercury Analyzer (Ohio Lumex, Inc., Twinsburg, OH). The instrument was calibrated up to 100 ng Hg with a detection limit of 0.1 ng (or 10 ng/L for the effluent sample). An air purge was used to transport the reduced mercury vapor into the measurement cell and analysis was conducted at λ=245 nm.

3.2.3 Regeneration of Sorbent Materials

Regenerable sorbent materials were prepared in our lab by functionalizing the proprietary core-shell particle with both sulfonate and thiol moieties. The goal was to achieve approximately equimolar thiol and sulfonate groups. Five grams of unfunctionalized sorbent was dispersed into 25 mL methanol with stirring, and 125 µL 3-mercaptopropyl-trimethoxy silane (MPTMS; from Gelest) was injected. This is sufficient to react with 25% of the available silanol groups, assuming that the surface area is ~100 m^2/g and ~3 silanol/nm^2. while the mixture was heated to 80 ºC over an oil bath. When the methanol had evaporated leaving a slurry, the particles were cured at 110 ºC for 8 h. They were washed in methanol to remove unreacted silane, centrifuged, and dried at ambient temperature under vacuum. A portion of these particles were retained

Table 3.1 Experimental parameters for real water sorbent tests.
*BV = bed volumes

	SCC-3 aggregated	SCC-3 non-aggregated
Dry weight sorbent (g)	7.9	10.2
Flow rate (mL/min)	1.82	2.16
Flow rate (BV*/min)	0.078	0.079
Total volume treated (L)	302	362
Total volume treated (BV*)	12,950	13,210
Inlet Hg concentration (µg/L)	6.34	6.34
Inlet Na concentration (mg/L)	9.11	9.11
Inlet Ca concentration (mg/L)	41.2	41.2
Inlet Mg concentration (mg/L)	12.1	12.1

for sorption experiments. The remainder of dried particles were then mixed with 40 mL of 8 vol% aqueous solution of 3-trihydroxysilyl-propane sulfonic acid (THSPS; received as 30-35% wt% in water; from Gelest), which was adjusted to pH=4.9 with NaOH. The same process was repeated: evaporation of water to leave particle slurry, curing, washing, centrifugation, and drying under vacuum. The molar ratio of sulfonate:thiol added was 10:1, but this does not mean all reacted.

The extent of available thiol and sulfonate was determined by sorption with Ag^{+} and Ca^{2+} for particles with only thiol and with both thiol and sulfonate. A silver solution was prepared: 88 mg/L (0.81 mmol/L) and initial pH of 6.1. Calcium solution was also prepared: 22 mg/L (0.54 mmol/L) and initial pH of 5.8. Two 50-mg sorbent samples were used with each solution in 40 mL volume for 90 h. Also, to determine if the material is useful for Hg sorption, a 140 mg/L solution (0.70 mmol/L) was prepared and 50-mg sorbent samples were shaken in 40 mL solution for 90 h. Concentrations of all solutions were analyzed with ICP.

Once the lab-synthesized material was shown to have high capacities, the regeneration ability was tested. A 150 mg/L Hg solution was prepared and pH adjusted to 6.4. Part of this solution was also mixed with $Ca(NO_3)_2$ in order to test the sorption in the presence of competing ions. The first sorption experiment was conducted as previously described and the capacity determined by ICP. The supernatant was removed and the particles were then immersed in dilute HCl (at pH = 4) and shaken overnight. The concentration of Hg removed from the particles into the regenerating solution was again determined by ICP, and the % regeneration calculated. Characterization (nitrogen

sorption, TGA, DSC, TEM) of the lab-synthesized material was carried out as previously described.

3.3 Mixed Matrix Membranes (MMM) Applications

MMM was synthesized from polysulfone and sorbent using the well-known phase inversion technique. To synthesize the MMM with high sorbent loading, 3 g polysulfone (PSf; from Aldrich; M_w = 16,000) was dissolved in 15 g anhydrous dimethylformamide (DMF), and SCC-3 particles were added to this solution to achieve desired sorbent wt% (on solvent-free basis). After stirring for 24 h to disperse the particles, the membrane was cast under ambient conditions into DIUF water. The evaporation time was less than 10 s. Final membrane thickness and mass was determined after drying.

MMM were used for Hg sorption in convective flow mode under nitrogen (< 6 bar). The water flux (J_W) was determined by measuring amount of water passed per unit time at different pressures. The Hg sorption capacity with kinetics was determined by passing a feed solution of mercury at known concentration ($C_{Hg,\ feed}$) and determining the permeate Hg concentration, also using ICP.

3.4 Elemental Mercury Vapor Sorption

Silica samples were provided by the J. M. Huber Corporation. For most materials, mesoporous silica gel particles were doped with copper (as copper sulfate, $CuSO_4$) and silanized with bis-(triethoxy silyl propyl)-tetra sulfide (S4) using dry silanization techniques. Si-1 material listed in Table 2.1 gives information on the typically used sorbent materials; other compositions were also briefly tested as described in Chapter 7. The materials were conditioned prior to Hg exposure using ultra-high

purity nitrogen at 140^{o}C for 30-60 min. A variety of silica-based samples were provided to examine the impact of composition on Hg capture.

3.4.1 Surface Area Measurements by N_2 Sorption

A 100-mg sample was prepared by degassing for 6 h at 140 ^{o}C under N_2 refluxing. The N_2 adsorption isotherm at 77 K was then measured using a Micromeritics Tristar 3000 pore volume analyzer. The total surface area was then calculated using the BET method.

3.4.2 SEM with Energy Dispersive X-Ray (EDS) Analysis

Scanning electron microscope images of select sample were acquired on a Hitachi Model S-3200-N scope using a working distance of 15 mm and source voltage of 20 kV. A sample of Si-1 after mercury saturation was pressed onto carbon tape affixed to an Al stage (15 mm diameter). Elemental probing was performed using EDS.

3.4.3 Fixed-Bed Mercury Vapor Adsorption

The total adsorption capacity of all functionalized silicas was determined using a fixed-bed system reported previously by our group.[16] The experimental set-up is shown in Figure 3.1. The packed-bed consisted of a 500-mg sorbent bed suspended in one arm of a 0.9 cm I.D. glass U-tube using approximately 0.15 g of glass wool to prevent particle loss under gas flow. The U-tube was maintained at 140 °C using a silicon oil bath and temperature controller. Mercury vapor was generated using a mercury permeation tube (VICI Metronics) that is capable of producing 1596 ng/min of Hg^0 at 100 °C. The permeation tube was supported on glass beads packed in a glass U-tube and maintained at 100 °C using a silicon oil bath. Ultra-high purity nitrogen, N_2 (99.999%, Scott Gross), was used as the carrier gas and was fed into the system at 60 mL/min using a Brooks

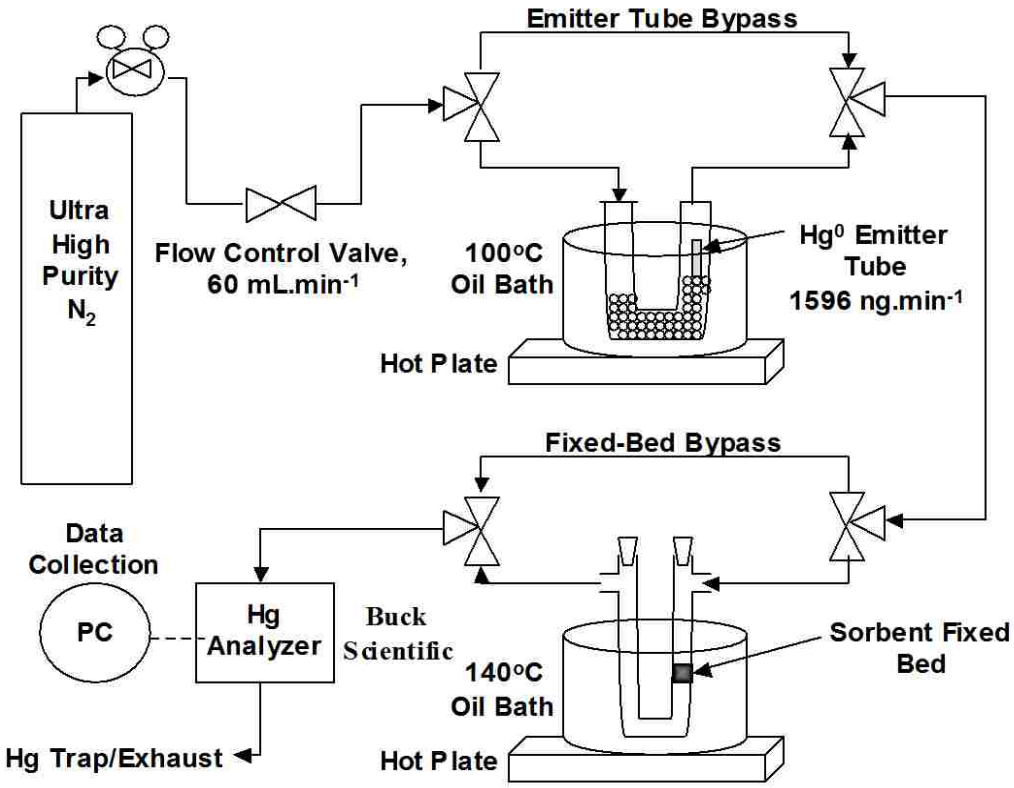

Figure 3.1 Experimental apparatus for fixed-bed mercury sorption.

Model 5850E mass flow control valve and Model 0152 controller. At these conditions, the concentration of Hg^0 in the inlet to the packed bed should be 2.97 ppm. The empty-bed residence time based on a bed height of approximately 1 cm was 0.65 s. The concentration of Hg used was three orders of magnitude larger than the concentration of Hg in most flue gases (2 ppb).

The system was equipped with four 3-way valves that allow for bypass of the Hg source, the packed bed, or both. Online monitoring of Hg was achieved using a Buck Scientific Cold Vapor Mercury Analyzer 400. The detector supplied an output signal in terms of the mV response to the change in % transmittance at a 253.6-nm wavelength to a coupled computer with a sampling interval of 0.5 s. Typical tests began by first bypassing the Hg source and feeding nitrogen through the packed bed to establish a zero baseline for the detector. The nitrogen flow was then routed to the Hg permeation tube and fed to the packed bed until a minimum of 90% exhaustion was achieved. A 20-mg sample of the contents of the bed was digested overnight using 40 mL of an aqua regia medium (4 M HCl and 1 M HNO_3). The amount of total Hg was then quantified using inductively-coupled plasma (ICP) elemental analysis.

3.4.4 Mercury Analysis Using Inductively-Coupled Plasma (ICP) Analysis

Digested samples were analyzed for Hg using a Varian Vista-Pro CCD Simultaneous ICP-OES (optical emission spectrometer). Analysis of Hg was performed at wavelengths of 194.1 and 253.7 nm. These wavelengths were selected because of their lack of susceptibility to Cu interference. The instrument was programmed to obtain readings in triplicate for each sample. An acidic rinse cycle was used between samples to avoid carry-over. The detector was calibrated to a lower limit of 0.5 ppm Hg, with a

linear trend existing over the entire calibration range. The lower detectable limit was 0.2 ppm Hg. The upper calibration limit was selected based on the anticipated amount of Hg captured for a given sorbent and ranged from 6-10 ppm Hg. Standards were prepared by digesting fresh sorbent (no Hg exposure) in the same aqua regia medium and spiking with appropriate quantities of a known Hg standard (Fisher) to produce the desired concentrations. Prior to analysis of digested samples, known samples were first prepared and analyzed to verify the accuracy of the machine. Both a 1.5-ppm and 0.5-ppm known sample routinely gave errors of less than 1%. Digested samples of exhausted beds were split in half, with a 0.5 ppm Hg spike added to one sample to verify the analysis by method of additions. This method was checked using a 0.5-ppm known sample, which yielded a recovery error of 9%.

3.4.5 Leaching Studies

The loss of Cu and Hg from a selected sorbent was examined both before and after impregnation in Concrete. Concrete samples were prepared using a Quikrete Fast-Setting cement mix that had been degraveled. A typical concrete blend consisted of 65-wt% cement, 34.5-wt% fly ash obtained from a Reliant Energy coal-fired power plant, and 0.5-wt% of Hg-saturated sorbent. This composition was based on typical standards for fly ash in concrete.[22] The dry materials were thoroughly mixed and then prepared for casting through the addition of de-ionized, ultra-filtered water to obtain a suitable working viscosity. The composition is shown schematically in Figure 3.2. After pouring, the concrete slug was allowed to dry and set overnight.

Leaching of sorbents after Hg exposure were performed by placing 50 mg of sorbent in 20 mL of deionized ultrafiltered water with an adjusted pH of 4.0 through the

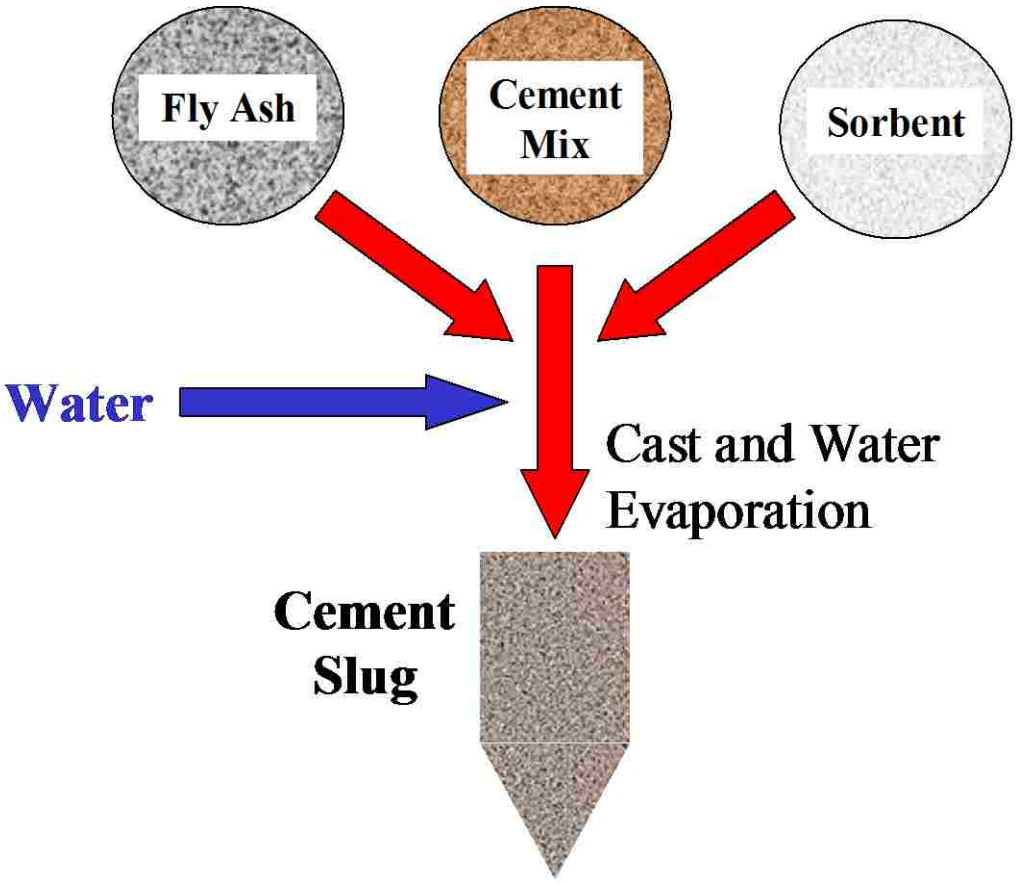

Figure 3.2 Cement slug composition for metal leaching experiments. Exact experimental compositions are given in Chapter 7.

addition of nitric acid. The leaching was carried out under mixing for 12 h. Concrete leaching studies were conducted using EPA Method 1312 Synthetic Precipitation Leaching Procedure.[23] Concrete slugs were placed in deionized ultrafiltered water with an adjusted pH of 4.2 through the addition of a solution of sulfuric and nitric acid (60 vol. % sulfuric and 40 vol % nitric). The liquid-to-solid ratio was 20:1. Leaching was allowed to occur under mixing for 24 h. In both cases, samples were prepared for Hg and Cu analysis by ICP. The analysis of Cu by ICP followed the same procedures used for Hg analysis given above with the exception of the selected wavelength for analysis (213.6, 219.2, and 224.7 nm for Cu analysis).

3.4.6 Moving-Bed (Injected) Vapor-Phase Hg Capture in Simulated Flue-Gas

In-flight mercury capture experiments were conducted in the U.S. EPA's Entrained Flow Reactor (EFR, Research Triangle Park, NC). A detailed description of the EFR set-up has been provided previously.[16] A schematic of the basic system is shown in Figure 3.3. Briefly, the system consisted of a 332 cm by 4 cm ID Pyrex contactor that was heated by three electric tube furnaces (Lindberg, USA) to maintain a constant controlled temperature. A water-cooled methane gas burner provided combustion flue gases (CO, CO_2, H_2O, and O_2) while other flue gas components (N_2, SO_2, NO, HCl) were introduced into the reactor at constant concentrations using compressed gases and mass flow controllers. Elemental mercury vapor (Hg^0) was generated using a permeation device (Dynacalibrator, VICI Metronics) with a N_2 carrier and subsequently mixed with the simulated flue gas before entering the EFR. The sorbent was entrained into the reactor using a nitrogen purge stream. The sorbent feeding assembly consisted of a gas supply manifold, a feed tube, and a syringe pump mounted to a vibrating plate. For all

Figure 3.3 Experimental apparatus for injected vapor-phase mercury sorption.

tests, the sorbent was diluted with an inert material (diatomaceous earth (DE) flour) at varying mixtures depending upon the desired sorbent injection rate. This dilution allowed the syringe pump to perform in the middle of its operating range and helped to maintain a steady sorbent addition rate. Although the EFR is capable of simulating a variety of conditions, the gases were mixed to simulate the flue gas that would be expected from the combustion of a low-sulfur Western sub-bituminous coal (e.g., such as that from Wyoming's Powder River Basin). The experimental conditions are given in Table 3.2.

Experiments were initiated by heating the reactor to the desired temperature and performing the necessary calibration checks for continuous emissions monitoring. An advanced Hg Continuous Emission Monitor (CEM) Nippon DM-6B (NIC, Japan) provided the concentration and speciation (elemental vs. oxidized) of Hg in the simulated coal combustion flue gas using a 10 s sampling interval. Baseline measurements were collected before beginning injection of the sorbent. The sorbent-DE mixture was added continuously for at least 20 minutes before stopping the injection and diverting the gas stream to bypass the on-line Hg analysis. The system was cooled and the reactor walls and tubing were thoroughly cleaned between experiments to prevent "memory effects" due to any accumulated sorbent on the reactor or tubing walls.

3.4.7 Fixed-bed Hg Adsorption Experiments at various Temperatures

Packed bed Hg capture experiments using this sorbent were conducted at 140 °C, 100 °C, 70 °C, again at 140 °C; all for 24 h. The second run at 140 °C was performed to ensure that results were not biased as the Hg source was depleted. The experimental apparatus has been described in detail elsewhere. Briefly, a packed bed was formed from

Table 3.2 Experimental parameters for injected vapor-phase mercury sorption.

Target	Unit	Wet basis	Dry basis	Remarks
HCl	ppm	10	10.8	from gas cylinders
SO_2	ppm	500	538	from gas cylinders
NO	ppm	200	215	from gas cylinders
CO_2	vol%	3.5	3.8	from methane burner
CO	ppm	~5	~5	from methane burner
O_2	vol%	6.8	7.3	from methane burner
H_2O	vol%	6.8	0	from methane burner
N_2	vol%	balance	balance	from cylinders &burner
$Hg^0(g)$	$\mu g/nm^3$	~21.5	~20	Hg^0permeation tube
Total flow	L/min	14	13	std cond, 1 atm, 20 °C
Temperature	°C	140	140	139-144 °C

sorbent which had previously been heated at 140 °C under flowing N_2 (60 mL/min). Mercury was released from Hg emitter tube at 1447 ng min^{-1} Hg vapor. During the 24-hour run, the total amount of Hg that passed into the bed was 2.08 mg Hg. The entire sorbent bed and glass wool of each trial was digested in a mixture of 20 mL conc. nitric acid and 5 mL conc. hydrochloric acid. After overnight digestion, this mixture was diluted with deionized ultrafiltered (DIUF) water to a total volume of 40 mL. A 100-mg sorbent not exposed to Hg was heated for 1 h at 140 °C under 60 mL min^{-1} of flowing N_2, and it was digested according to the same procedure.

Standard Hg solutions were made: 1 ppm, 2 ppm, 4 ppm, 10 ppm; these were made by mixing 2.5 mL of the digest water, an appropriate amount of 100 ppm $HgNO_3$ (diluted stock solution from Fisher); and enough water to dilute to 10 mL. The digested solutions were filtered with 0.45 μm PVDF membrane filter syringe, and the 2.5 mL of the supernatant solution was diluted to 10 mL with water. The concentration of Hg in the samples was determined using inductively coupled plasma instrument, based on the intensity of the samples at $\lambda = 253$ nm. All measurements had a relative standard deviation of less than 4 %.

3.4.8 XRD of Sorbents and Product

X-ray diffraction patterns were obtained at room temperature with 2-theta from 10° to 60° and a step size of 0.2° at a rate of 1^0/min for the following samples: anhydrous copper sulfate, S4 functionalized copper sulfate doped silica gel (both heated and unheated), S4 functionalized silica gel, mercury sulfide, and S4 functionalized copper sulfate doped silica gel after being exhausted with mercury capture.

3.5 Reactive and Catalytic Nanoparticle Synthesis

Colloidal silica Ludox TM-50 was obtained from Grace Davison (Columbia, MD) & silica gel from Huber Corp (Havre de Grace, MD). Sulfonated silane reagent, 3-(trihydroxysilyl)-1-propane sulfonic acid (30-35 % in water) (THSPS), was obtained from Gelest Inc. (Morrisville, PA). Potassium tetrachloropalladate was obtained from Sigma-Aldrich. Deionized ultrafiltered (DIUF) water & ethanol were obtained from Fischer Scientific.

3.5.1 Functionalized Silica Synthesis

Silica D (silica gel) and Ludox were functionalized with 3-trihydroxylsilyl-1-propane sulfonic acid (THSPS) using previously reported[81] methods without the use of organic solvents. Briefly, a 3 wt% aqueous solution of THSPS was adjusted to pH = 4.9. Silica particles (10 g in each batch) were dispersed into 50 mL DIUF water and the silane solution (about 75 mL) was injected with vigorous stirring. The mixture was stirred for 15 min to disperse the silane, followed by heating (with stirring) to 100 °C until all water was evaporated. The functionalized particles were cured for 4 h at 100 °C to complete the silylation. They were washed with water to removed excess silane, centrifuged, and dried.

3.5.2 Extent of functionalization

The extent of functionalization was determined by infrared spectroscopy and thermogravimetric analysis methods given in detail elsewhere.[81] Briefly, a small amount of functionalized particles were finely ground with potassium bromide and pressed into a die. The Fourier transform infrared spectrum was recorded based on 128 scans from 4000 to 400 cm^{-1}. The same procedure was carried out for unfunctionalized particles, and

the heights of the Si-O-H peaks at about 980 cm^{-1} were compared; assuming that the loss of silanol groups due to functionalization is proportional to the decrease in Si-O-H peak height. Determining extent of functionalization by thermogravimetric analysis was done by recording the mass loss of a sample as temperature is increased from room temperature to 1000 °C (at a rate of 10 °C/min). The total mass losses of a functionalized and unfunctionalized sample were compared.

3.5.3 Silica-Based Fe Particle Synthesis

The first step to forming Fe/Pd particles is to immobilize the ferric ions. The sulfonate-functionalized silica particles were shaken in a 0.017 *M* ferric chloride ($FeCl_3 \cdot 6H_2O$; 951 mg Fe/L) solution for 12 h. The pH of ferric solution was 2.5 and was unchanged after shaking with the particles, since they were in the Na^+ form (by previously adjusting silane solution pH using NaOH). After centrifugation to remove the particles, the amount of sorbed Fe was determined by measuring the Fe concentration in the supernatant with inductively coupled plasma (ICP) at multiple wavelengths. Next, the immobilized ferric ion was reduced to zero-valent iron (ZVI) by borohydride. A freshly prepared 0.17 *M* solution (50 mL) $NaBH_4$ was added dropwise to a beaker containing about 20 mg of Fe immobilized on ~3 g silica dispersed in 100 mL deoxygenated water. The particles turned gray due to the formation of black iron particles on the white silica surface. The reduction was allowed to continue for 1 h, and the silica/Fe particles were centrifuged, washed with ethanol, and dried. In the case of particles silica-based particles used for oxidative dechlorination reactions, the Fe NP were oxidized using air bubbled through a dispersion of these particles in water for up to 24 h. The iron oxide/iron particles on silica were then centrifuged and dried.

3.5.4 Ascorbic acid as a reducing agent

Besides immobilization or the use of polyligands, another method to synthesize particles while inhibiting oxidation and aggregation is to use natural weak reducing agents, such as ascorbic acid. Excess reducing agent adsorbs to the particle surface to prevent oxidation of the particle, and various surface adsorbed species can also inhibit aggregation. Ascorbic acid is a weak reducing agent, and therefore will not sufficiently reduce iron without the presence of another reduction reaction. Therefore, bimetallic Fe/Pd particles were prepared by the co-reduction of $FeCl_3 \cdot 6H_2O$ and K_2PdCl_4 with ascorbic acid, which is a modification of a recent procedure.[53] Briefly, for each batch prepared, 10 mL of a 0.1 M ascorbic acid solution was mixed with 20 mL of 0.01 M ferric solution ($FeCl_3 \cdot 6H_2O$). Particles were formed upon the addition of $PdCl_4^{2-}$ solution (10:1 Fe:Pd ratio). Alternatively, Pd can be prepared alone by reduction with ascorbic acid: particles were first prepared by reducing $PdCl_4^{2-}$ to Pd^0 using ascorbic acid in ten times the stoichiometric amount, 23.1 mM ascorbic acid solution was used with four times the volume of Pd(II) solution. Upon reaction, the solution turned immediately gray. Then, Pd particles were prepared in various ascorbic:Pd molar ratios for analysis.

3.5.5 Metal particle characterization

Metal or bimetallic particles were characterized using several methods. Nitrogen sorption data at 77K was obtained using a Micromeritics Tristar 3000 instrument. Surface adsorbed species were detected by Nicolet Nexus 470 infrared spectrometer running Omnic software. Particle morphology was determined in Jeol 2100 TEM at 200kV accelerating potential and dynamic light scattering was used to determine hydrodynamic radius.

3.5.6 TCE degradation experiments

TCE degradation experiments were carried out in 20 mL EPA glass vials with a gas-tight PTFE-coated PDMS septum. Samples were initially loaded with particles and TCE solution (20-30 mg/L). A control vial was prepared without particles to ensure that no TCE was volatilized. The concentration of TCE in a sample was determined after a certain time interval by extraction of the sample with pentane (5 µL ethylene dibromide (EDB) as an internal standard, per 100 mL pentane) and analysis using gas chromatography (HP Series II model 5890) with a mass spectrometer (HP 5971A) detection system (GC-MS). Each sample was used for only a single data point. Standard solutions (1 to 30 mg/L) of TCE in pentane were prepared, also using EDB as an internal standard. The lowest detection limit was 1 mg/L TCE in pentane.

For oxidative dechlorination experiments (using oxidized particles), each sample vial was loaded with reactive particles (average loading = 0.16 g/L Fe; detected by acid digestion followed by atomic absorption), hydrogen peroxide ($C_{initial}$ = 1409 mg/L), and TCE ($C_{initial}$ = 22 mg/L) in deoxygenated water. Each vial (20 mL clear EPA vial with Teflon-coated septum) was shaken for a time and opened only once, where 4 mL of the solution was removed. This solution was extracted by shaking with the EDB-containing pentane. After 2 h extraction, the concentration of TCE in the pentane was determined by GC-MS. For reductive dechlorination experiments, the same sampling and analysis procedure was used. The initial concentrations were 1 g/L Fe loading, 30 mg/L TCE, and no hydrogen peroxide.

4. Chapter Four: Functionalization Fundamentals

The first objective of this study is to determine the effect that silica particle structure and silane structure have with regard to the maximum extent of silica particle functionalization, using IR, Ag^+ sorption, TGA, and TSA. The second objective is the characterization of the functionalized silica particles. The third objective is to demonstrate how pore structures influence breakthrough capacity of these sulfur-functionalized particles.

4.1 Effect of silica particle structure on extent of functionalization

The three types of silica particles used in this study (Table 4.1) were chosen because of their different structural characteristics. The surface areas and average pore diameters of the S4 functionalized silicas are also given. Silica A and silica B are both porous silica gels with similar particle diameters; Ludox (TM-50) is colloidal silica with monodisperse primary particles 22 nm in diameter (provided by manufacturer but confirmed by our lab using dynamic light scattering and SEM). Nitrogen sorption isotherms (Figure 4.1a,c) for these samples are IUPAC Type IV confirming the porous nature of the sample.[82] Silica A has a much larger hysteresis than Silica B due to the larger mesopores. Although the Ludox base particles (22 nm) are non-porous, the small diameter allows for close packed aggregates of particles, which leads to a small "pores" between particles. The nitrogen sorption isotherms and pore distributions for the functionalized particles (Figure 4.1b,d) are described below. The extent of S4

Table 4.1 Silica morphology before and after tetrasulfide functionalization.
Silicas A and B are amorphous silica gel particles and Ludox is a colloidal silica particle which has a non-porous base particle ("pores" arise through interparticle spacing in dried agglomerates of colloidal particles).

		Unfunctionalized Silica		S4-Functionalized Silica	
Silica Sample	Particle Size (μm)	Average Pore Diameter (nm)	Surface Area (m^2/g)	Average Pore Diameter (nm)	Surface Area (m^2/g)
Silica A	3.7	9.6	206	3.3	264
Silica B	3.3	2.9	484	4.7	61
Ludox	0.022	7.1	76	3.2	243

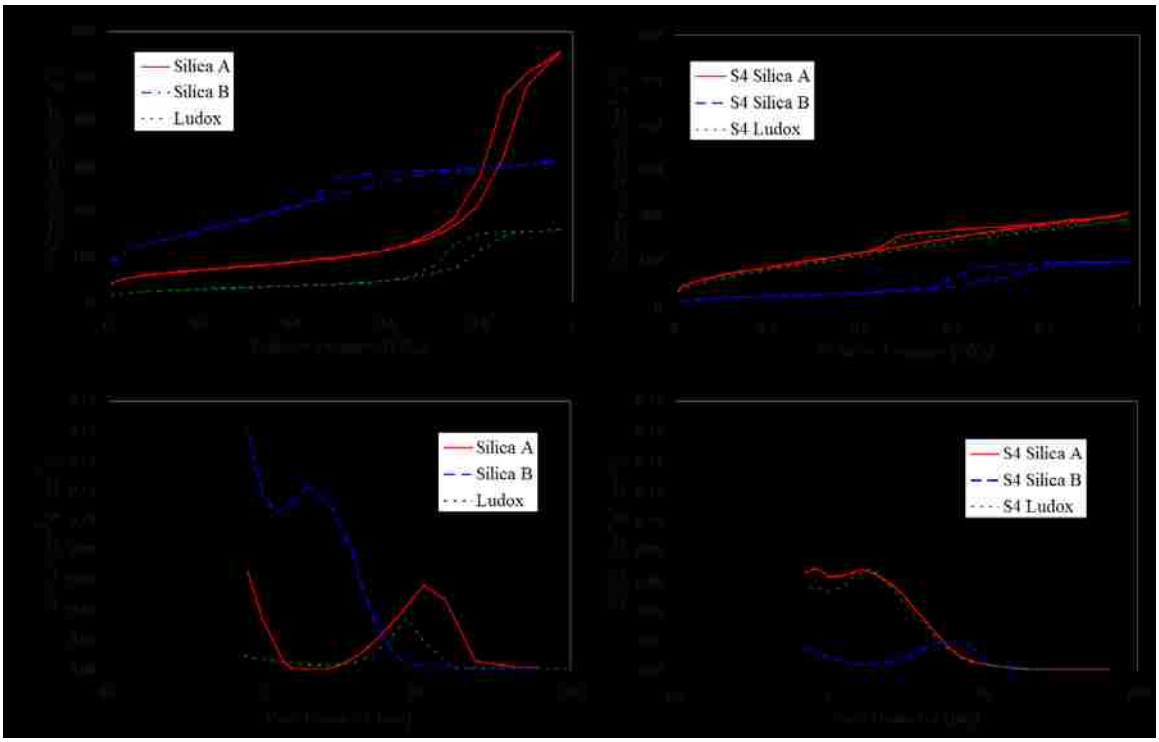

Figure 4.1 Nitrogen sorption for tetrasulfide functionalized silica particles.
(a) nitrogen sorption isotherms at 77 K for unfunctionalized silica
(b) nitrogen sorption isotherms at 77 K for S4-functionalized silica
(c) BJH pore volume distributions for unfunctionalized silica
(d) BJH pore volume distributions for S4-functionalized silica

functionalization on these different particles is determined using infrared spectroscopy and/or thermogravimetric analysis.

Representative FTIR spectra of S4-functionalized silica are show in Figure 4.2. The IR peak at 980 cm^{-1}, which is attributed to the Si-O-H vibration, can be used to determine the extent of functionalization.[9] The FTIR spectra are normalized using the Si-O-Si peak (normalized to the bulk amount of silica), then the difference in peak height between the functionalized and unfunctionalized silica at 980 cm^{-1} is proportional to the extent of functionalization. Since the amount of silica (based upon Si-O-Si peak height) has been normalized for both samples, small differences in the mass of sample used to prepare the pellets can be neglected, and any difference in peak height between the functionalized and unfunctionalized samples is attributed to the disappearance of silanol groups during the silylation reaction.

The extent of functionalization results are summarized in Table 4.2. Silica B has a much larger specific surface area, it may be expected that the larger surface area should allow for a greater extent of silylation. However, Silica A has 54% of its silanols functionalized with S4, with a standard deviation of 8.8% of the silanols functionalized (for 3 different silylation batches). For Silica B, the extent of silylation with S4 is 17% with a standard deviation of 4.2% of the silanols functionalized. These results indicate that the larger pores of Silica A allow for the silane to reach far more of the reactive silanol sites. For the Ludox samples, the IR spectral noise was too great to quantify the extent of silylation, but TGA and total S were used for these materials.

Figure 4.2 FTIR spectra of S4-functionalized silica.
The transmission FTIR peak at 980 cm-1 is attributed to the Si-O-H vibration and its relative height can be used to determine extent of silylation reaction. The decrease in peak height after functionalization is seen here for S4-silica A (54% of silanol groups functionalized).

Table 4.2 Summary of silylation results.

Silica Type	Silane	%Silanol Functionalized (IR)	Mass% Silane (TGA)	Mass % Sulfur (TSA)
Silica B	MPTMS	38	10.6	3.99
Silica A	S4	54	12.0	4.53
Silica B	S4	17	11.0	3.98
Ludox	S4	NA	4.7	1.56

While IR measures extent of functionalization in terms of how many silanol are reacted, TGA (Figure 4.3) measures extent of functionalization in terms of how much silane can be deposited on it (12.0 weight % silane with standard deviation of 1.6 weight %) than Silica B (11.0 weight % silane with std. dev. of 0.4 %). These values are of the same magnitude as previously reported values using the same method.[83] In the small pores of silica B, both ends of S4 silane are more likely to react with the surface, which would lead to a loss of more SiOH per S4 molecule incorporated. However, the silanes block pore openings leading to fewer silanol functionalized, but the silane has multilayer deposition on the particles surface. The S4-functionalized Ludox has average 4.7 weight % silane (standard deviation of 0.2 weight %) because the Ludox surface area (where the silane can attach) is much smaller. Similar to the TGA method, total sulfur analysis gives the extent of functionalization in terms of total sulfur mass whether those sulfur-containing silanes are covalently bound to the surface or deposited into the pores. Silica A has 4.53 mass % sulfur, and silica B has 3.98 mass% sulfur. Consistent with the TGA results, Ludox has 1.56 mass % sulfur.

Further indication that the higher silane weight % on Silica B (than would be expected by the FTIR results) is due to the large pore sizes is given by the pore volume distributions calculated with the BJH method (Figure 4.1b,d). Silylation of Silica B leads to a decrease in mesopores of all sizes, and the large decrease in surface area (484 to 61 $m^2\ g^{-1}$) arises from the complete blocking of the pores by the large S4. The occurrence of pores after S4 functionalization is greatly decreased, although the BJH model gives a

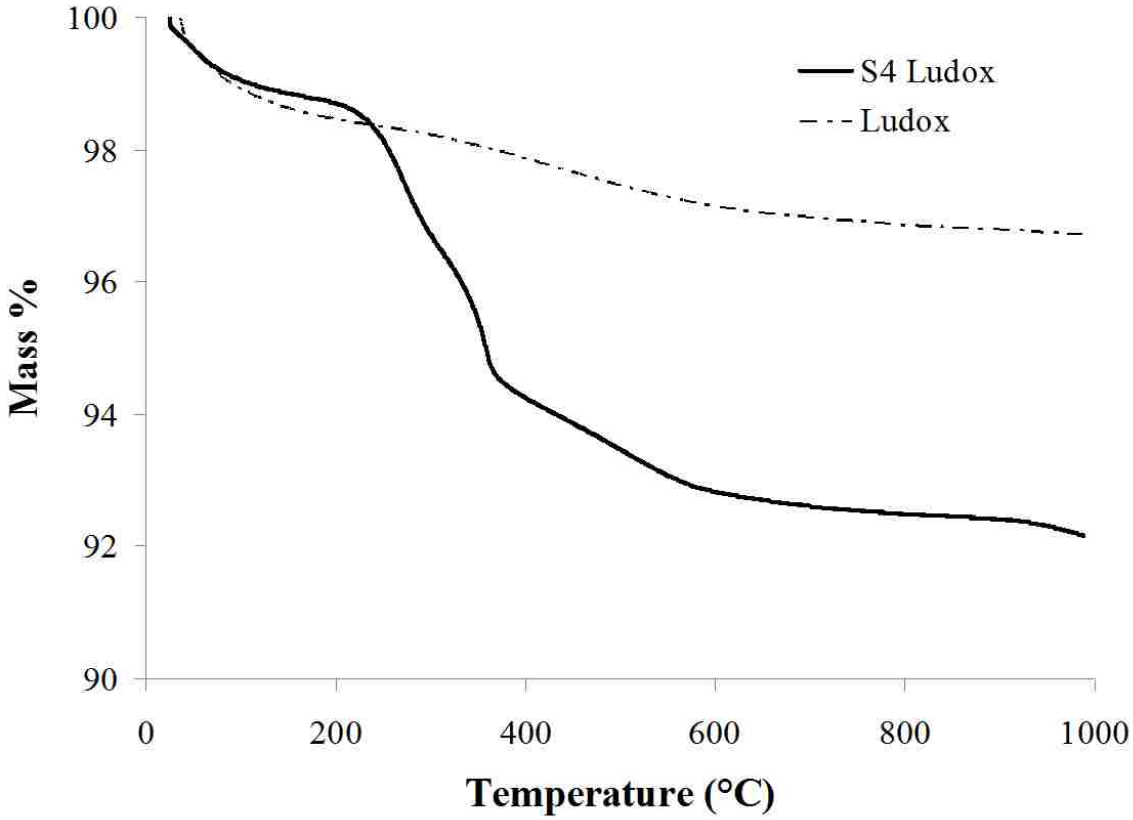

Figure 4.3 TGA plot for S4-functionalized silica

nominal average pore diameter (of the few pores which are remaining) of 4.7. For Silica A, silylation coats the larger mesopores with silane, and the average pore diameter is drastically reduced from 9.6 nm to less than 3.3 nm. However, these narrower pores still have larger surface area, and the addition of S4 actually increases the surface area to 264 m^2/g, suggesting that the S4 is able to form a network on the surface with very small pores. This explanation is also consistent with the order of magnitude decrease in average pore diameter. The silylation of Ludox (4.7 wt% silane) fills in the gaps between particles and results in an agglomeration of particles and the silane network, and the apparent "pore" volume is also reduced for Ludox particles with silylation. However, this agglomeration also produces a porous silane network which contains the particles, as the surface area is increased to 243 m^2/g. The contrast of the IR extent of functionalization results and the TGA extent of functionalization results indicate that TGA can only be used as a reliable metric of extent of silylation if the silane covers the silica as a monolayer or the pores are small enough that multilayer adsorption can be neglected.

4.2 Impact of silane molecule structure on extent of functionalization

A second objective of this study is to determine the difference in extent of silica particle functionalization achieved with different silanes. The two silanes (Table 2.2 & Figure 2.1) which are considered are S4 (with results discussed in the previous section) and MPTMS. These silanes react with the particle surface through a single silicon center ("single-point attachment") in the case of MPTMS, or through one or two silicon centers ("double point attachment") in the case of S4. Silica B is the silica that is functionalized in this comparison. Based on extent of silylation determined using IR spectroscopy,

MPTMS reacted with an average of 38% of silanol groups, with a standard deviation of 8.6 for the 3 different samples which were prepared. However, using the same method, S4 reacted with an average of 17% of silanol groups, with a standard deviation of 4.2, also for 3 different samples. This difference based on the structure of the silanes is expected because the MPTMS functionalizes the silica by one end only. However, the S4 can react with the particle surface at two different locations, and hinders further reaction with other silanol groups and block pore openings.

TGA results indicate that silane reacted with the silica particle surface is approximately the same for both MPTMS (10.6 mass %) and S4 (11.0 mass%) silanes, as the silica particle characteristics are the same in both cases. Total sulfur analysis also confirms this result. The extent of functionalization is not dependent on the structure of the silane molecule for this silica particle with small pores. Based on these results taken together (and converting the mass to moles from the TGA results), it is concluded that not all of the S4 react at both ends. The mole % of S4 on Silica A is 1.7. Considering that for double-point attachment, 2 SiOH are consumed for every S4 added, 3.4 moles SiOH should be reacted in the S4 case. For the MPTMS case, the mole % of MPTMS on Silica A is 4.9 (and also 4.9 moles SiOH consumed). Thus, for MPTMS, 4.9 moles SiOH react, and 3.4 moles of SiOH should react with S4. However, the IR results would indicate that approximately twice as many silanol groups are reacted with MPTMS as with S4, indicating a portion of the S4 does not have double-point attachment.

4.3 DSC Characterization

The functionalized particles were analyzed using differential scanning calorimetry in order to determine if the sulfur-containing silanes exhibited any thermal transitions.

This is of interest because the mercury sorption scheme is proposed to operate at about 140 °C. Although both the heating and cooling scans were obtained for completeness, the cooling scan is more typically used for glass transition identification[84] and is shown in Figure 4.4. For the S4-functionalized silica particles, a slight glass transition is observed at 85 °C. This transition is not observed for the MPTMS-functionalized silica particles. It is proposed that the S4 chains can interact with each other on the surface and act as a polymer network, whereas the reduced thiol groups do not interact on the silica particle surface. Also, it is possible that some of the S4 molecules (with two reactive ends) formed oligomers prior to reaction with the silica particle surface. Further understanding of this network will be important to elucidating the mechanism for mercury capture using these materials.

4.4 Application to Mercury Vapor Sorption

Lab-scale mercury capture experiments were conducted to relate the mercury sorption to the pore structure before and after functionalization. The use of sulfur (in various forms) as a sorbent for mercury is well-known, although the structure of the active site of sorption for this tetrasulfane and mercury is unclear. In this study, the S4-functionalized materials were used for mercury sorption. High capacities have been shown by elsewhere using S4-functionalized silica to which small amounts of copper sulfate have been added (and this is discussed in Chapter 7).[85]

For sorption, the breakthrough curves give information about the accessibility of active sites to the sorbate. Figure 4.5 shows the four breakthrough curves (shown only for $C/C_0 > 0$). The steeper the breakthrough, the more accessible and open structured the

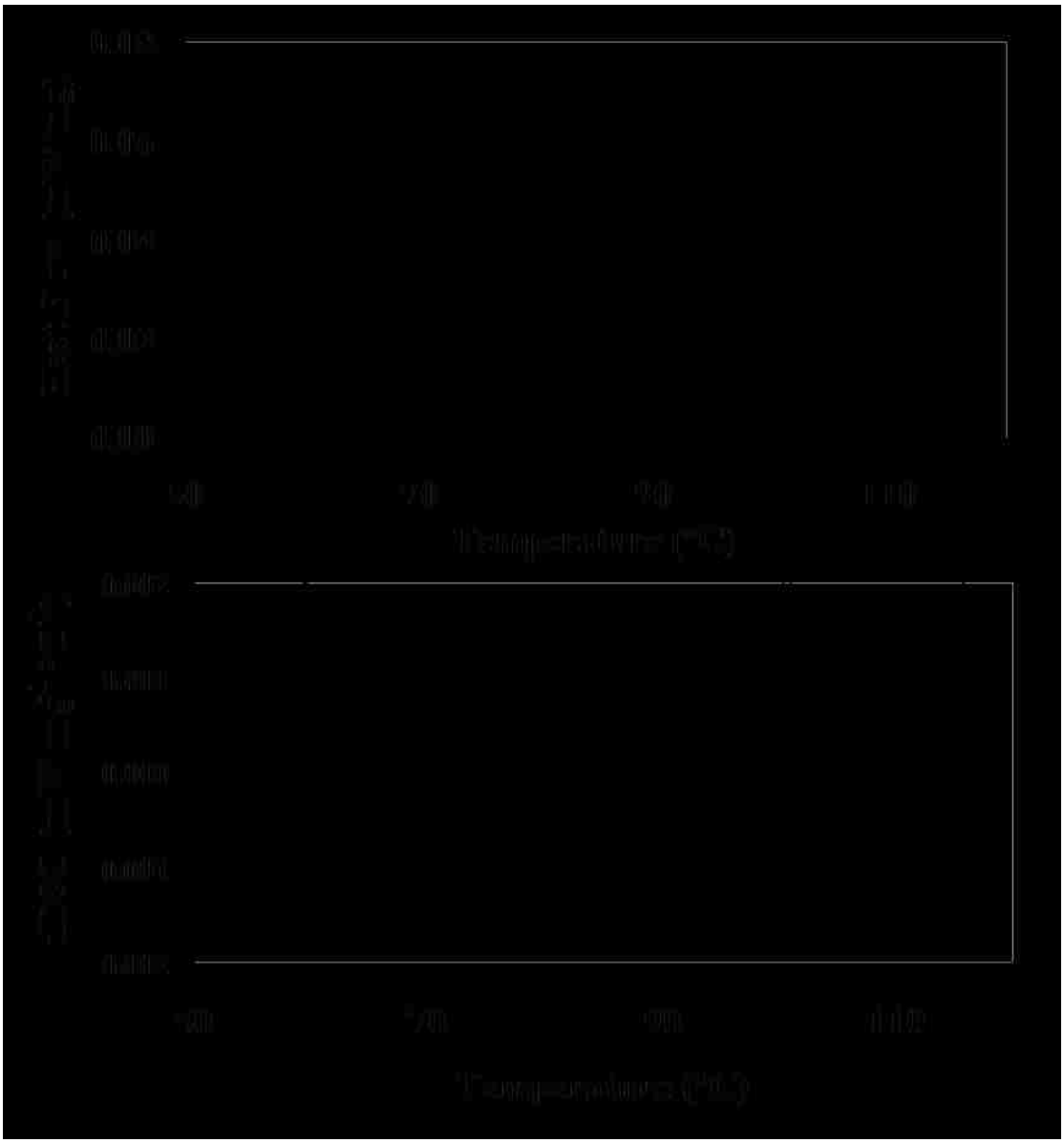

Figure 4.4 Thermal transitions of sulfur-functionalized silica particles.
Differential scanning calorimetry demonstrates thermal transitions of (a) S4-Silica A particles and (b) SH-functionalized particles. These *cooling* scans were obtained by heating to 130 °C in order to remove excess moisture then cooled to 30 °C. Parameters: cooling rate of 5 °C/min; Pt-Rh alloy pan; N2 atmosphere. The baseline DSC plot for an empty pan was subtracted. A slight glass transition (Tg) is observed at about 85 °C for the S4 functionalized, as also confirmed by the DSC derivative plot.

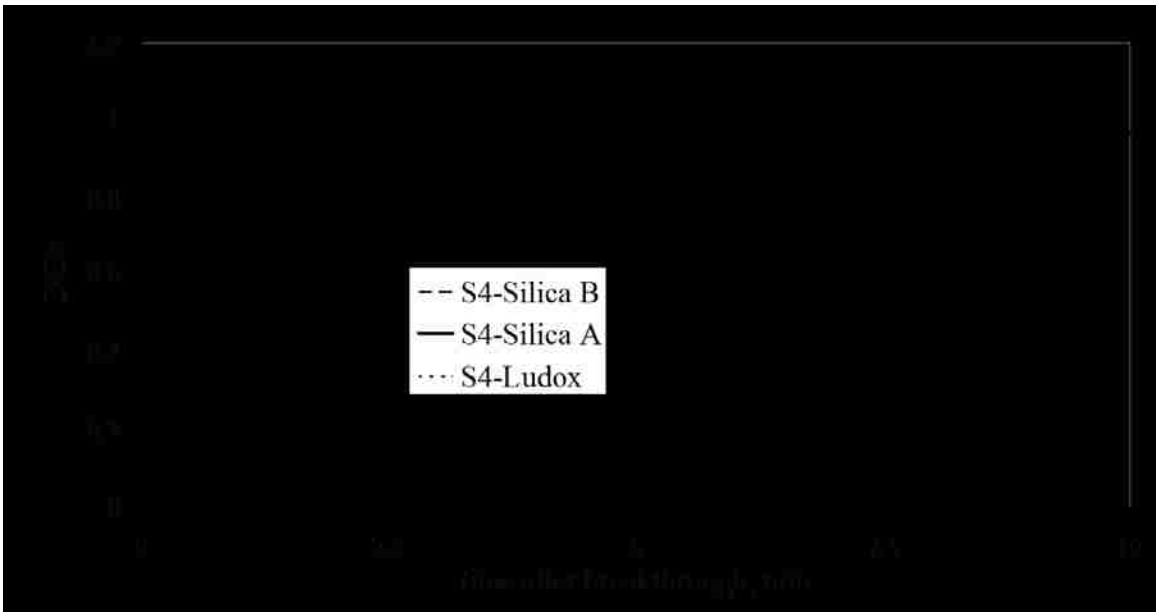

Figure 4.5 Breakthrough curves for fixed bed mercury vapor sorption.
Only shown after breakthrough. Steeper and sharper breakthrough curves indicate the material is more open structured.

sites. The steeper breakthrough curves indicate less mass transfer resistance, which is desirable for applications involving short residence times. S4-Ludox has the steepest breakthrough, but S4-Silica A has the most gradual breakthrough, even though both these materials have almost identical pore distributions and surface areas. However, the difference in these two materials is that much more of the surface area in S4-Ludox arises directly from the S4 network, so the active sites are much more accessible. S4-Silica A also has a very gradual breakthrough at high C/C_0 indicating the high resistance to filling the microporous active sites. Similarly, S4-Silica B has a breakthrough curve which follows closely along the S4-Ludox curve (facile mass transfer due to the S4 covering the pore mouths), but near maximum capacity ($C/C_0 > 0.9$), the curve becomes much more gradual as the few remaining microporous sites slowly become occupied. These curves do not indicate the capacity of the material, only the openness of the functionalized material's pore structure. Most of the capacity is determined by the time before breakthrough.

4.5 Conclusions

Unlike many previous studies which focus on ideal particles, this work has determined extents of reaction for commercially available silica particles which are currently used in various industries, for applications besides mercury sorption. Different methods have been used to determine the extent of functionalization, and it has been shown that up to 50% of the silica surface silanol groups can be functionalized, even with a bridged silane that can attach to the particle surface through two silicon centers. The extent of silylation reaction has been shown to be primarily dependent upon pore distribution, size of the silane, and whether the silane is monofunctional or difunctional. The extent of

functionalization (as deposition) depends on pore morphology and is also not affected by the structure of the silane. These particles have good thermal stability in the temperature range of interest, and the formation of sulfur-containing oligomers on the silica particle surface has been indicated.

5. Chapter Five: Aqueous Mercury Sorption

The objective of this part of the study is to demonstrate thiol-functionalized silica-coated carbon particles for aqueous mercury sorption applications. This involves characterization of the sorbent, determination of equilibrium sorption, demonstration of the role of solution pH and sorbent agglomerate size play in sorption capacity and kinetics, and demonstration of functionalization approaches for regenerable particles, and proposition of future strategies for their optimization.

5.1 Mercury Sorption Using Thiol-modified sorbent

5.1.1 Sorbent Characterization

Sulfur content of the functionalized sorbent is shown in Table 5.1. All samples were functionalized by the manufacturer and have various extents of silylation (regenerable sorbent described later were functionalized in the lab). SCC-3 was also provided in a variety of agglomerate sizes (Figure 5.1); however, the DLS indicated that the base particle size (79-89 nm) is identical for all agglomerates. The DLS also indicated that 98% of the agglomerates are in this range after sonication. About 2% of the particles remain agglomerated after sonication (no filtration), with a mean diameter of 2.1-2.6 μm.

Nitrogen sorption experiments indicate that the particles are primarily microporous as well as macroporous, with little mesoporous character. Representative isotherms are shown in Figure 5.2. The micropores (steep part of the curve at low relative pressures) arise through the agglomeration of small base particles so that the space between these base particles facilitates the capillary condensation of nitrogen. Upon functionalization (comparing SCC-0 and SCC-3 in Figure 5.2), the microporosity is

Table 5.1 Surface area and composition of aqueous mercury sorbent particles.

Sorbent	BET surface area (m^2/g)	mass% sulfur
SCC-0 (no thiol functionalization)	209	0
SCC-2	132	3.0
SCC-3	83	3.7

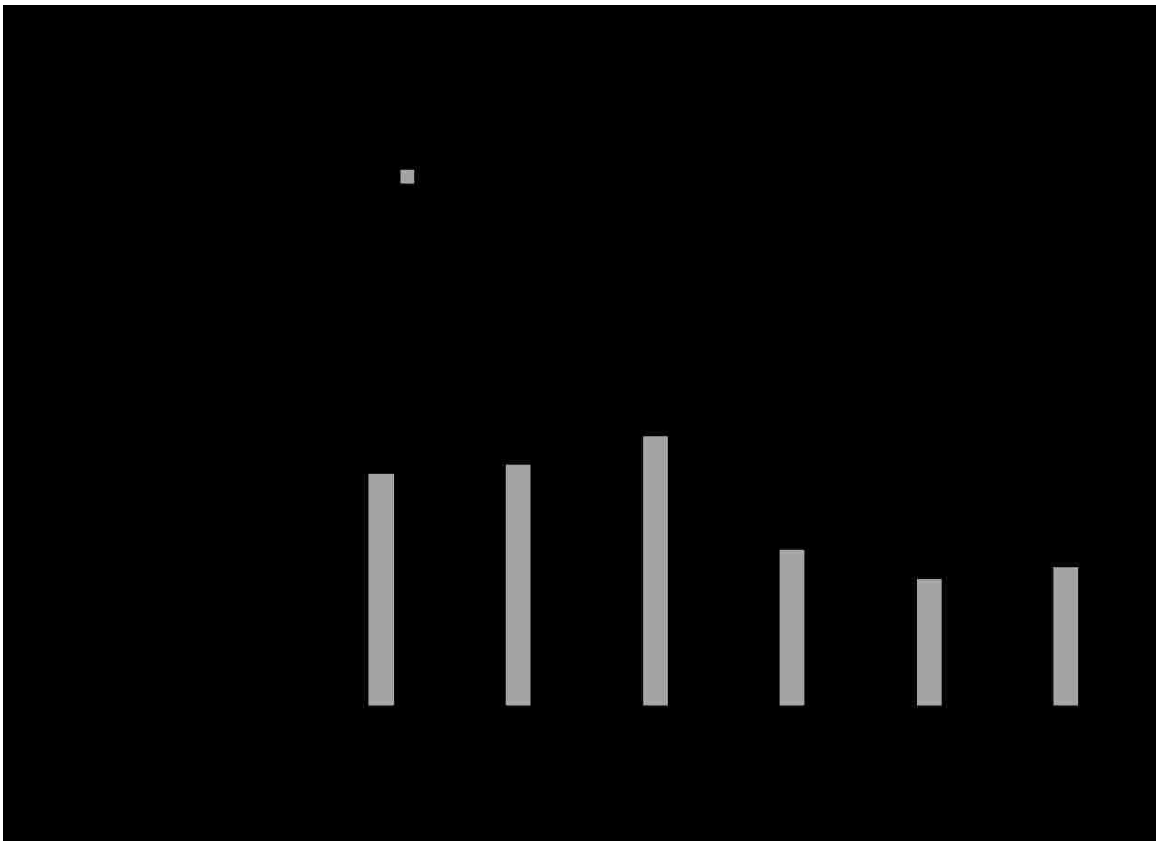

Figure 5.1 Agglomerate size ranges for various types of SCC-3 sorbent particles. The base particles of all agglomerate size ranges is the same 80-90 nm.

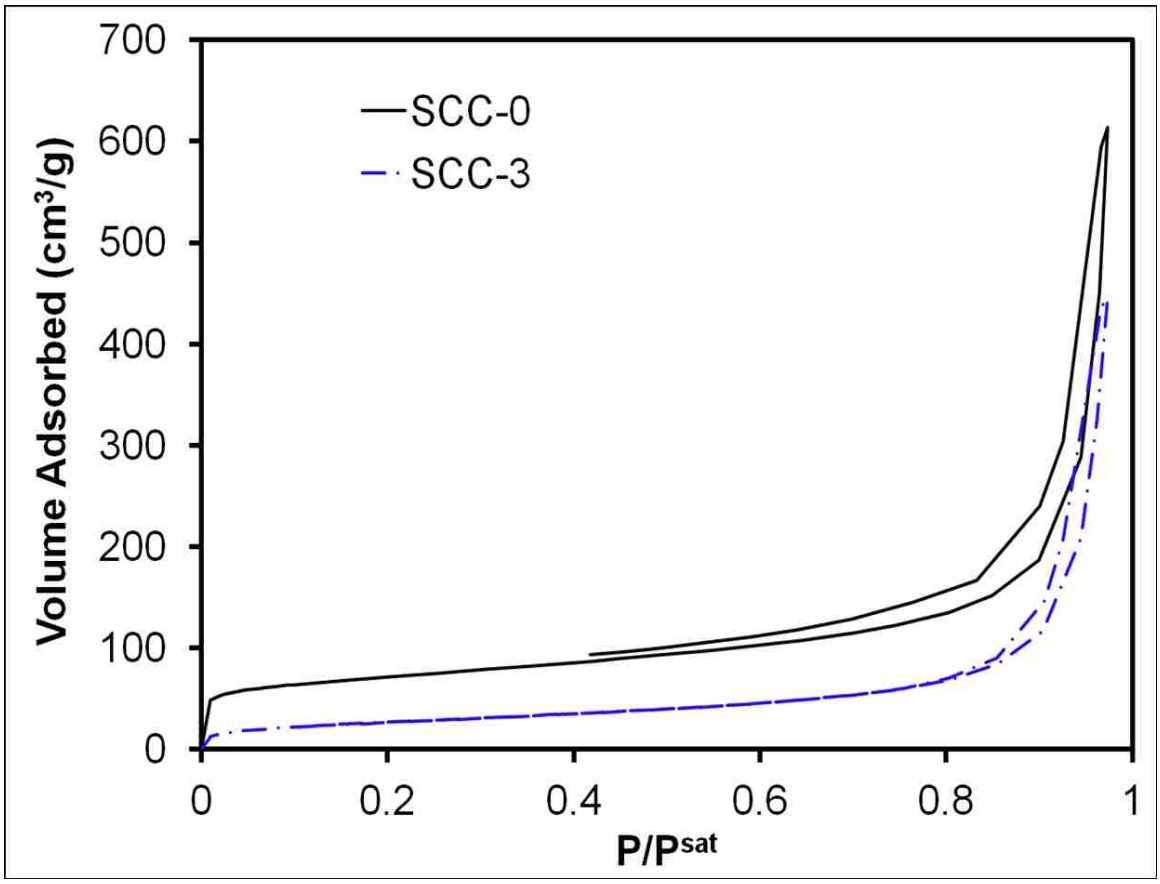

Figure 5.2 Nitrogen sorption isotherms for aqueous mercury sorbent particles.
Data indicate primarly micro- and macroporous nature of the particles. SCC-3 refers to non-aggregated SCC-3 particles. SCC-0 are unfunctionalized sorbent particles.

greatly reduced due to pore-filling by the silane. The macroporous nature arises from the interparticle spacing. Functionalization with the MPTMS decreases the overall BET surface area by about half (Table 5.1), as the silane can fill the pores as well as coat the entire surface, reducing nitrogen sorption capacity of those small metal oxide pores.

Thermal experiments indicate that the sorbent particles are thermally stable and can also be used to determine the composition of the sorbent particles. Figure 5.3 is the TGA of SCC-2 particles compared to unfunctionalized (SCC-0) particles. The unfunctionalized particles show an evaporation of water to just above 100 ºC, and no further mass loss until above 400 ºC. This loss is due to combustion of the carbon core of the material, where the weight loss occurs over a very broad temperature range, which has also been reported by previous studies.[20] The metal oxide coating prevents efficient combustion of the carbon core at lower temperatures. The DSC (Figure 5.4) indicates two transitions within the silane layer, when compared with DSC for unfunctionalized sorbent material (SCC-0), which has a larger peak for the removal of water than the functionalized sorbent material.

Tranmission electron micrographs (TEM) indicate the heterogeneous nature of the sorbent particles (Figure 5.5a), and the overall carbon-silica composition is seen by the energy dispersive X-ray (EDX) spectrum (Figure 5.5b). The non-uniform silica coating renders a material which has both hydrophobic and hydrophilic surface properties, with the added benefit that the hydrophilic metal oxide coating can be functionalized.

The sorbent material (SCC-3) was found to be hydrolytically stable towards leaching of sulfur in dilute nitric acid at pH 5.5. This is expected since the siloxane bond formed by the silylation reaction is known to be stable between $2 < pH < 9$.[13] Only 1.5

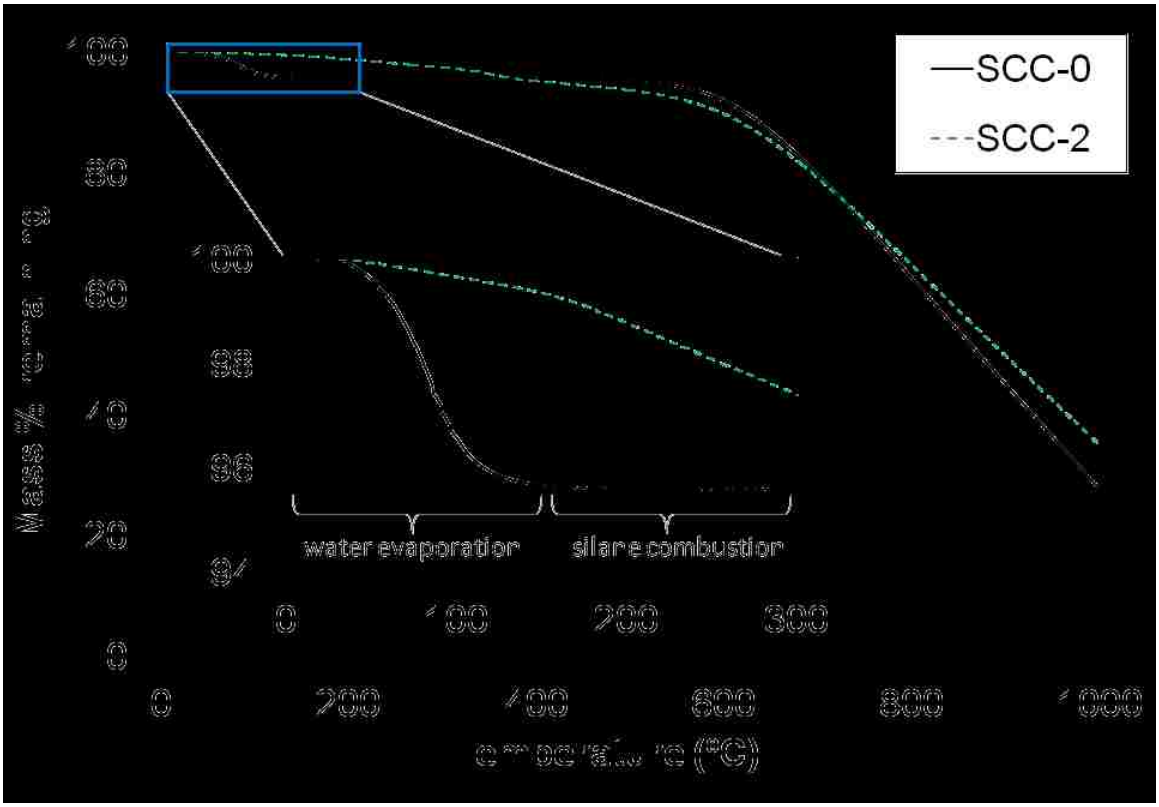

Figure 5.3 TGA of aqueous mercury sorbent particles.
Data indicate temperature stability of MPTMS functionalization to ~150 ºC followed by destruction of the carbon core at > 400 ºC.

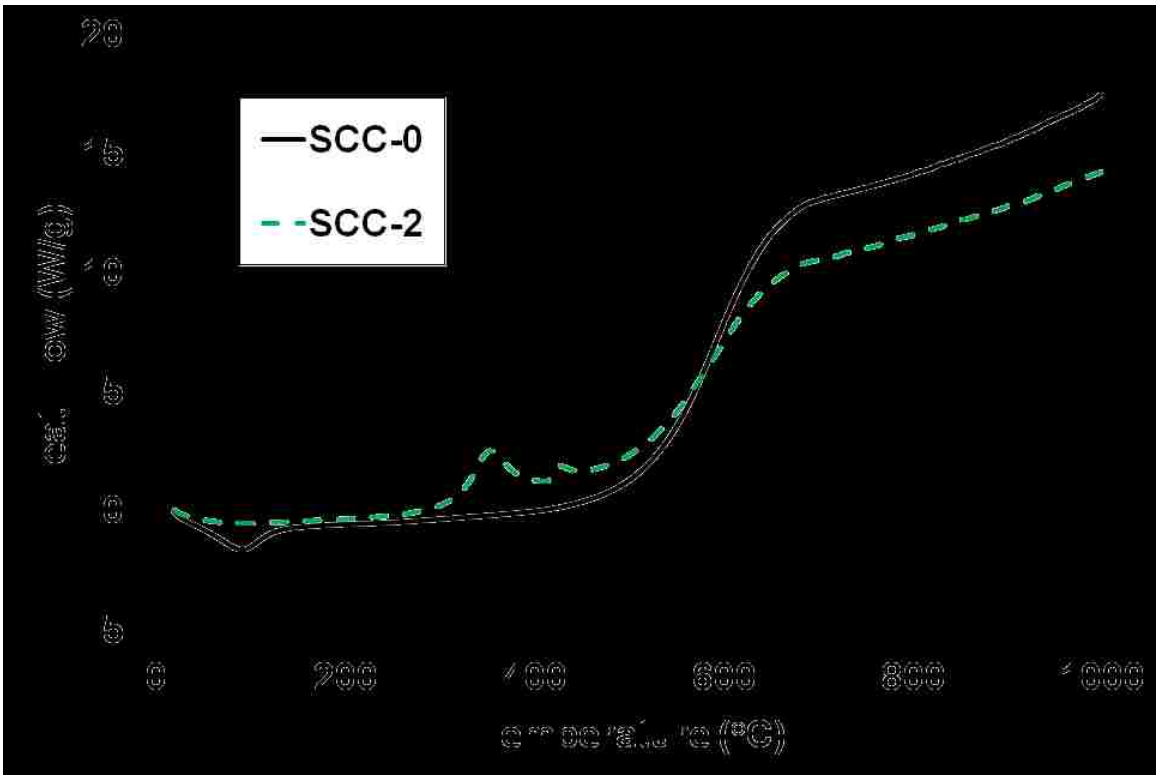

Figure 5.4 DSC of aqueous mercury sorbent particles.

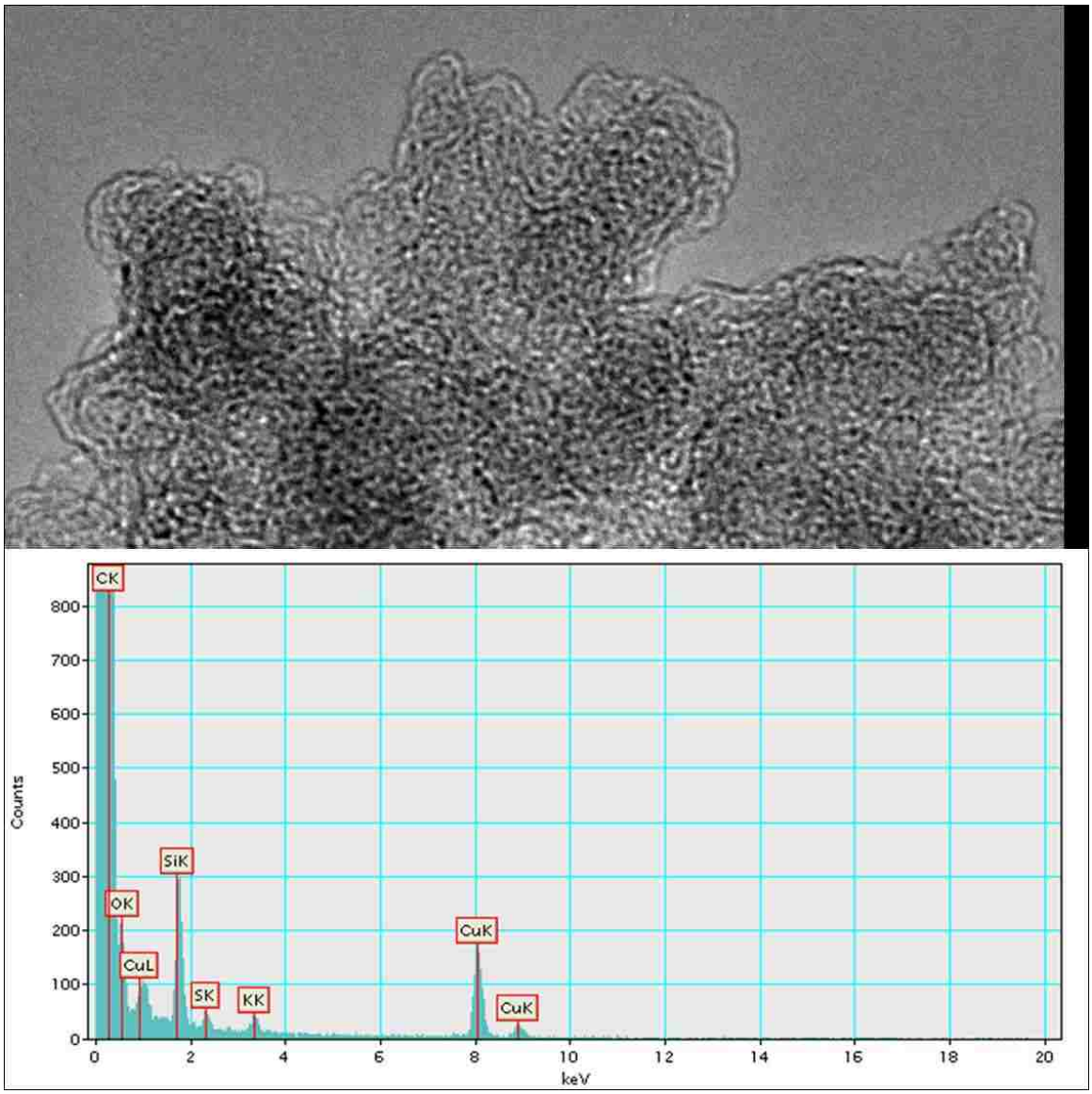

Figure 5.5 TEM of SCC-3 indicates overall agglomerate morphology and composition. (a) TEM of SCC-3 showing overall agglomerate morphology and carbon core. (b) Energy dispersive X-ray (EDX) spectrum indicating overall carbon and silica composition. Cu is present from the TEM grid. Accelerating voltage = 200 kV.

wt% of the sulfur was leached. The concentration of S in the leachate was only 2 mg/L, but the lowest practical detection limit of S in ICP is 1 mg/L.

5.1.2 Mercury sorption Capacity

The Hg sorption capacity of the sorbent materials for mercury was determined at various conditions (Table 5.2). The SCC-2 material was found to have a higher capacity due to the larger surface area, although it had less overall sulfur content. SCC-3 had a higher extent of functionalization and therefore was tested under several different conditions (such as at different Hg concentrations, pH values, etc). The capacities were consistent but lower than SCC-2 at the conditions tested. The results indicated in Table 5.2 are described in further detail throughout this chapter.

In addition to mercury sorption, silver sorption tests were done with these sorbents. The objective with these is not to remove silver from aqueous solution (though there are high-value applications for this), but in this case it is used as a probe for the number of thiol groups. Like mercury ions, silver is also known to have a very strong affinity for thiol moieties. Unlike Ag(I), Hg(II) is often present as a complex ion and also multiple oxidation states are possible with Hg ions. Also, Hg(II) can coordinate with two thiol groups near a pore mouth, blocking access to active sites within the pore. Little change in pH was observed with sorption of mercury due to coordination with the thiol moiety rather than ion exchange. For silver sorption, large pH changes were typical.

The SCC-3 particles had an average silver capacity of 39.6 mg Ag/g sorbent after 12 h. This is in agreement with the capacity found in the silver kinetics experiment (see "kinetics of sorption" discussion below) and reveals the total thiol surface accessible to be about 0.4 mmole thiol/g sorbent. From the elemental analysis of 3.7% S, it is

Table 5.2 Total aqueous mercury sorption capacity under various experimental conditions.

Sorbent	initial conc. (mg Hg/L)	pH	time (h)	Q (mg Hg/g)	Std. Dev. of Q (mg Hg/g)	Q (mol Hg/mol S)
SCC-2	183-200	6-7.5	6-18	70.48	12.41	0.45
SCC-3	83-150	5-6	6-18	34.47	4.79	0.15
SCC-3	11	5.8	12	56	NA	0.024
SCC-3	15	6.8	80	16	NA	0.069
SCC-3	22	5.8	12	16.8	NA	0.073

computed that there are 1.15 mmole thiol/g sorbent, meaning that only 35% of the thiol moieties are accessible to Ag(I) because of intraparticle diffusion limitations. These active sites are inaccessible within the agglomerate and so the silver capacity is considered the true equilibrium capacity for the agglomerate. Calcium(II) sorption experiments were also done to determine if some thiols had been completely oxidized to sulfonate moieties, and this was not found to be the case.

Sorption capacity was found to increase for increasing equilibrium concentrations of the supernatant (Figure 5.6). This linear relationship is described by sorption adsorption and desorption at the active thiol sites and the overall rate constant K ($=k_a/k_d$) is computed.

$$\text{Hg + site} \rightarrow \text{Hg·site},\ r_a = k_a C_{Hg} C_{site} \quad (5.1)$$

$$\text{Hg·site} \rightarrow \text{Hg + site},\ r_d = k_d C_{Hg-site} \quad (5.2)$$

At equilibrium, the rates of sorption and desorption are equal, and the fraction of occupied sorption sites is expressed as

$$\theta = \frac{C_{Hg-site}}{C_{site}+C_{Hg-site}} \quad (5.3)$$

Combining and arranging the equations gives:

$$C_{Hg} = \frac{1}{K}\left(\frac{\theta}{1-\theta}\right) \quad (5.4)$$

so that K (adsorption equilibrium constant) is determined by the slope of C vs. θ/(1-θ). In this case, θ (fraction of occupied sites) is computed from the determined capacity by noting that only 35% of the thiols are accessible (from the silver capacity) at equilibrium, using Eq 5.5.

$$\theta = \frac{q}{0.35 Q_{theor.}} \quad (5.5)$$

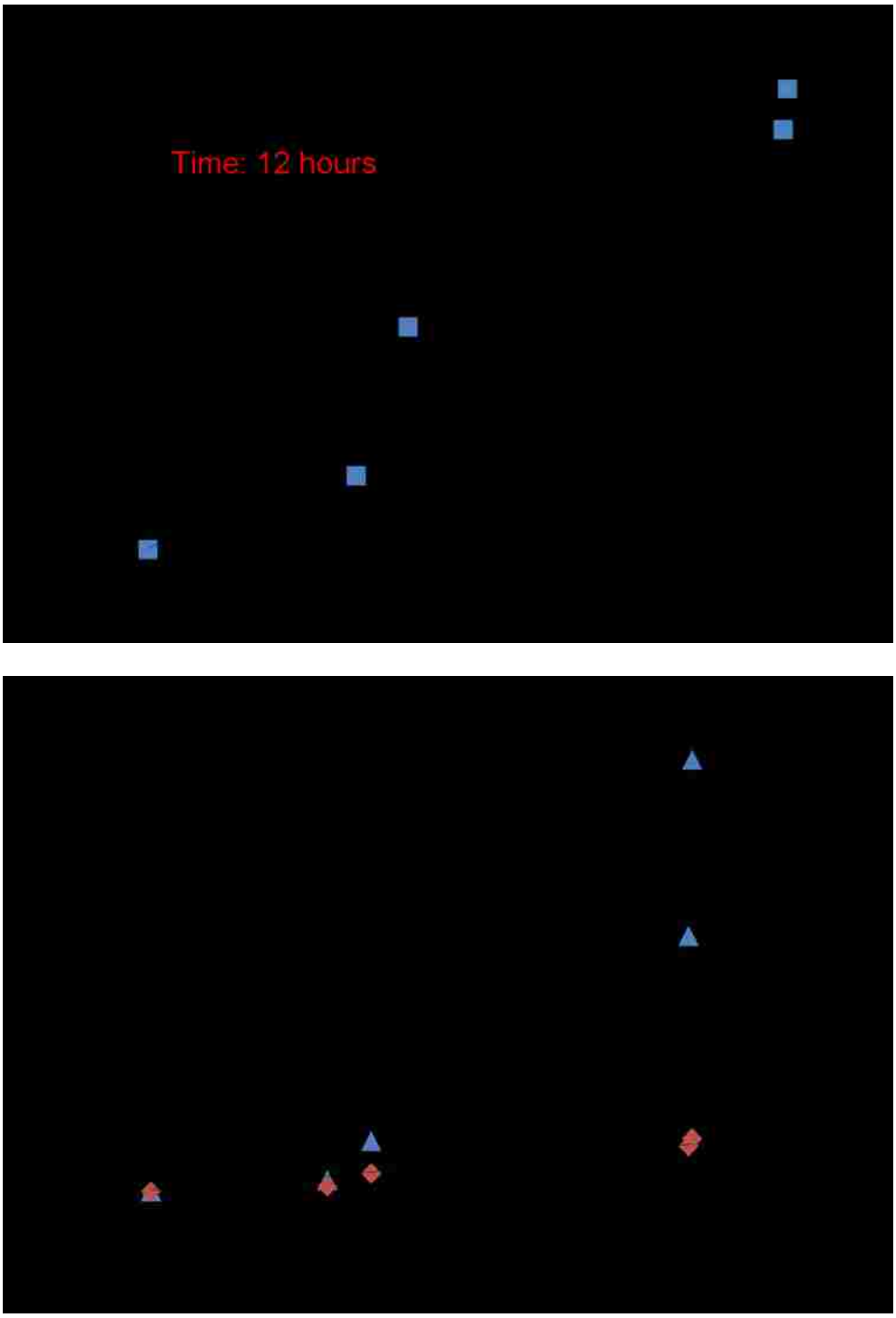

Figure 5.6 Aqueous mercury sorption isotherm.
(a) Equilibrium mercury sorption for SCC-3 indicates linear isotherm. (b) Fraction of occupied sites (θ) is used in conjunction with the adsorption and desorption rate laws to calculate overall sorption constant K (Equation 4-4).

Because all S was also found to be in reduced form (thiol), the theoretical capacity ($Q_{theor.}$) could be either 116 mg Hg/g (if 2 mol thiol binds to 1 mol Hg) or 232 mg Hg/g (if 1:1 thiol:Hg is assumed).

The capacity of the material increases for increasing pH as shown in Figure 5.7. This is presumably due to competition for sites with protons at lower pH values. It may also be due to changes in the mercury(II) speciation at increasing pH, such the presence of complex ion species containing more than one mercury atom adsorbed by a single site. Previous studies found constant or increasing sorption capacity with increasing pH: up to 4,[14] up to 6,[86] and up to 7.[87]

The total capacity (Table 5.2) of these materials is high, demonstrating that even at high concentrations of mercury they are efficient for removal. For these materials, capacities of up to ~70 mg/g were found at high Hg concentrations (~200 ppm). Previous studies of functionalized silicas have found a wide range of capacities, and these cannot always be accurately compared because of the variety of factors (synthetic conditions, pore morphology, particle size, silane layer thickness, etc) involved.

4.1.3 Kinetics of Sorption

Sorption kinetics was also determined for SCC-3 for Ag^{+} and Hg^{2+} (Figure 5.8). The relative rate of sorption for Ag(I) is higher than that for Hg(II) at similar concentrations, indicating that the Ag(I) is present as a smaller ion. It is likely that Hg(II) is adsorbed as a complex ion. Both Hg(II) sorption experiments reflect the effect of sorbent concentration on equilibrium capacity. Even for time up to 80 h, there is no further increase in capacity with additional time, at low concentration. Data also indicate

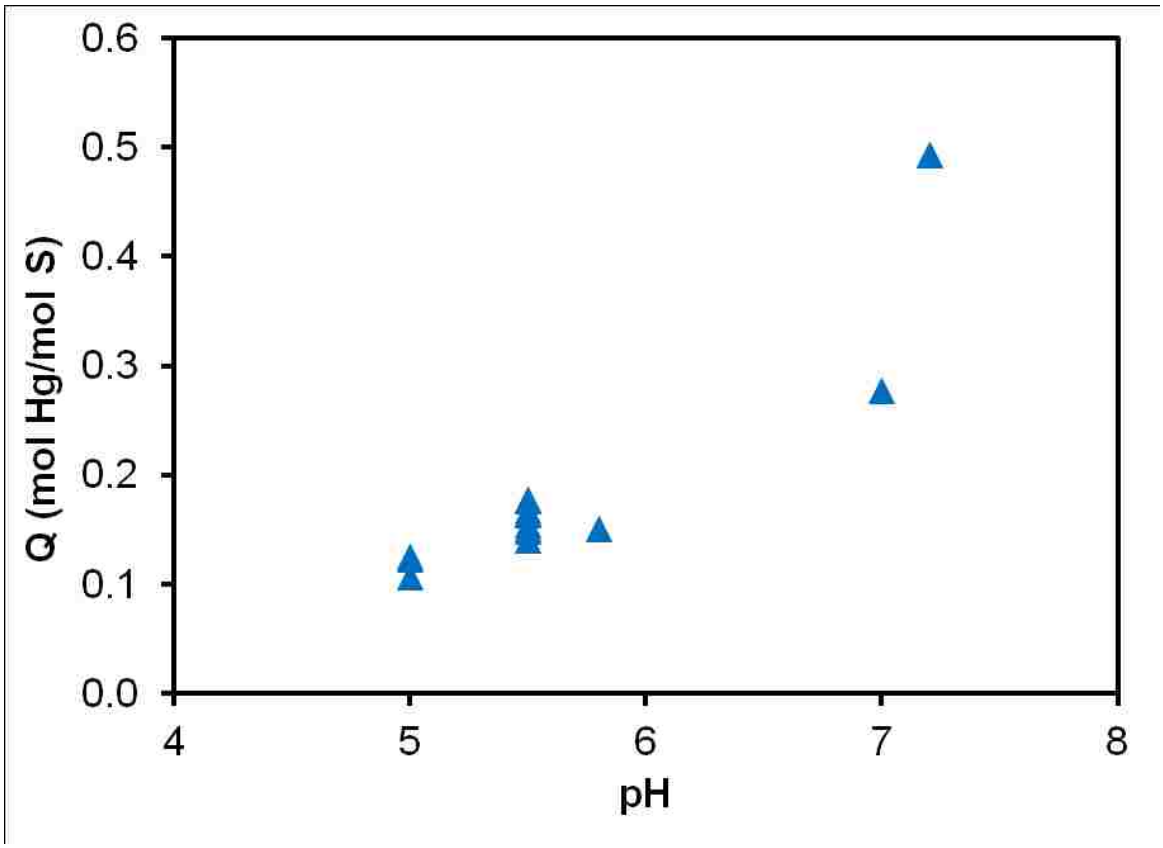

Figure 5.7 Aqueous mercury sorption increases with pH for SCC-3.
Sorbent equilibrium capacity increases in the pH range 5 to 7 due to less competition from protons and from potential changes in mercury speciation. SCC-3 sorbent. The scatter at a single pH value (such as 7) is not due to experimental error but to solution concentration, as capacity is also a function of concentration.

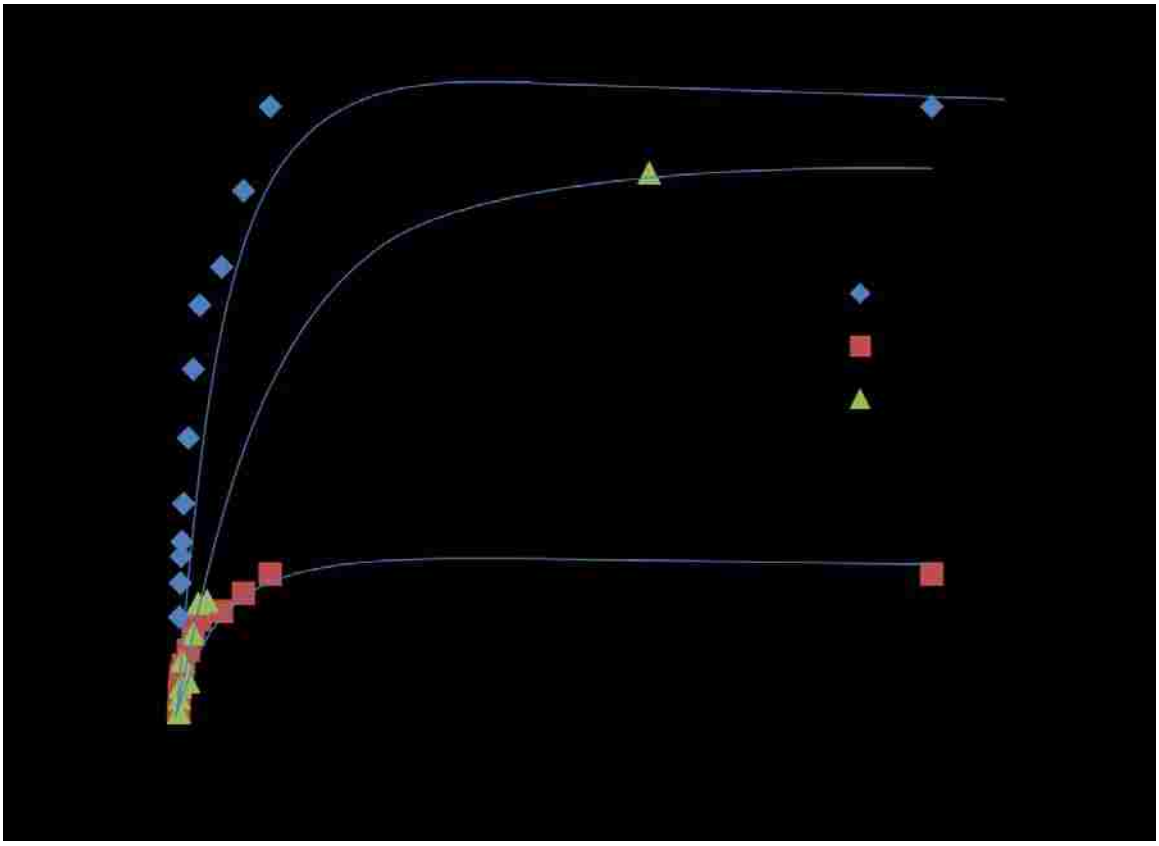

Figure 5.8 Aqueous mercury and silver sorption kinetics.
Ag (I) reaches equilibrium very fast compared to Hg(II). Hg(II) also reflects the effect of sorbent concentration on equilibrium capacity. Data also indicate that the total capacity at high concentration (in mmol/g) for Hg(II approaches that for Ag(I), demonstrating that the 1:1 thiol:Hg sorption is a valid assumption.
Parameters:
Sorbent: SCC-3
Ag: $pH_0 = 4.5$; $C_0 = 258$ mg Ag/L; 1 g sorbent/L
Hg Low conc: $pH_0 = 6.8$; $C_0 = 15$ mg Hg/L; 1 g sorbent/L
Hg High conc: $pH_0 = 7.0$; $C_0 = 129$ mg Hg/L; 0.5 g sorbent/L

that the total capacity at high concentration (in mmol/g) for Hg(II) approaches that for Ag(I), demonstrating that the 1:1 thiol:Hg sorption is a valid assumption.

Next, sorption kinetics were tested for the various agglomerate sizes of SCC-3 sorbent material: milled, aggregated, as well as non-aggregated (Figure 5.9). The larger "aggregated" sorbent particles were formed from the agglomeration of the fine particles, not agglomeration of the non-aggregated particles. The initial sorption rates of the three agglomerate sizes varied according to expected mass transfer limitations: milled SCC-3 > SCC-3 > aggregated SCC-3. Once the surface sites were initially occupied, diffusion to other sites continued at the same rate for all sorbent samples.

5.1.4 Real Water Testing of Sorbent

Real water testing in Oak Ridge National Laboratory indicated the usefulness of the sorbent for ground and process water treatment. The characteristics of the water and experimental column parameters are shown in Table 4.4. Even for the non-aggregated SCC-3 sorbent, the pressure drop was monitored and remained below 2 psig. The effluent from the columns was below the detection limit of 10 ng/L for the duration of the 4 month test; no breakthrough was observed. For the SCC-3 (non-aggregated) the sorption at this point was 0.225 mg Hg/g sorbent, two orders of magnitude below the total capacity of this material.

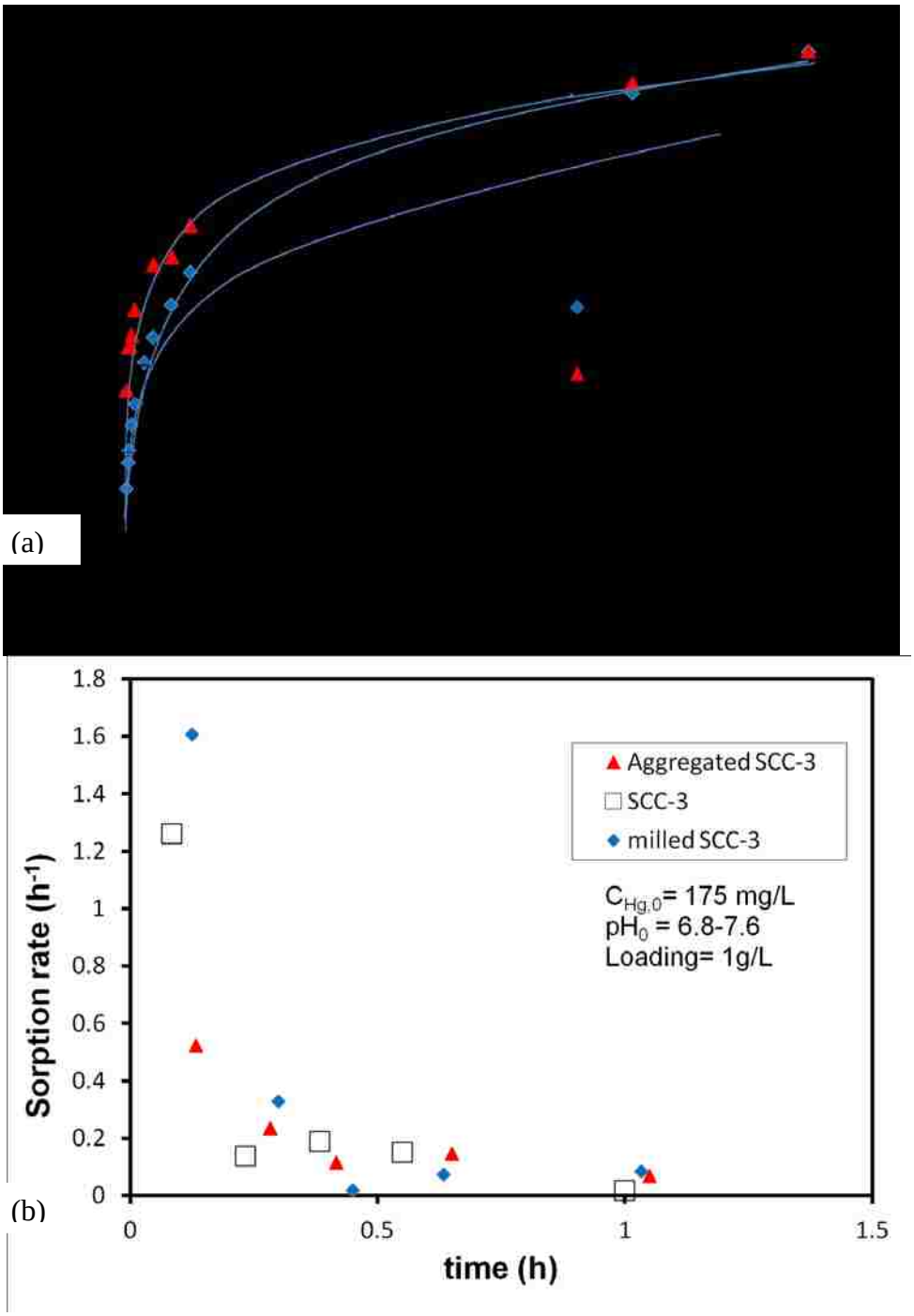

Figure 5.9 Aqueous mercury sorption kinetics for agglomerates of SCC-3 sorbent. (a) Details of agglomerate size range are given in Figure 1. (b) Dependence of initial Hg sorption rates ($-d(C_{Hg}/C_{Hg,0})/dt$) on sorbent particle size. The initial sorption rates depend on agglomerate size (milled SCC-3 > SCC-3 > aggregated SCC-3) but subsequent sorption rates are similar among all agglomerate sizes.

5.2 Regeneration of Sorbents

Rregenerable sorbents were prepared by the functionalization of silica-coated carbon with both a thiol moiety and sulfonate moiety. The thiol moiety is the active sorption site but the sulfonate moiety introduces some steric effects so that the adsorbate is not bound so tightly to the surface. The functionalized sorbent was prepared by the well-known silylation reaction with sulfonated silane (THSPS) and thiol silanes (MPTMS). Previous studies (discussed in Section 2.2.2) regenerated using more harsh conditions but in this study we have looked at potential regeneration using dilute HCl (pH ~4). The schematic is shown in Figure 5.10.

The density of thiol groups is given by Ag^{+} sorption before the addition of sulfonate moieties. Since there is a 1:1 Ag:thiol interaction, there is 0.18 mmol thiol/g sorbent (Table 5.3). Calcium(II) sorption is used to quantify the number of sulfonate groups but there is some non-specific sorption of Ca^{2+} in the absence of sulfonate moieties. Based on Table 5.3, there is 0.062 mmol Ca^{2+} sorbed/g due to the sulfonate only. Since there is a 2:1 ratio of Ca:sulfonate, this indicates that there is 0.12 sulfonate/g sorbent. Taken together, these figures indicate that the functional groups are about 60% thiol and 40% sulfonate. The Hg^{2+} sorption does not increase significantly for thiol only particles compared to sorbents with both thiol and sulfonate. After the sorption of mercury, both types of particles were washed in pH ~4 dilute HCl. For the thiol only particles, about 5% of the Hg was removed. About twice as much (10%) was removed for the sorbent with both thiol and sulfonate moieties. These results are promising

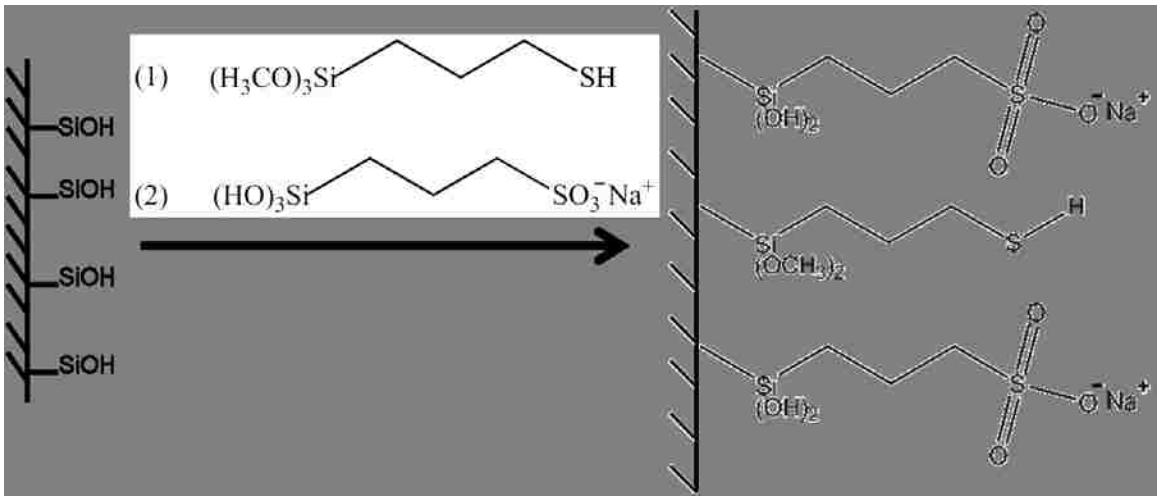

Figure 5.10 Schematic synthesis of regenerable aqueous mercury sorption particles. Regeneration capacity can be controlled by ratio of thiol to sulfonate.

Table 5.3 Sorption capacity of regenerable sorbents.

	Sorption Capacity (mg/g)			Sorption Capacity (mmol/g)		
Functional Group(s)	Ca^{2+}	Ag^{+}	Hg^{2+}	Ca^{2+}	Ag^{+}	Hg^{2+}
thiol only	0.98	19	23	0.025	0.18	0.11
thiol + sulfonate	3.5	29	26	0.087	0.26	0.13

because there is little sacrifice of mercury sorption capacity in order to synthesize these potentially regenerable sorbents.

5.3 Conclusions

Novel silica-coated carbon particles have been successfully functionalized and used for the development of high-capacity sorbents for dissolved mercury. The silica coating is very thin (< 5 nm) and non-uniform, allowing for exposure of both hydrophilic oxide and hydrophobic carbon surfaces. The particles are thermally and hydrolytically stable in the range of applicable temperature and pH values. The Hg sorption fits a chemisorptive model and indicates that the Hg:thiol ratio is 1:1. Regenerable sorbents were functionalized by incorporation of both sulfonate and thiol functional groups on to the particle surface.

6. Chapter Six: Mixed Matrix Membranes for Aqueous Hg Sorption

This chapter describes the facile synthesis and application of mixed matrix membranes (MMM) for aqueous mercury sorption. The first objective is the synthesis of MMM using the functionalized silica-coated carbon particles described in the previous chapter. The second is to analyze MMM behavior including flux and sorption capacity at various sorbent loadings. Finally, a model for the breakthrough curve of MMM is applied.

6.1 MMM Synthesis and Characterization

The MMM was prepared by phase inversion casting technique (Figure 6.1) using polysulfone as the polymer phase and SCC-3 (non-aggregated and milled size ranges) as the sorbent phase. However, particularly in the case of milled particles, the sorbent phase is better dispersed in the matrix so that the functional sorptive sites are more fully utilized. In phase inversion, the polymer such as polysulfone (PSf) is dissolved in a solvent, such as dimethylformamide (DMF) in this case. After casting the viscous polymer solution to the desired thickness, the polymer/DMF solution is immersed in a second solvent which is immiscible with the polymer phase.

The DMF inverts to the second solvent, leaving behind a solid polymer, which also in this case contains sorbent particles. The key to creating porous polymeric membranes by phase inversion is to remove the DMF fast, so factors that affect the DMF removal rate will affect the morphology of the membrane. These include evaporation time, temperature, relative humidity, and, in general, the choice of solvent systems.

MMM of up to 50 wt% particles have been prepared and successfully used. This is a high loading compared to MMMs with pure silica previously prepared in our lab.[45] It

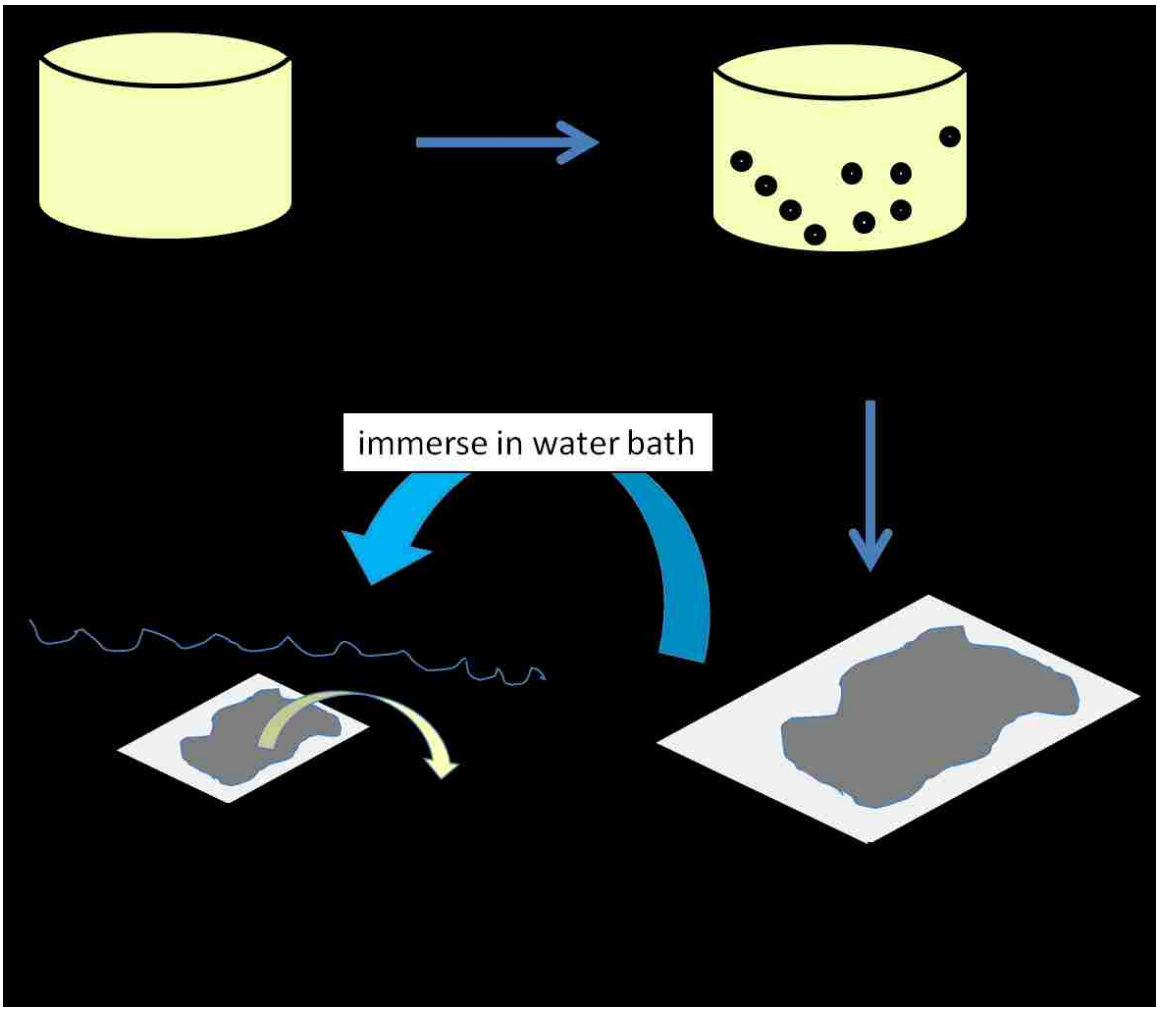

Figure 6.1 Mixed matrix membrane synthesis schematic.
The properties of the membrane are controlled by the kinetics of DMF inversion to the water phase.

is expected that exposed carbon black on the silica particles provides a more stable interface with the polysulfone matrix than pure silica. The membranes were mechanically stable up to pressures greater than 5 bar and water flux (J_W) was determined for two compositions.

From water flux data at various pressures, the permeability (A) can be computed for each membrane. The addition of sorbent particles to the membrane increases the flux in all cases due to disruptions in the polymer network. However, the effect of that increase with increasing weight fractions depends on the nature of the material. Figure 6.2 demonstrates three cases. The "thiol-silica-PSf" data is obtained from our lab's previous publication[45] on MMM, which used thiol-functionalized silica gel particles of about 3-20 μm agglomerate size. In this case there was a modest but linear increase in permeability. In the case of SCC-3 sorbent (average agglomerate size ~100 μm), there was a marked increase in doubling of the weight fraction, indicating that the large sorbent particles disrupt the polymer matrix. In order to increase the capacity of the membranes, SCC-3 milled particles (with a base particle size of ~80 nm) were used and there was no increase in the flux with increasing particle concentration. It is believed that this is due to both the particles' small size and the increased mechanical stability achieved when exposed carbon on sorbent particle surface is interfaced with the polymer matrix.

6.2 Mercury Sorption using MMM

The efficient removal of Hg from the feed solution by MMM of various compositions is shown in Figure 6.3, plotted as Hg(II) sorbed vs. Hg(II) passed through the membrane. The diagonal line indicates complete sorption of all Hg(II) passed. After all sorption sites are occupied, passage of additional Hg(II) yields no additional removal.

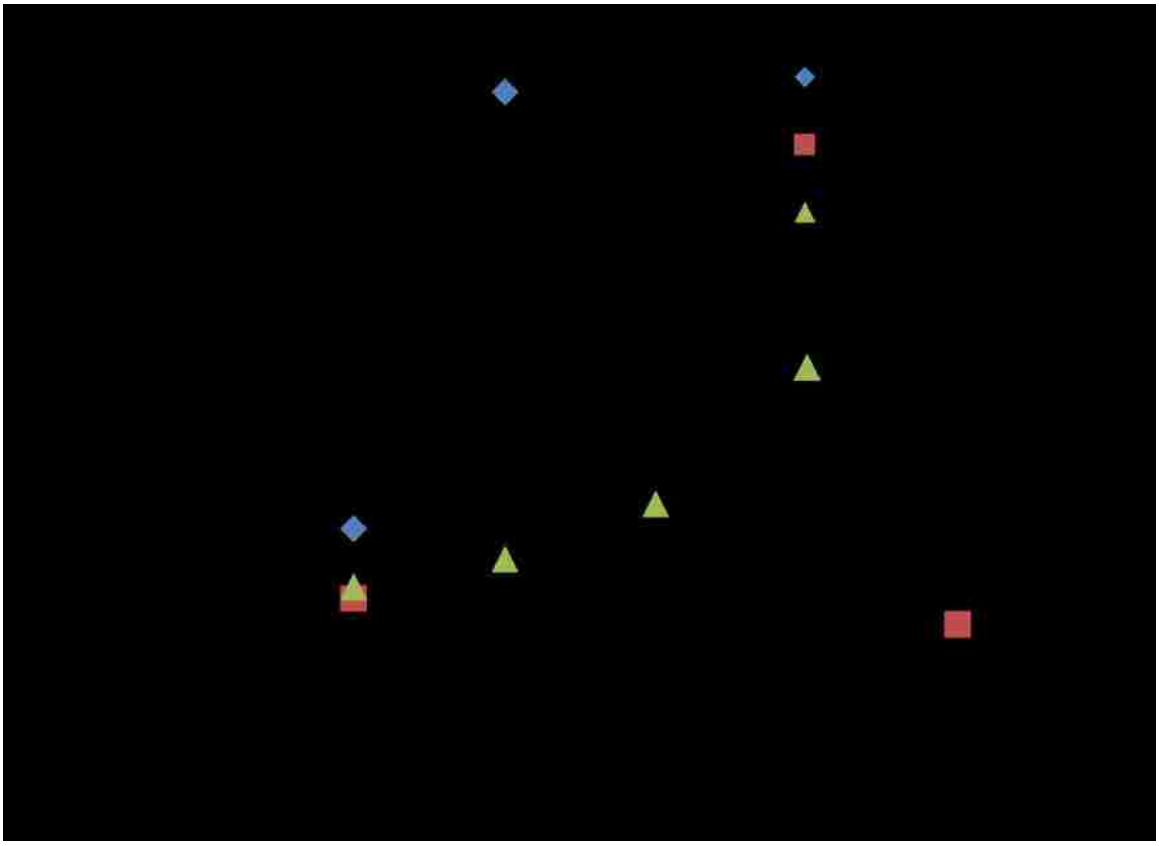

Figure 6.2 Mixed matrix membrane permeability.
The large agglomerates of SCC-3 create gaps within the polymer matrix, increasing the flux but decreasing the mechanical stability. The milled SCC-3 particles are much smaller and better dispersed so that the MMM is mechanically stable even at high loadings, with no increase in flux upon higher loadings. The thiol-silica-PSf particles show a similar trend has been observed for other thiol-functionalized particles (MPTMS-functionalized silica gel, agglomerate size 3-20 μm), from reference 15.

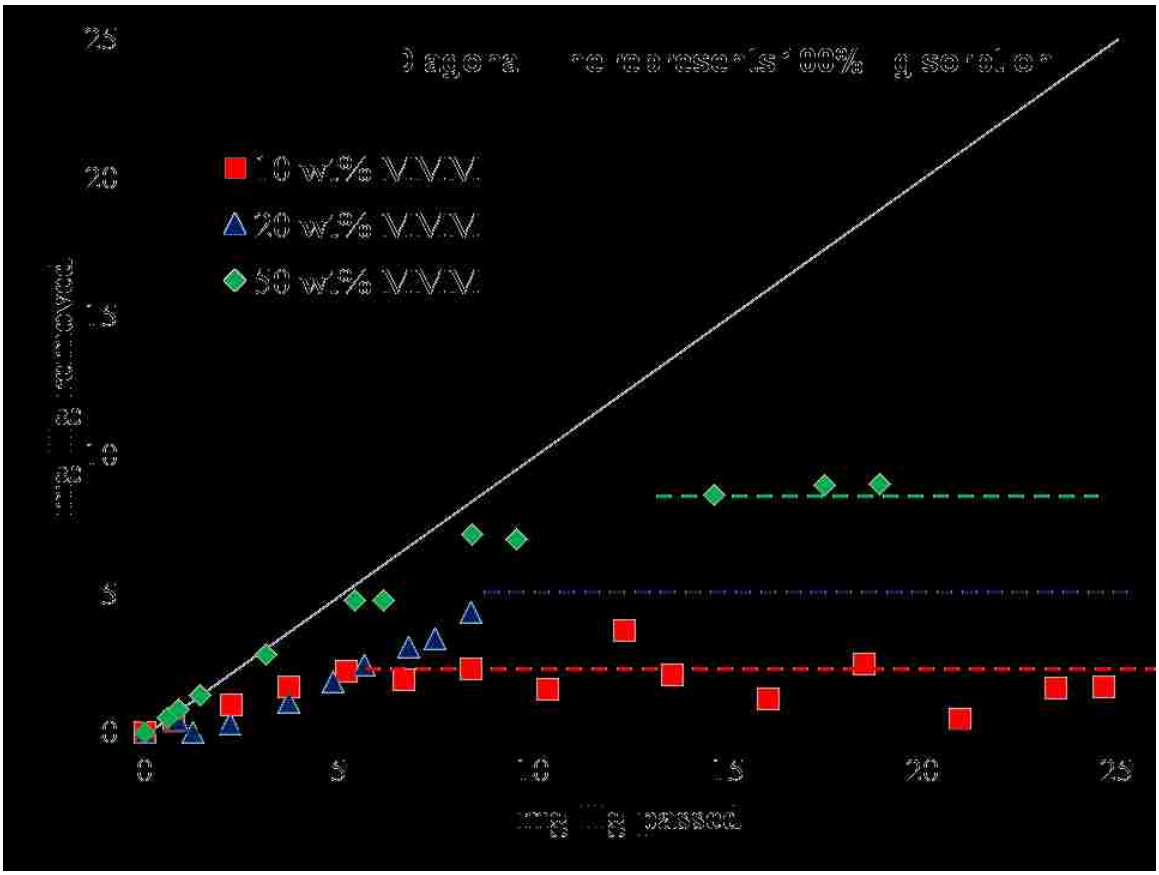

Figure 6.3 Removal of mercury using MMM platform with convective flow. MMM platform is PSf/SCC-3 milled. Cconvective flow demonstrates high capacity of the material and improved accessibility of sorption sites (due to dispersion of base particles through the membrane matrix) to achieve maximum sorption. Dotted lines represent maximum mercury capacity of thiol groups for each sorbent loading.

There is a high sorption capacity achieved because the milled agglomerate particles are well-dispersed within the porous polymer matrix, which decreases the mass transfer resistance, and more of the sorption sites are accessible. The total sorption capacity of the membrane approaches the theoretical capacity of the sorbent (which contains 3.7% S as thiol). The pure polysulfone control membrane showed only a small amount of non-specific sorption or Hg rejection.

6.3 Conclusions

The mixed matrix membranes (MMM) have been successfully synthesized with a high loading of silica-coated carbon particles which are functionalized for specific sorption of mercury. The presence of agglomerate particles disrupts the polymer matrix leading to a higher flux, but dispersed particles allow for the mechanical integrity to be maintained. The sorbent particles show high capacity for mercury sorption under convective flow, and using the MMM brings practical advantages to the mercury removal application.

7. Chapter Seven: Elemental Mercury Vapor Sorption

7.1 Material Characterization

Nitrogen adsorption at 77 K was performed on the blank silica precursor, the Cu-impregnated silica, and S-functionalized Cu-impregnated silica (Si-1) to examine the impact of functionalization on pore accessibility. The results for nitrogen adsorption as a function of relative pressure for all three materials are shown in Figure 7.1. All three isotherms exhibit Type IV behavior with condensation occurring in the mesopores at elevated pressures. The unfunctionalized silica, designated Si, and functionalized material, Si-Cu-S4, have the same shape. As expected, the functionalized material has a decreased volume in comparison. Interestingly, the copper-impregnated material (Si-Cu) exhibited a large increase in the volume of gas adsorbed. This is the result of enhanced surface roughness and the additional particles present after doping with $CuSO_4$. The Barrett-Joyner-Halenda (BJH) average pore size after functionalization with both Cu and S4 is 2.9 nm.

7.2 Fixed-Bed Hg^0 Capture

A summary of results for fixed-bed testing using pure sorbent beds (and the composition of the functionalized sorbents) is shown in Table 7.1. The total capacity of materials ranges from 9.7 to 20.0 mg Hg/g sorbent. This is a significant increase over the use of both activated carbon and Fe nanoaggregates for this application.[88] The highest capacity was achieved using 2.5 wt% Cu and 6 wt% S. A better understanding of the role of Cu and S can be gained through comparison of the various materials. The immediate impact of S is observed when comparing Si-2 and Si-3. For a constant level of Cu, the

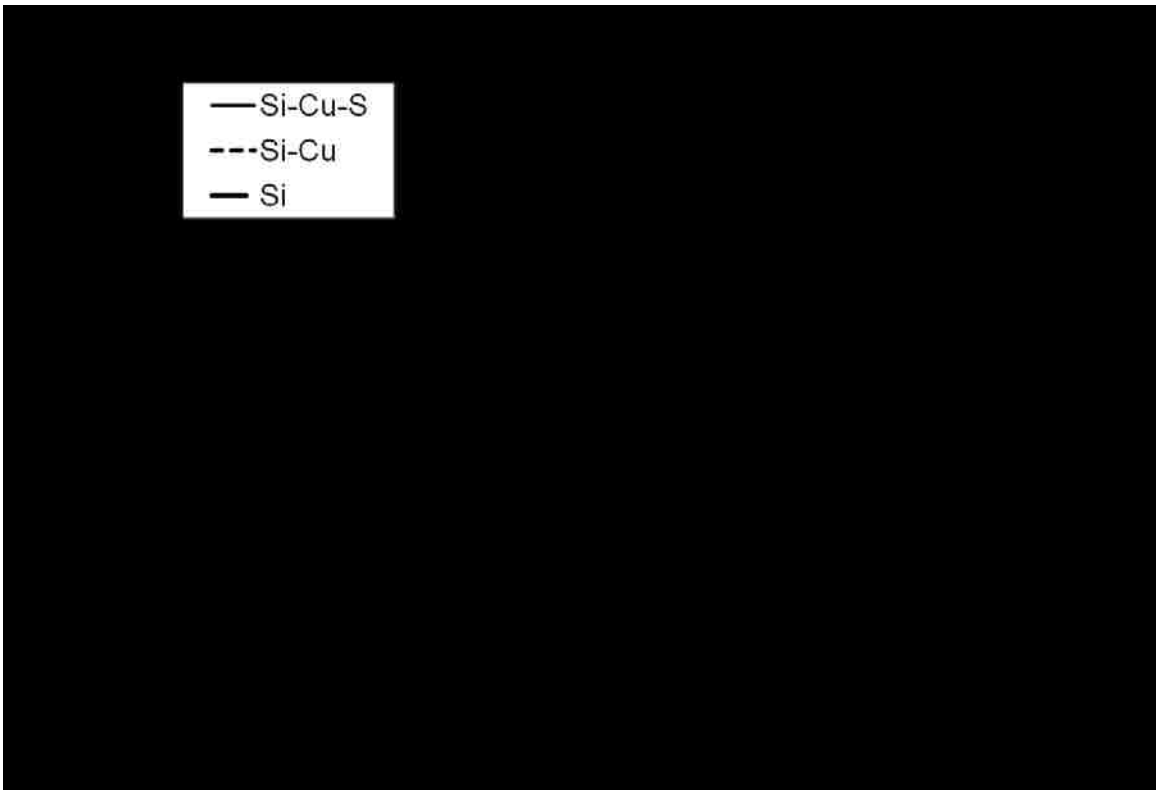

Figure 7.1 Nitrogen sorption isotherms (77 K) for mercury vapor sorbents.
Isotherms shown for the bare silica precursor (Si), copper-impregnated silica (Si-Cu), and fully functionalized Si-1 (Si-Cu-S4) showing a Type 4, multilayer adsorption.

Table 7.1 Summary of results for fixed-bed mercury vapor sorption.

Sample	% Cu	% S	Exhaustion time (min)	Capacity (mg Hg/g sorbent)
Si-1	2.5	6	12577	19.8
Si-2	5	3	10091	16.8
Si-3	5	1	6749	9.7
Si-4	3	3	17443	16.8

capacity of materials increases 72% from 9.7 to 16.8 mg Hg/g sorbent as the S level is increased from 1 to 3 wt%. Similarly, when comparing Si-1 and Si-4, the capacity increases 18% from 16.8 to 19.8 mg Hg/g sorbent as the sulfur content is increased from 3 to 6 wt%. These observations suggest that an optimal content exists around 3 wt% S because enhancement of capacity is much less pronounced beyond these levels. Variation of Cu at the levels tested showed no real impact. This can be seen when comparing Si-2 and Si-4 where the capacity is essentially unchanged while the Cu level is increased from 3 to 5 wt%. Based on previous work with Fe nanoaggregates, the minimal required level of Cu was around 1 wt%. Therefore, the optimal Cu level for the silica platform is approximately 3 wt%. The existence of optimal levels is sensible considering that elevated levels of functionalization will result in pore blocking and increased resistance to mass transfer.

The increased capacity of copper-containing functionalized silica support as compared to Fe nanoaggregates can be attributed to the increased number of surface groups for silanization and a much larger surface area for capture. However, some questions remain regarding the effect of Cu species on Hg capture. The silica-based materials were prepared using $CuSO_4$ as the source of copper while Fe nanoaggregates had Cu^0 deposited on the surface. As part of this project, materials were also prepared using alternative counter-ions, including hydroxide and nitrate, as well as non-copper doped samples to determine the importance of Cu for Hg separation. The alternative copper materials were found to have significantly decreased capacities for Hg of less than 1mg/g using similar compositions. The non-Cu materials could only achieve a maximum

capacity of approximately 0.4 mg Hg/g sorbent using the same S loading. Therefore, the presence of copper as $CuSO_4$ appears to have a beneficial impact on Hg capture.

7.3 Temperature Effects in Fixed Bed Sorption

The reason for the enhanced capacity when using copper sulfate might be based on a thermal transition that occurs for this material at approximately 140 °C after 30-60 minutes of heating. The transition is accompanied by a change in color from greenish blue to dark brown. Interestingly, the materials had low Hg sorption capacities unless heated to this transition point. If the Cu and S are forming a copper sulfide complex, the material will have an increased affinity for oxidation of Hg. The role of silanized S4 during this transition is not well understood.

To demonstrate the increased capacity with increased temperature for the Si-1 sorbent, fixed-bed sorption experiments were conducted at 70, 100, and 140 °C (Figure 7.2). Each experiment was run for 24 hours, rather than to exhaustion. However the mercury inlet was constant for all samples. As seen in Figure 7.2, the capacity was slightly increased at increasing temperature up to 140 °C. Also, in order to demonstrate that the changes were not just the result of changes in mercury flowrate (as if the emitter tube were being depleted of mercury over multiple experiments), a final experiment was performed again at 140 °C to verify the previous result. Sorption experiments were performed on diluted sorbent beds (with inert sand) and increasing termperature to 170 ºC slightly lowered the capacity.

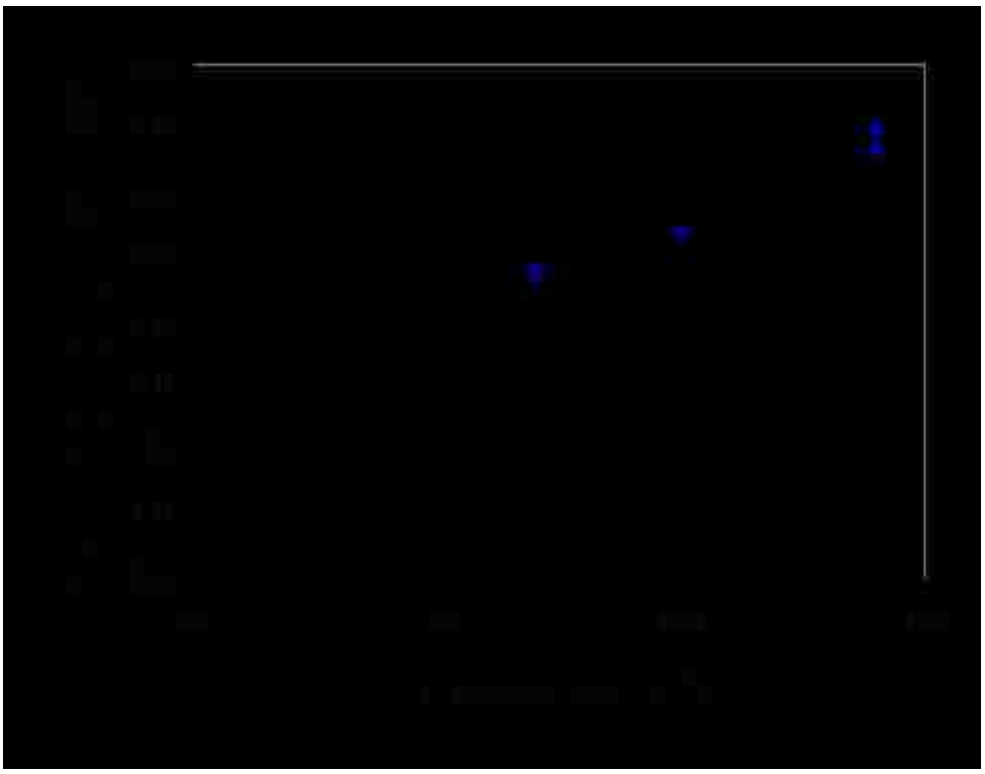

Figure 7.2 Sorption capacity increases with increasing temperature.
Increase due to chemisorptive mechanism and thermal effects in material at 140 ºC.

7.4 "Dynamic" Sorption of Mercury

In power plant applications, not only is total capacity important, but it is also important to have a dynamic capacity for fast removal of mercury. In order the demonstrate the sorbent performance in a dynamic environment, entrained-flow apparatus was used and compared to two other samples, that of conventional powder activated carbon (Darco) and that of silanized Fe/Cu nanoparticles, which were previously studied in our lab for mercury sorption. Figure 7.3 shows the outlet relative concentration of Hg, and the time required to reach steady-state removal for the sorbents. This figure shows that the Si-Cu-S4 functionalized particles perform nearly as well as the conventional sorbent in the dynamic sorption environment. Although the overall surface area is much lower than the activated carbon, the more open pore structure (Figure 7.1) allows mercury to reach the active sorption sites with less mass transfer resistance.

7.5 Leaching Studies of Sorbent

The use of sorbents for Hg capture by injection must be evaluated with regard to their potential environmental impact because they will be removed with the fly ash from coal-fired power plants. This is most important when considering the use of fly ash in concrete as a means of cost recovery for plant operations. If the use of a particular Hg sorbent would prevent the sale of fly ash for cost recovery, the actual cost of Hg removal using this material would be greatly increased.[89] A benefit of silica-based platforms when compared to PACs is that silica is already used in concrete blends to both reduce cost and improve mechanical properties. In order to continue the use of fly ash in concrete, a sorbent must demonstrate the ability to maintain chemical stability when exposed to a leaching environment and not degrade the quality of concrete when used.[90]

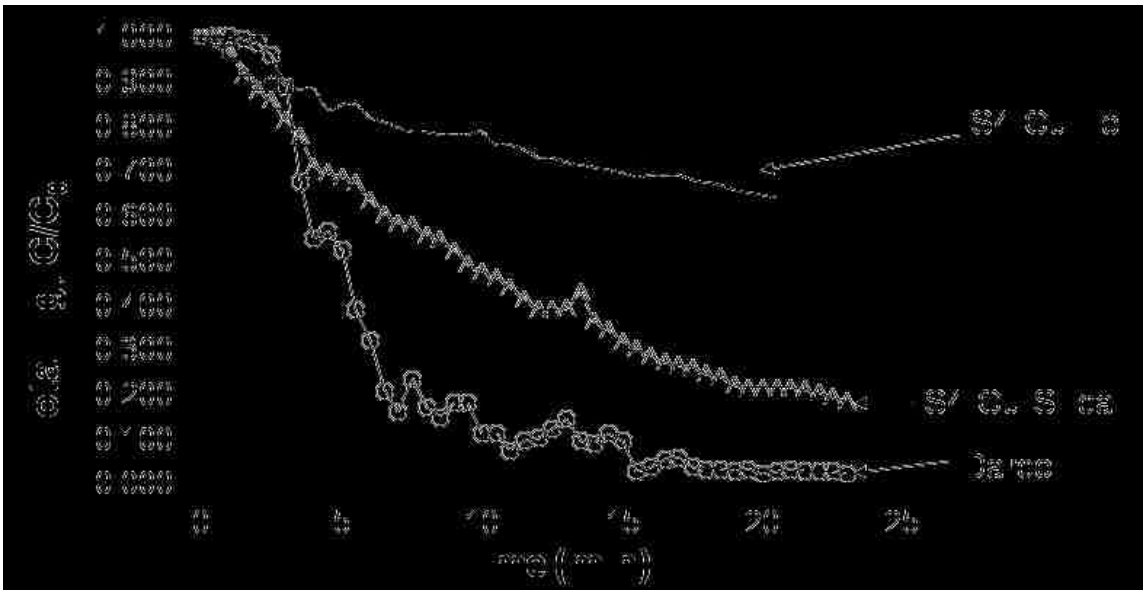

Figure 7.3 Injected-flow breakthrough curves for mercury vapor sorption.
These curves demonstrate the effect of surface area and pore structure on dynamic sorption.

The results for Hg leaching from Si-1 after Hg exposure were at the detectable limits of the machine, only 0.2 ppm Hg. This corresponds to a 0.4 % loss of the total Hg captured and indicates a possible strong affinity of Hg for the Cu/S site. The loss of Cu was much greater at 15.2% of the maximum possible, with 8.2 ppm leached for the given conditions. The amount of Cu leached merits some concern because it is approximately six times greater than the action level (AL) of 1.3 mg/L established for Cu by the U.S. EPA.

The actual compositions of concrete slugs tested are given in Table 7.2. For sample 3, the saturated sorbent was blended with fresh sorbent to better approximate power-plant applications where only a fraction of the total capacity is utilized during injection. The results for concrete leaching of both Cu and Hg are given in Table 7.2 as well, along with the maximum possible quantity of each. The quantities of both the Cu and Hg were below the detectable limit. For Hg, these results are consistent with leaching of the sorbent after Hg exposure and support the use of these materials in concrete processing. The improved Cu results in the presence of the concrete matrix suggest that concrete impregnation can be beneficial with regard to material disposal because it reduces the amount of leached Cu to well below the AL.

7.6 Formation of HgS-type product

The hydrolytic stability of the mercury in leaching studies is explained by the stable mercury-sulfur product which is formed. This is seen in both SEM-EDX (Figure 7.4) and X-ray diffraction (Figure 7.5) of exhausted sorbent.

The SEM image indicates that the exhausted sorbent is made up of various size agglomerates with a non-uniform elemental distribution. Very small particles (< 5μm)

Table 7.2 Leaching experiments composition and results.

Sample	Concrete mass (g)	Cement (wt%)	Fly ash (wt%)	Sorbent (wt%)	Max Cu (mg)	Leached Cu (mg)	Max Hg (mg)	Leached Hg (mg)
Exhausted Si-1		0	0	100	1.1	0.2	0.99	0.04
Sample 1	11.7	71.7	28.3	0	0	0	0	0
Sample 2	9.6	65	34.5	0.5	1.1	BDL	1.0	BDL
Sample 3	9.6	65	34.5	0.5[b]	1.1	BDL	0.1	BDL

[a] BDL: below detectable limit.
[b] The 50-mg sorbent sample consisted of 5 mg of saturated sorbent blended with 45 mg of fresh sorbent.

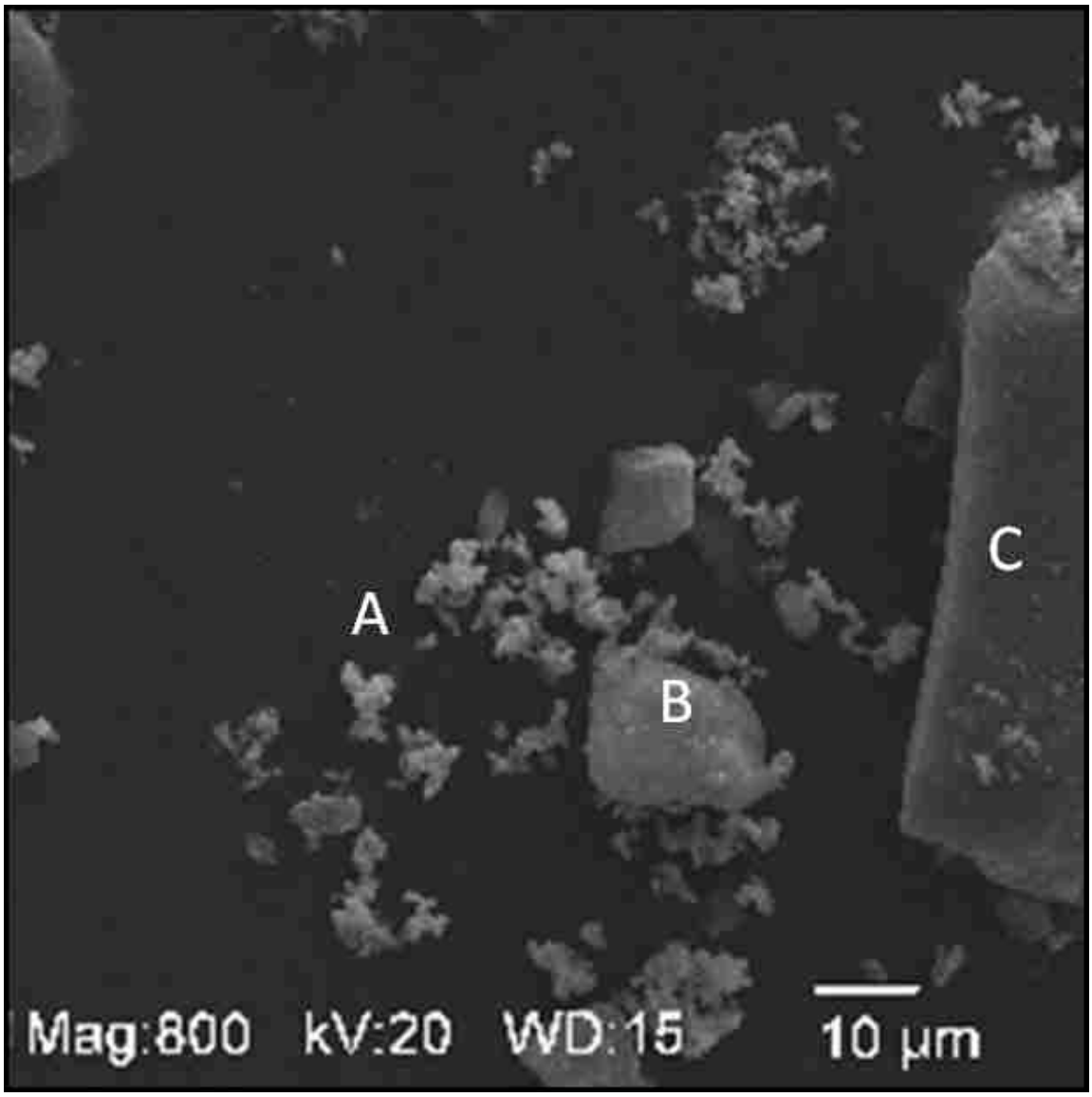

Figure 7.4 SEM image and EDX analysis of exhausted sorbent Si-1.
Nonuniform distribution of elements based on the EDX analysis for: (A) 3 wt % Si, 4 wt % Cu, 32 wt % S, 53 wt % Hg; (B) 41 wt % Si, 1.5 wt % Cu, 20 wt % S, 3 wt % Hg; and (C) 54 wt % Si, 1.6 wt % Cu, 16 wt % S, 4 wt% Hg.

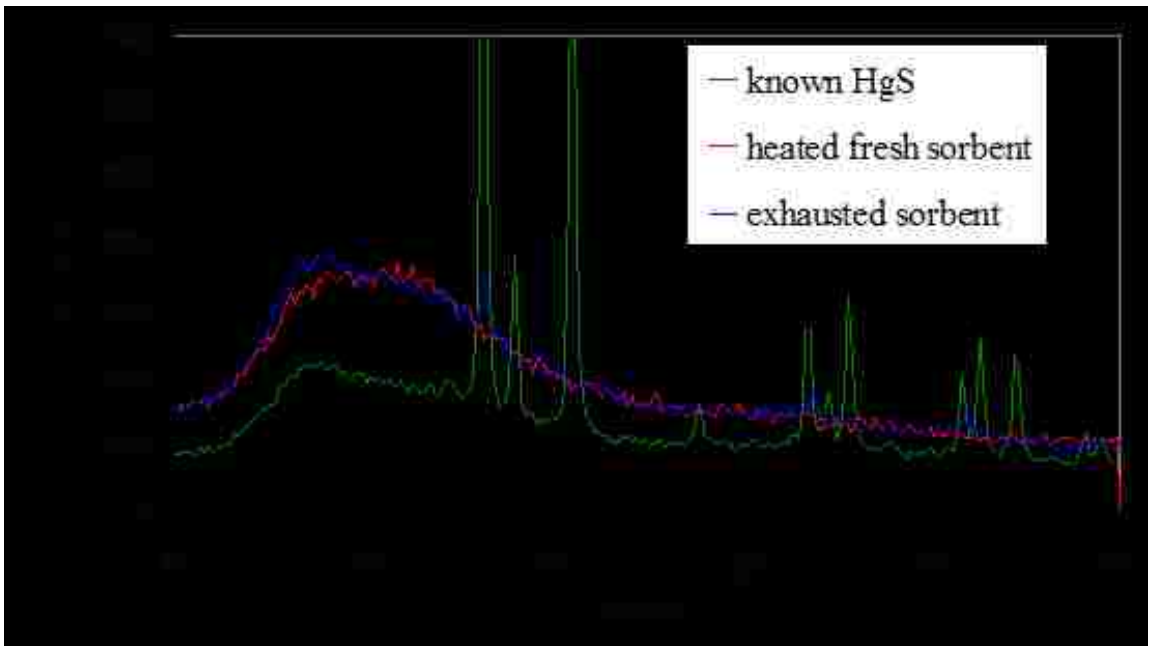

Figure 7.5 XRD of exhausted mercury vapor sorbent Si-1.
The exhausted sorbent is partially HgS with other crystalline species present.

contain the highest proportion of sulfur and mercury, while the larger particles are bulk silica with some surface mercury and sulfur. Although a mercury sulfide-type product is formed, this data does not indicate discrete particles of HgS. The Hg:S mass ratio in this compound would be about 6:1, but the overall mass ratios found for the various sized agglomerates are Hg:S values of 1.65 (A particles), 0.15 (B particles), and 0.25 (C particles). However, some of the product formed may be surface adsorbed HgS.

The XRD patterns verify the SEM-EDX data by comparing the crystal structures of unused (but heated) sorbent, exhausted sorbent, and pure HgS. The unused sorbent indicates very little crystallinity, due to the amorphous silica and very fine dispersion of copper sulfate, all of which has been silanized. After exhaustion, some crystal faces correspond to the known HgS. However, HgS is not the only species formed, because some known HgS peaks are not seen in the exhausted sorbent, and some sorbent peaks are not in HgS.

7.7 Performance with SO_3 present

Additional tests were performed using Si-1 to determine the impact of both the mass injection rate and the presence of SO_3 on Hg capture. The results are shown in Figure 7.6. Two trials were made at a mass injection rate of $1.2x10^{-4}$ g/L h, double the original test rate. The resulting steady-state removal of Hg ranged from 82-100%. The lower end of the range is the same as the results for the original mass injection rate, which is further support that the adsorption process is mass transfer controlled. The diatomaceous earth/sorbent blend used for trial 2 was then subsequently used for Hg capture in the presence of 20 ppm SO_3 at a mass injection rate of $1.2x10^{-4}$ g/L h. The SO_3 was generated by injecting a dilute sulfuric acid solution into a tube furnace. This

level is representative of the typical 1-40 ppm of SO_3 that is found in most flue gases.[13] It is believed that competitive sorption is the reason that activated carbon materials suffer a significant decrease in Hg capture when SO_3 is present because the concentration of SO_3 is much larger than Hg. The steady-state removal of Hg for Si-1 at this concentration of SO_3 was marginally impacted, again indicating the selective chemisorptive nature of the active site, and also confirms the usefulness of this sorbent in practical power plant applications.

7.8 Conclusions

Functionalized silica with tetrasulfur silane and doped with copper has been developed as a high-capacity chemisorptive material for elemental mercury vapor removal. Capacities as high as 20 mg/g sorbent have been developed with optimal sulfur content of 3%. Higher capacity was observed at 6% organic sulfur but the increase in capacity was not proportional, due to pore blocking and increased mass transfer limitations. The rate of adsorption ranged from 0.6 to 1.6 μg Hg/min depending on feed concentration. The steady-state removal was 82%, and the lack of increase in Hg removal when the injection rate is doubled suggests that pore accessibility is the rate-controlling step during dynamic Hg capture. Key benefits of this sorbent over conventional activated carbon were: the sorbent maintained performance in the presence of SO_3, the sorbed mercury and copper were stable during leaching tests, and the chemisorptive mechanism increased capacity with increasing temperature.

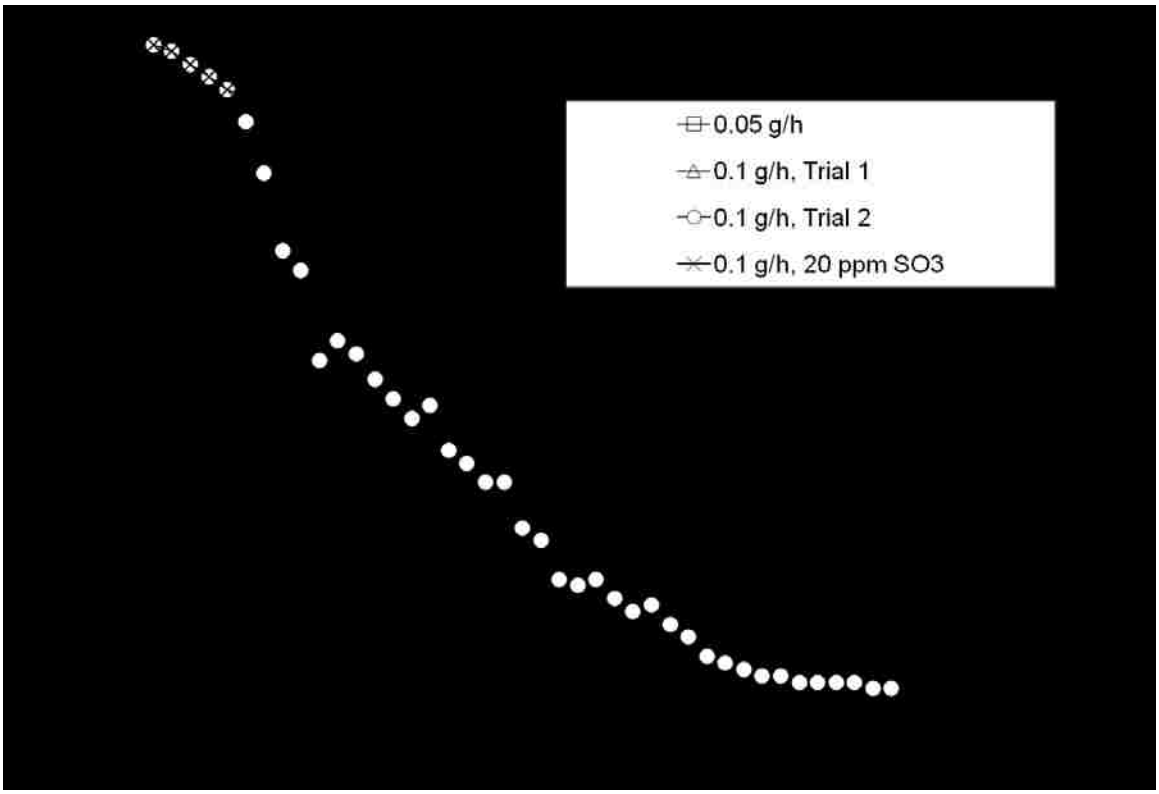

Figure 7.6 Injected-flow mercury vapor sorption in presence of sulfur trioxide.

8. Chapter Eight: Reactive and Catalytic Nanoparticle Synthesis

The two schemes presented in Figure 8.1 were used to synthesize silica-based Fe nanoparticles and ascorbic acid-stabilized Fe/Pd bimetallic nanoparticles. The first objective of this research was to quantify the silica functionalization, to characterize the Fe NP and the oxidized Fe NP (for dechlorination), and to demonstrate the utility for dechlorination. The second objective was to synthesize, characterize, and demonstrate the reductive dechlorination of the ascorbic acid-stabilized Fe/Pd bimetallic particles. These are also compared and contrasted with results from similar recent studies to show key outcomes.

8.1 Unfunctionalized Silica Characterization

Two types of silica (Table 8.1) were functionalized with 3-(trihydroxysilyl)-1-propanesulfonic acid ("THSPS"). One type of silica used is Ludox TM-50 colloidal silica from Grace Corp. The manufacturer reported these to be monodisperse 22 nm silica spheres, and SEM measurements as well as dynamic light scattering measurements performed in our lab confirm this. This type of colloidal silica has no intraparticle pore structure, only gaps between particles. The surface area (A_S) of 22 nm solid silica spheres (r = 11 nm), assuming no aggregation, is computed geometrically (using density, ρ, of 2.65 g/cm^3) to be 103 m^2/g.

$$A_S = \frac{4\pi r^2}{\frac{4}{3}\pi r^3 \rho} = \frac{3}{r\rho} \quad (8.1)$$

However due to aggregation during the required drying to nitrogen sorption measurements, the BET surface area was computed to be 87 m^2/g. The other type of

Table 8.1 Structural characteristics of silica used as a platform for Fe NP synthesis.

		BET surface area (m^2/g):		
	Aggregate size (μm)	before functionalization	After functionalization	Fe NP-silica
Ludox	0.022	87	92	110
Silica gel	3.7	585	264	224

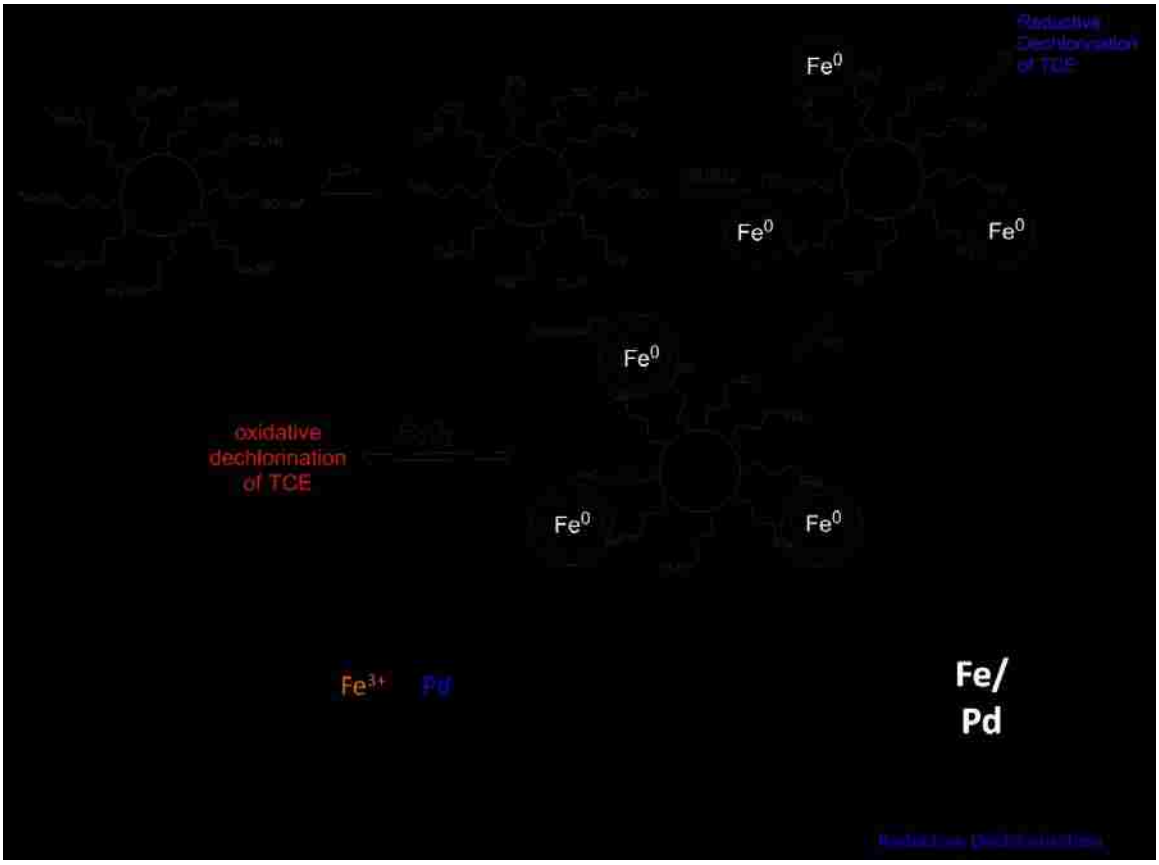

Figure 8.1 Schematic of NP synthesis.
(a) Silica-based synthesis for which two types of silica are used. (b) "green" synthesis of bimetallic particles where excess reducing agent inhibits oxidation as well as agglomeration of particles. In this reaction, ascorbic acid is oxidized to dehydroascorbic acid.

silica used is porous silica gel, with 3 μm particles, and a wide distribution of intraparticle pores (average diameter ~10 nm) has a BET surface area of 585 m^2/g.

8.2 Extent of Silica Functionalization

The extent of functionalization is determined through two methods, IR spectroscopy and TG analysis. For the Ludox, IR spectra (Figure 8.2a) indicate that 47 % of the silanol groups are reacted after sulfonate functionalization. For the silica gel, IR spectra indicate that 68 % surface silanol groups are reacted. These are consistent with previous functionalization results for these silica platforms in our lab.[81] Extent of silica functionalization (g silane / g silica or % silane) is computed from TGA (Figure 8.2b) data. Using the high temperature data of mass loss, the extent of silica functionalization is given by

$$\%\ silane = 100 \times \frac{(mass\ remaining\ of\ silica - mass\ remaining\ of functionalized\ silica)}{mass\ remaining\ of\ silica} \quad (8.2)$$

TGA indicates that the organic silane is 14.2 mass% of the functionalized Ludox particles. For the functionalized silica gel, silane is 18.4 mass%. Using the nitrogen sorption data, the sulfonate (silane) groups per nm^2 (α_{SO3}) is approximated, and the original silanol number (α_{SiOH}), before the functionalization, can also be theoretically calculated.

$$\alpha_{SO3} = \frac{sulfonate}{nm^2} = \frac{\%\ silane \times N_A}{A_S \times MW_{silane} \times 100 \times 10^{18}} \quad (8.3)$$

MW_{silane} is the molar mass of silane (202.26 for THSPS), N_A is Avogadro's number, and A_S is surface area of functionalized silica in m^2/g. Using these theoretical calculations, for functionalized Ludox, $\alpha_{SO3} = 4.6$ and for functionalized silica gel, $\alpha_{SO3} = 2.0$. The

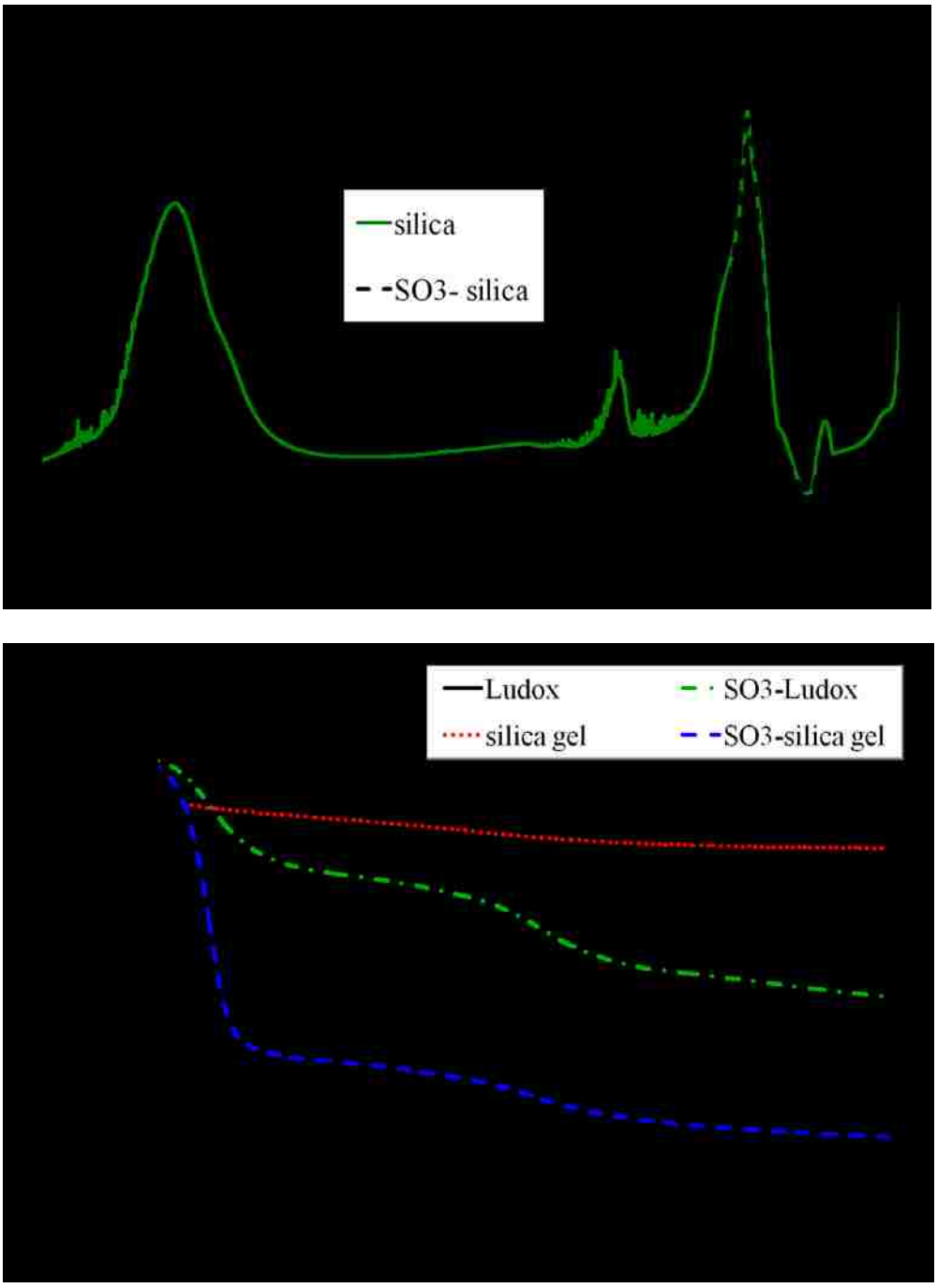

Figure 8.2 Two methods for determining extent of sulfonated silica functionalization. (a) Representative normalized FT-IR spectra for sulfonate-functionalized Ludox silica and unfunctionalized silica. The peak at 980 cm^{-1} indicates the surface Si-OH, which decreases upon functionalization. (b) Representative TGA for sulfonated silica samples. Heating rate: 10 ºC/min.

computed cross-sectional area of THSPS is 0.2855 nm^2 (using Chemicalize beta software, http://www.chemicalize.org). For silica gel, the $\alpha_{SO3} = 2.0$ is very reasonable, as two THSPS molecules would occupy a cross sectional area of 0.571 nm^2. However, for Ludox, the theoretically calculated $\alpha_{SO3} = 4.6$ is too large to occupy the silica surface, indicating the presence of multilayer silane network around the Ludox silica nanoparticles. Based on the number of number of silanol groups reacted (from IR data), and the TG data, it is possible to compute the original silanol number (α_{SiOH}).

$$\alpha_{SiOH} = \frac{silanol}{nm^2} = \frac{100 \times \alpha_{SO3}}{\%silanol\ reacted} \quad (8.4)$$

For Ludox, $\alpha_{SiOH} = 9.8$, and for silica gel, $\alpha_{SiOH} = 3.0$. The highest reported theoretical silanol number is 8,[13] again indicating that for functionalized Ludox, the silane is present as a multilayer network around the silica. For the silica gel, the silanol number is consistent with previous reports that have found α_{SiOH} values of 2.9 up to 3.6.[91]

8.3 Morphology of Functionalized Silica

Functionalization of Ludox doesn't significantly change the BET surface area (87 and 92 m^2/g), because the particles are non-porous. The nitrogen sorption isotherm (Figure 8.3a) indicates the similar morphology before and after functionalization. The silica gel has a wide size range of intraparticle pores, and functionalization narrows the pores of all sizes, as well as blocks many of the micropores (Figure 8.3b). The functionalization of silica gel decreases the BET surface area from 558 m^2/g to 264 m^2/g due to shrinkage and blockage of the pores.

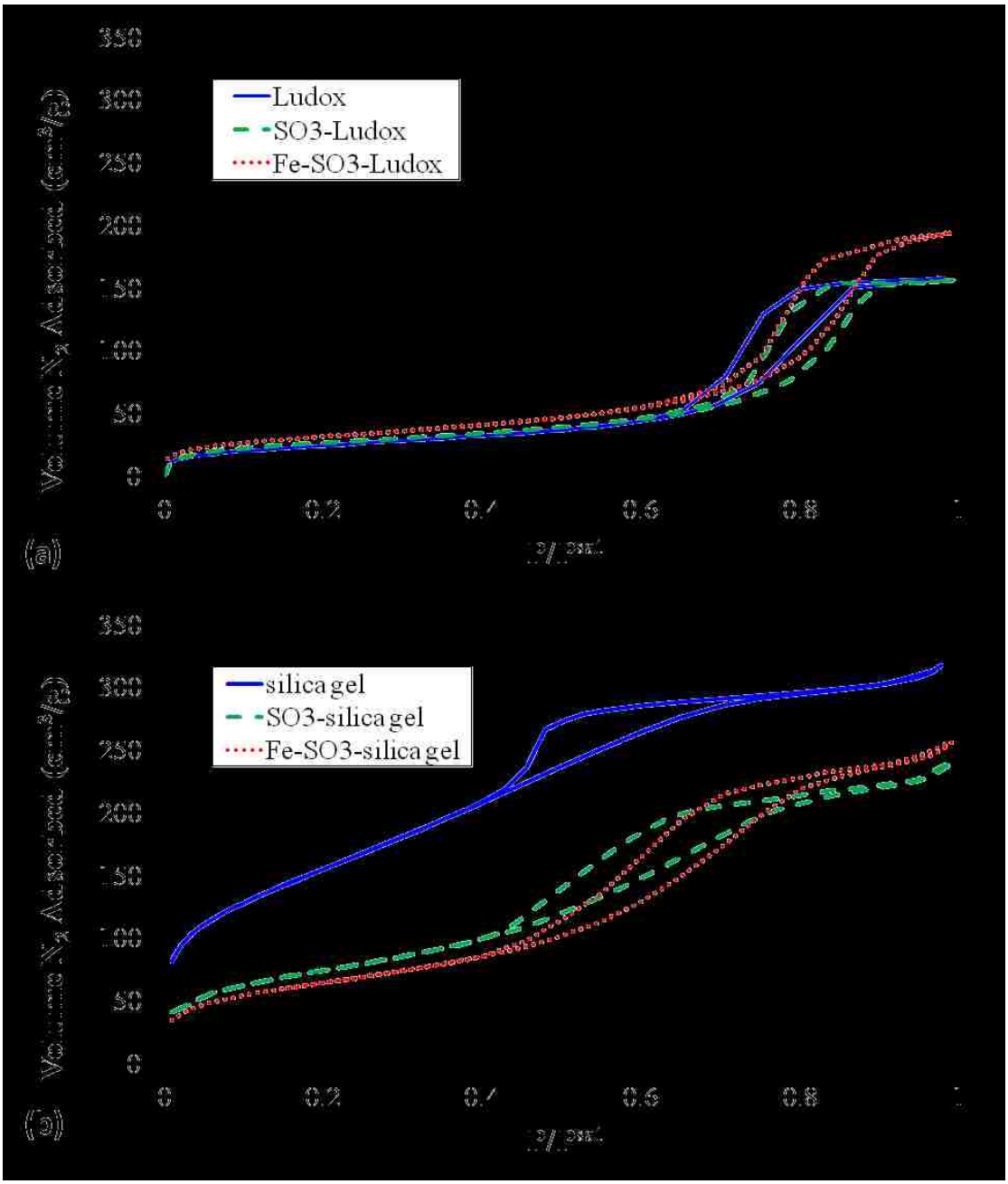

Figure 8.3 Nitrogen sorption isotherms (77 K) for sulfonate-functionalized silica. (a) Sulfonation of Ludox surfaces does not change the surface area or pore structure. Synthesis of nanoparticles (NP) increases microporous and macroporous surface areas, corresponding to sorption of nitrogen between non-porous NPs and sorption of nitrogen on surface of non-porous NPs. (b) Sulfonation of silica gel narrows pores of all sizes. Synthesis of nanoparticles (NP) decreases micropores, corresponding to pore blockage, and increases macroporous surface area, corresponding to sorption of nitrogen on surface of non-porous NPs.

8.4 Iron Immobilization on Functionalized Silica

The first step in synthesis of sulfonated-silica based iron nanoparticles is immobilization of the ferric ions. Both silica platforms indicate the same capacity of Fe^{3+}, about 7.0 mg Fe/g, or 0.125 mmol Fe/g. The immobilization of ferric ions is the same process as conventional sulfonated ion exchange resins. Dow's (Rohm & Haas) Amberlite has total capacity of 0.8 mmol ferric ion/g. However, functionalized silica gel has advantages of open mesoporous structure and also the further advantage of facile multifunctional silylation. The functionalized silica gel (2.0 sulfonate/nm^2) has 5.28 mmol sulfonate/g, indicating an experimental Fe:sulfonate ratio of 0.0237. The theoretical Fe:sulfonate ratio is 0.33, indicating that only about 7% of the sulfonate groups are ion-exchanged with Fe^{3+}. For Ludox, the experimental Fe:sulfonate ratio is 0.0295, or only 9% of sulfonate groups.

This process exchanges one Fe^{3+} ion for three Na^+ ions (subscript "s" means surface-bound).

$$Fe^{3+} + 3\ Na_S^{+} <=> Fe_S^{3+} + 3\ Na^{+} \qquad (8.5)$$

According to the law of mass action, which describes general exchange equilibria in ionized systems (for surface activity coefficients which are unity), the apparent equilibrium constant, $K^c_{Fe,\,Na}$, is given by

$$K^c_{Fe,Na} = \left(\frac{n_{Fe}}{c_{Fe}}\right)^{z_{Na}} \left(\frac{c_{Na}}{n_{Na}}\right)^{z_{Fe}} \qquad (8.6)$$

where c_i is the supernatant concentration [mol m^{-3}] and n_i is the exchanger-bound concentration [mol kg^{-1} exchanger]. Based on the observed Fe^{3+} supernatant and

exchanger-bound concentrations, the equilibrium constant for these functionalized silica platforms as 3.4×10^{-4} (g silica / L)^2.

8.5 Iron Particles on silica

Once ferric ions are immobilized on the sulfonate-functionalized silica, they are reduced to zero-valent iron particles using freshly prepared aqueous sodium borohydride. As it dissolves, the borohydride anion reduces water to hydrogen as well as reducing Fe^{3+} to Fe^0; borohydride itself is oxidized to various borate species. The formation of Fe^0 is physically seen as the silica suspension changes from white (silica with ions) to gray (silica with black Fe^0 particles. The agglomeration of the Fe NP (due to both electrostatic and magnetic forces) is limited by the immobilization of the iron on the silica surface and in the pores of the silica gel. The Fe NP with Ludox forms in the sulfonated silane network, resulting in Fe NP physically mixed with the colloidal Ludox silica NP.

Although the electrostatic interaction between Fe NP and sulfonate is less than that between Fe^{3+} and sulfonate, there is still some coordination between the surface atoms of the Fe NP and the sulfonate, which can also stabilize the Fe NP. As the sulfonate anion has various resonance structures, interaction with the Fe surface could occur by mono- or tri-dentate coordination, or through bi- or tri-dentate bridging (Figure 8.4). Little shift in the IR spectrum from sulfonate silane (THSPS; in water) to sulfonated Ludox silica indicates that the interaction occurs primarily through a tri-dentate coordination, whereby the asymmetric and symmetric vibrations are not impacted by the presence of the Fe atoms.[56] This lack of shift occurs is understood as the tridentate

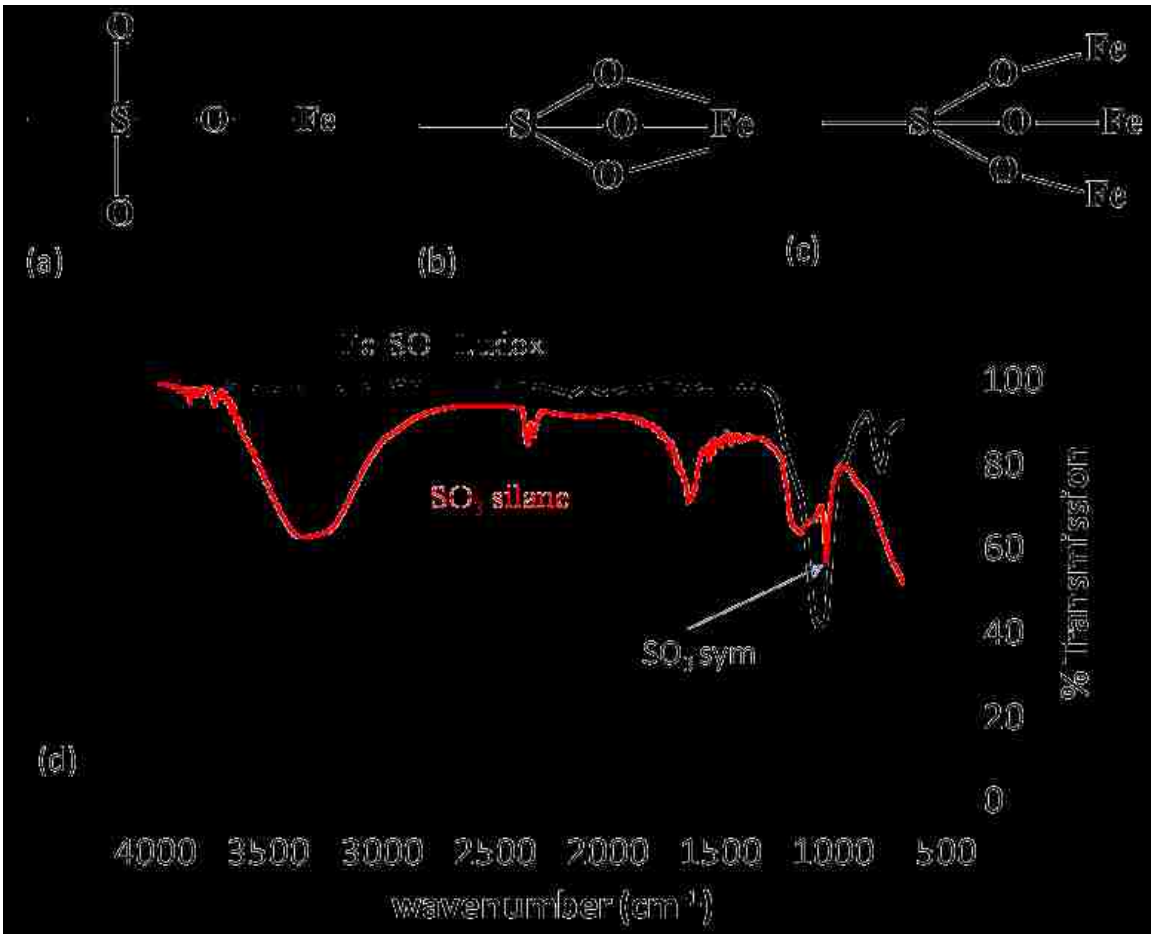

Figure 8.4 Possible modes of Fe interaction with sulfonate.
(a) monodentate chelating (b) tridentate chelating, (c) tridentate bridging. (d) ATR-IR spectra indicates that SO3 symmetric vibration does not significantly change upon Fe particle formation, indicating likely tridentate chelating due to small shift in symmetric vibration.

chelation retaining the same point group as the sulfonate.[92] Fe-phosphate interactions have also been found to occur similarly,[93] and this is further confirmed by the lack of an Fe-O-Fe peak at 845 cm^{-1}.[94]

Transmission electron microscopy (Figure 8.5) indicates that the iron nanoparticles are located both on the surface and pore mouths of the silica gel, as well as aggregated (apart from the silica surface) in chains that are typical of Fe^0 nanoparticles. Due to the sonication and drying during sample preparation, it is impossible to obtain a true image of the iron nanoparticles during the reactions. However, the particle size of ~50 nm can be determined and elemental analysis (energy dispersive x-ray spectroscopy, EDS) is used to show that they are indeed Fe^0 nanoparticles with a thin oxidized shell due to drying. EDS information alone does not indicate valence state, but the line-scan is used to show that the oxygen increases near the particle edges, when a thin layer of iron oxide would be the only material present. As the line scan proceeds across the particle, the oxygen content remains constant (from this oxide shell surrounding the particle of constant thickness) even as the iron signal increases due to the increasing depth of the iron core. The particles on the Ludox silica (Figure 8.6) also were found to be somewhat smaller (~30 nm). The silica nanoparticles are also on the order of that size (22 nm), they form a mixture of silica and agglomerated Fe nanoparticles. EDS line scan indicates that the particle composition is Fe (with Si also indicated because of the proximity to silica particles).

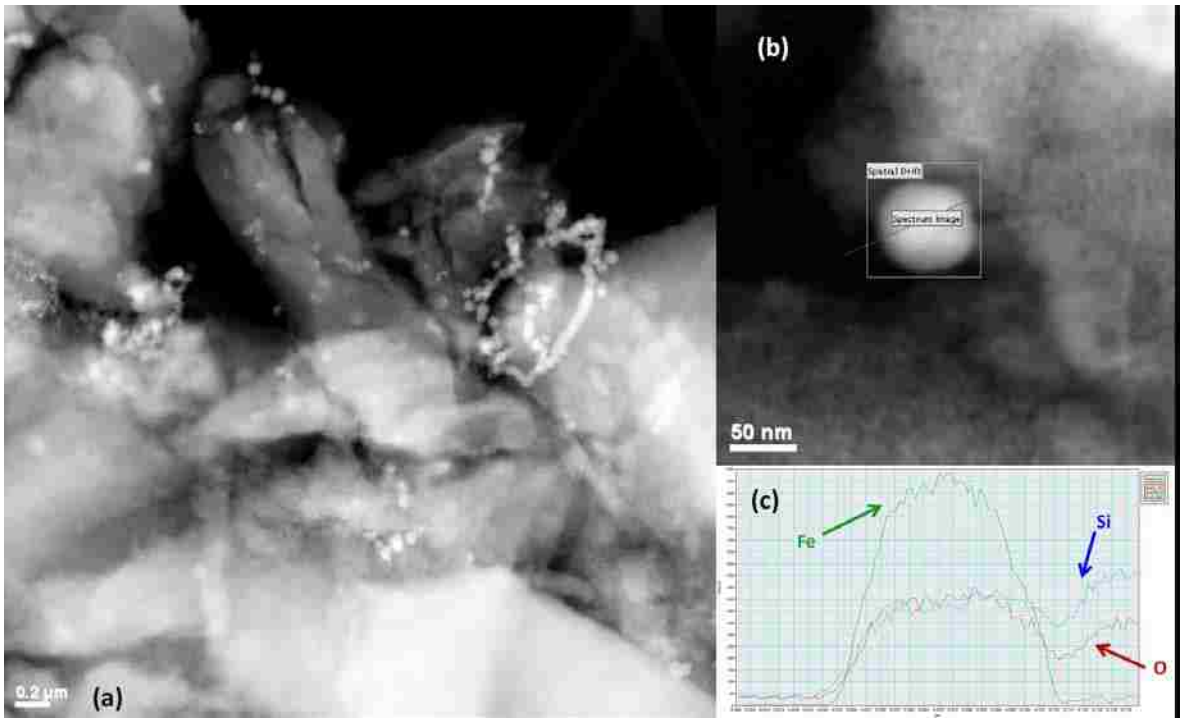

Figure 8.5 TEM of Fe NP on sulfonated silica gel.
(a) Fe particles (~50 nm) formed on surface and in the pores of silica gel. Brighter spots indicate Fe (higher atomic number). Scale bar is 200 nm. (b) Higher resolution image of spherical Fe nanoparticles with path indicating line scan for EDS. (c) EDS confirms elemental Fe composition of particle with silica background.

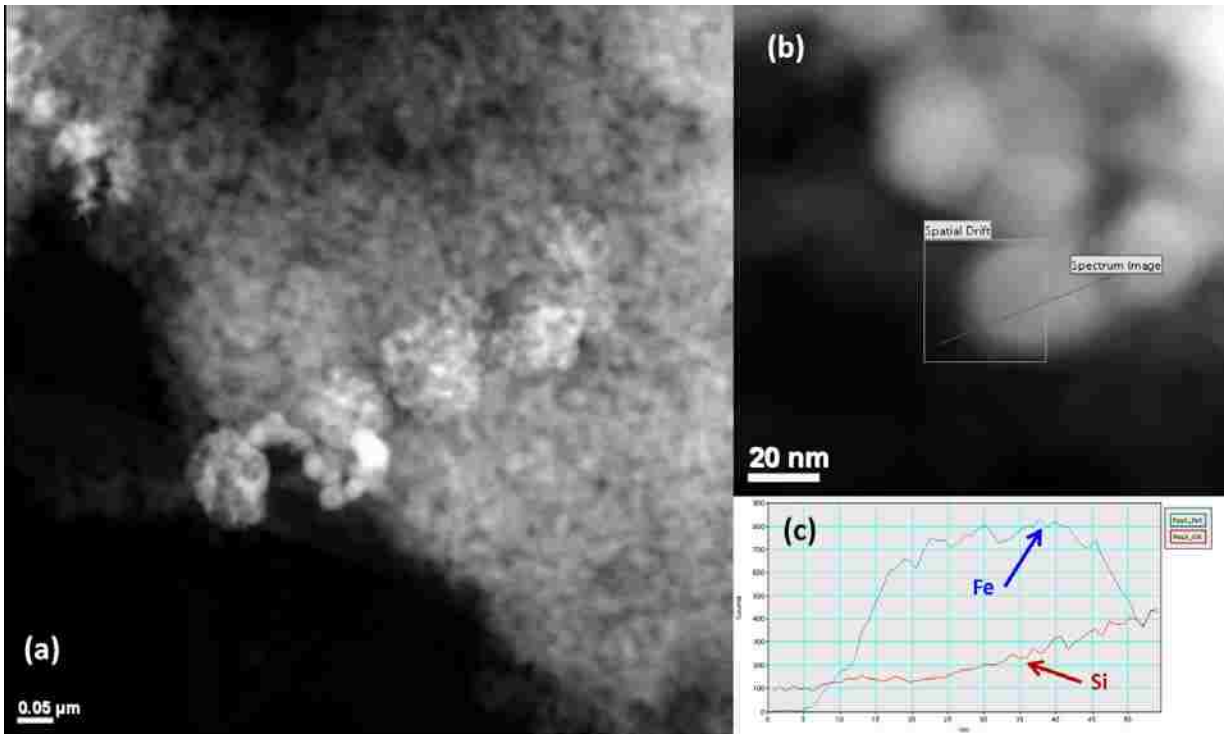

Figure 8.6 TEM of Fe NP on Ludox silica.
(a) Fe particles (30-50 nm) formed on surface of silica nanoparticles (22 nm). Brighter spots indicate Fe (higher atomic number). Scale bar is 50 nm. (b) Higher resolution image of spherical Fe nanoparticles with path indicating line scan for EDS. (c) EDS confirms elemental Fe composition of particle with silica background.

The iron nanoparticle alters the pore structure and surface characteristics of the functionalized material. Fe NP on Ludox (Figure 8.3b), both microporous and macroporous surface areas increase, corresponding to sorption of nitrogen in the interparticle spacing as well as on the surface of the NP. Overall, the surface area increase for Fe particles on Ludox is from 87 to 110 m^2/g. Using Equation (8.1), the expected increase in surface area for 30 nm Fe NP would be 25 m^2/g Fe, which is consistent with the experimentally determined increase (23 m^2/g). For the Fe NP on silica gel (Figure 8.3a), microporous surface area decreases, corresponding to pore blockage. The macroporous surface area increases, corresponding to sorption of nitrogen on surface of the NP. Overall, the BET surface area decreases from 264 to 224 m^2/g.

Silica-based Fe NP have been used as catalysts for well known Fischer-Tropsch hydrocarbon synthesis (particularly when using coal-derived syn gas[95]) and more recently as catalysts for carbon nanotube synthesis.[96] Catalytic advantages of silica-supported Fe NP are improved thermal stability, decreased deactivation, and improved selectivity.[93] The silica is thought to play a role in the reduction and drying process which preserves a high surface area. However, Fe NP on silica have been found to have lower activity than those on other supports or unsupported catalysts, due to the stronger interactions between silica and Fe NP including the formation of iron silicate interfacial species.[97] This effect increases with increasing silica:Fe ratio.[98] Fe NP on silica in these studies have been reported to be 5 to 20 nm.

8.6 Synthesis of Pd and Fe/Pd NP by ascorbic acid

The use of natural products as reducing agents (antioxidants) for the synthesis of metal NP has emerged as an important area of research. Not only are the natural products

completely “green” but they also can stabilize the particles against agglomeration and oxidation. Various natural products have been suggested, including the use of polyphenols,[99] commonly found in tea, coffee, wine, and fruit juices. Typically, the E^0 value of these compounds is sufficient to reduce ferrous or even ferric iron to zero-valent iron. Another natural product which has been used is ascorbic acid; however, the reduction potential of ascorbic acid to dehydroascorbic acid is not sufficient to reduce iron alone.[100] The use of ascorbic acid requires a secondary metal, such as Pd, which is reduced along with Fe to form Fe/Pd particles. Although other secondary metals have been described, Pd was chosen because Fe/Pd bimetallic nanoparticles have been shown effective in dechlorination of TCE. The reactions for the formation of Fe/Pd particles are shown in Table 8.2.

The use of natural reducing agents such as ascorbic acid can stabilize the nanoparticles against oxidation as well as inhibit particle growth. After synthesizing Pd nanoparticles, an IR spectrum of the particles was compared to spectra from the pure dehydroascorbic acid and ascorbic acid. The spectra (Figure 8.7) indicate that both the oxidation product (dehydroascorbic acid) and excess ascorbic acid (ascorbate at pH > 4.17) were adsorbed to the surface (structures are given in Figure 8.1b). The difference between the two compounds is seen by the peaks at 1753 cm^{-1} (C=O) and 1660 cm^{-1} (C=C). The shift of the C=C peak in the dehydroascorbic acid is caused by additional ring strain of three carbonyl moieties on a 5-membered ring. For the Fe/Pd particles, both peaks are seen indicating the presence of these adsorbed species.

Table 8.2 Reactions and standard reduction potentials for "green" synthesis of Fe/Pd bimetallic NP by ascorbic acid.
See Figure 1 for chemical structures

Reaction	E^0 value (V)
2 Ascorbic acid → 2 dehydroascorbic acid + 4 e^- + $4H^+$	-0.116
2/3 Fe^{3+} + $2e^-$ → 2/3 Fe^0	-0.0247
Pd^{2+} + $2e^-$ → Pd^0	+0.951

Overall:
2 Ascorbic acid + 2/3 Fe^{3+} + Pd^{2+} → 2 dehydroascorbic acid + 2/3 Fe^0 + $4H^+$ +0.810V

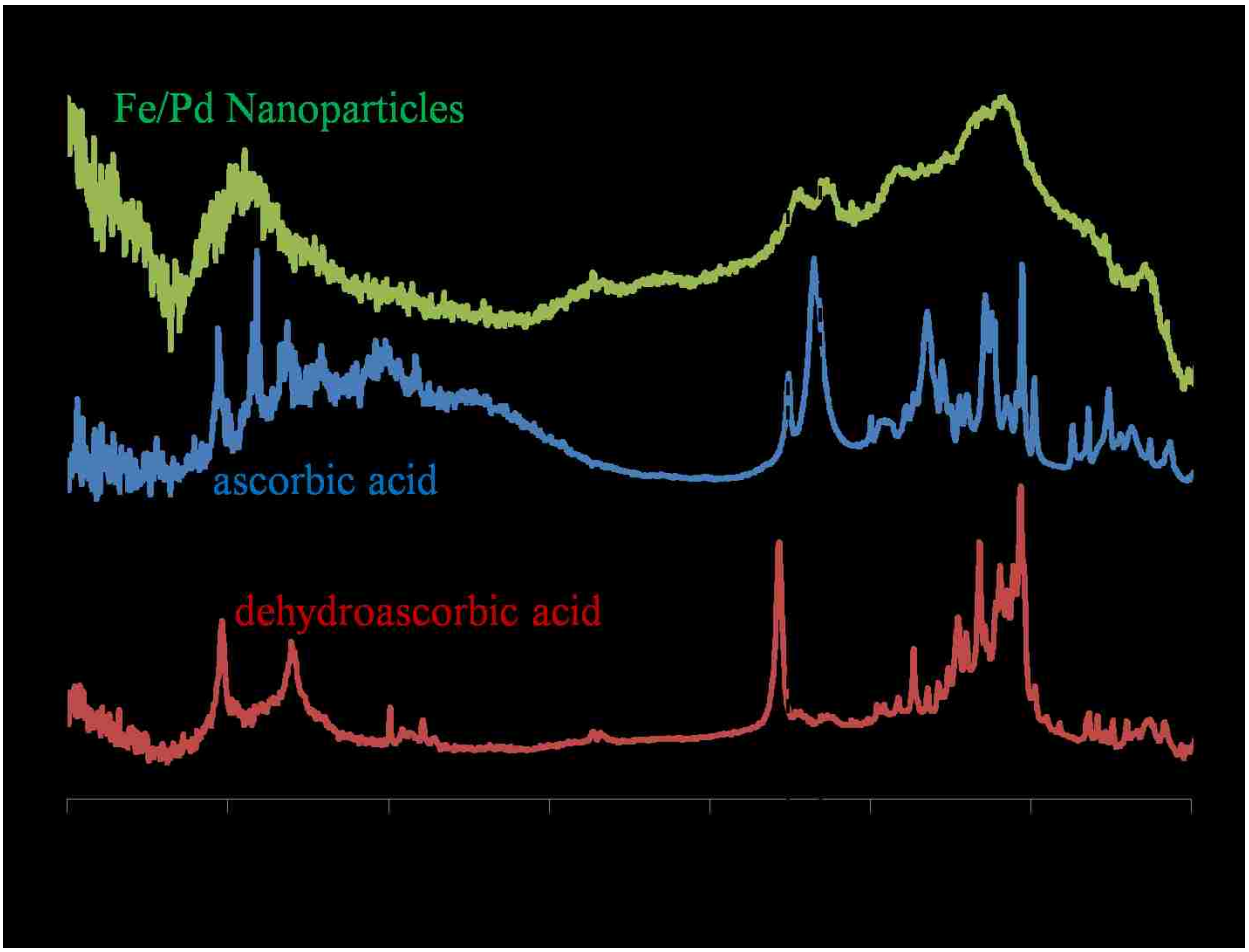

Figure 8.7 IR spectra of Fe/Pd NP with adsorbed surface species.
The nanoparticle spectrum indicates both ascorbate ion (C=C bond) and dehydroascorbic acid (C=O bond) adsorb to the nanoparticle surface. (Ascorbate ion is present above pH 4.7)

The particle size can be limited by use of excess ascorbic acid as indicated by Figure 8.8. The ascorbate can adsorb to the surface and impart a surface charge which inhibits agglomeration. As a higher ascorbic acid:Pd mole ratio was used, the measured hydrodynamic particle radius was significantly lowered, though ascorbic acid:Pd molar ratio >7 rendered no more decrease in size. For this reaction, the stoichiometric ratio is 2. Smaller Pd particles have been synthesized by other methods, such as the use of polyligand stabilizers and ascorbic acid reduction,[100] as well as the in vivo synthesis of bio-Pd.[101] However, this simple method yields stable, small Pd or Fe/Pd NP. Transmission electron micrograph of the ascorbic acid-synthesized particles at lower pH indicate the unusual growth of crystals with agglomerate diameter ~100 nm (Figure 8.9). Although the exact role of dehydroascorbic acid and ascorbate in directing the crystal growth is not known, other studies have indicated the synthesis of crystallites of various shapes using natural product reducing agents.[102]

Figure 8.8 Pd NP stabilized by excess ascorbic acid in synthesis.
Decrease in particle size (hydrodynamic radius measured by DLS) for Pd particles synthesized by reduction with ascorbic acid, due to presence of surface adsorption of excess ascorbate and dehydroascorbic acid. The synthesis reaction is same as presented in Figure 1, without the presence of Fe.

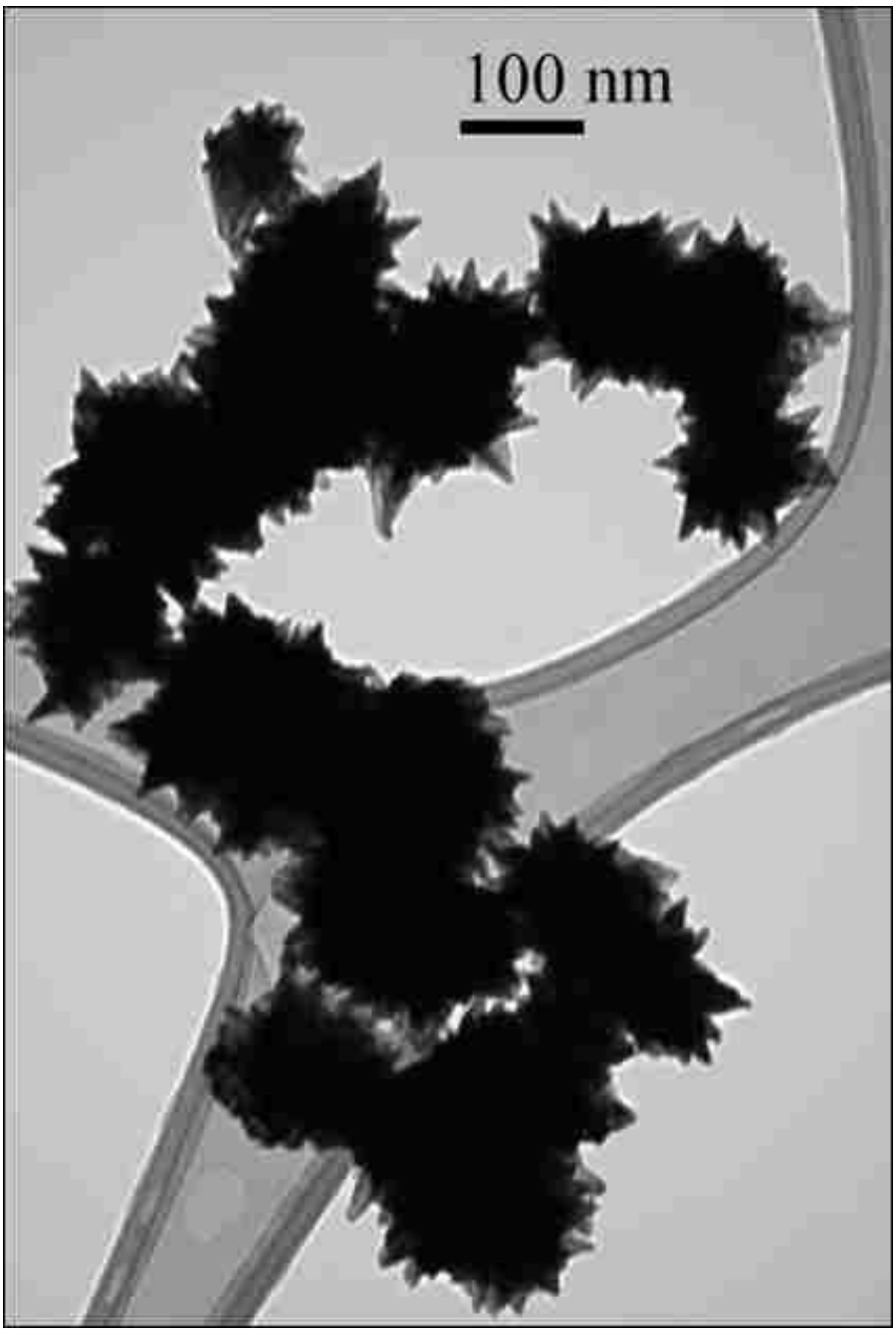

Figure 8.9 TEM of Fe/Pd NP synthesized by ascorbic acid at pH<4.2.

8.7 Oxidative Dechlorination

Recent results have shown success using silica-supported Fe NP for reductive dechlorination of TCE; however, heterogeneous oxidative dechlorination by Fe/Fe_2O_3 particles is an emerging area of research and holds great promise because of the naturally occurring oxidized iron in contaminated aquifers. Oxidative detoxification of TCE is accomplished using Fe/Fe_2O_3 particles as catalysts for the heterogeneous decomposition of H_2O_2, resulting in the formation of OH· (a strong oxidant with $E^0 = 2.73$ V). Iron oxide particles based on various platforms (membranes, polymers, and silica) have been also used for this reaction. To show the usefulness of this approach with our silica-based particles, we deliberately oxidized the Fe particles supported on Ludox and tested their efficiency. The primary species present is Fe_2O_3 which may surround a zero-valent Fe core.

The modified Haber-Weiss mechanism is commonly used to describe the decomposition of H_2O_2 on iron oxide surfaces.[103] Although many reactions are involved, the formation of OH· is driven by oxidation (8.7) of surface ferrous species (≡Fe(II)) and direct decomposition (8.8) of H_2O_2 by hydroperoxyl radicals (HO_2·). Overall, the decomposition of H_2O_2 is modeled as a heterogeneous pseudo-first order reaction (8.9).

$$\equiv Fe(II) + H_2O_2 \rightarrow \equiv Fe(III) + OH^- + OH\cdot \quad (8.7)$$

$$H_2O_2 + HO_2\cdot \rightarrow H_2O + O_2 + OH\cdot \quad (8.8)$$

$$-\frac{dC_{H_2O_2}}{dt} = k_{SA} A_s \rho_m C_{H_2O_2} \quad (8.9)$$

In the case of our reactions, the Fe loading (0.16 Fe/L) was lower compared to other studies, which slowed the reaction, with initial H_2O_2 concentration of 41.4 mM (1409 mg/L).

The TCE is then oxidized by the generated OH·, which is given as a second order reaction.

$$-\frac{dC_{TCE}}{dt} = kC_{TCE}C_{OH\cdot} \quad (8.10)$$

Previous studies have found $C_{OH\cdot}$ is small and constant,[104] so that in many cases the oxidation of TCE can be given as pseudo-first order. Pseudo-first-order kinetics have been seen for the Fe-catalyzed oxidation of quinoline[105] (using Fe-containing aquifer material) and trichlorobenzene[106] (using hematite, Fe_2O_3) under reaction conditions similar to this study. However, others have found this Fe-catalyzed oxidation to be pseudo-zeroth order. In this case the decomposition of H_2O_2 was not measured, only the oxidation of TCE. Figure 10 shows the 50% dechlorination in 50 hours of using these particles. However, the further result depends on Fe loading and H_2O_2 concentration, as well as Fe:H_2O_2 ratio. The TCE oxidation kinetics fit a first-order reaction with R^2= 0.95 up to 20 h, as shown in Figure 8.10. The usefulness of Fe/Fe_2O_3-catalyzed production of OH· for oxidative dechlorination is demonstrated. Chloride measurements indicated that after the reaction had ceased (50 hrs), the recovery of Cl^- was 91% of the theoretical Cl^- production, based on 3 mol chloride:1 mole TCE degraded.

The role of silica in the oxidative dechlorination of TCE is not well understood. Recent reports have speculated that the silica alters the rate of H_2O_2 decomposition because the lower point of zero charge renders the silica-Fe/Fe_2O_3 negatively charged at

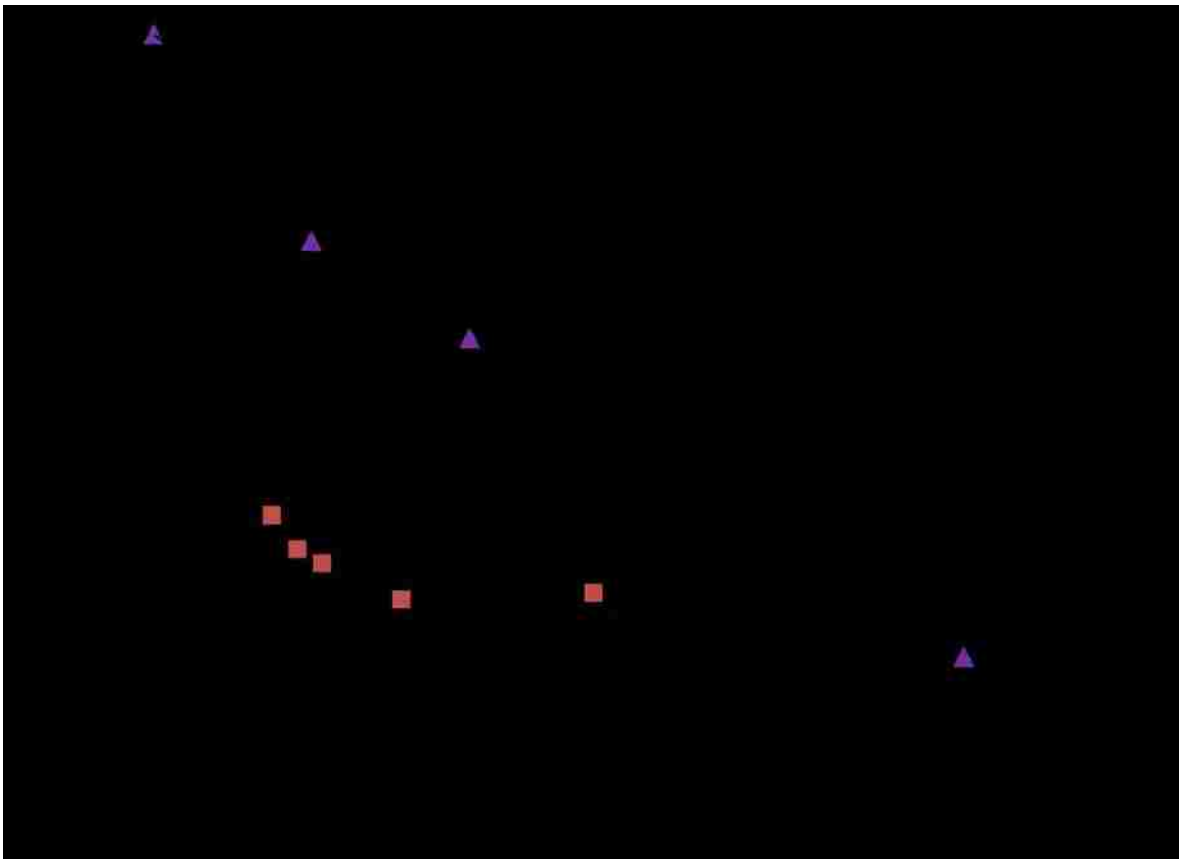

Figure 8.10 Oxidative degradation of TCE by supported iron-iron oxide particles. Particles are air-oxidized Fe/Fe_2O_3 on Ludox, and degradation occurs by hydroxyl radical reaction (use of H_2O_2). $C_{TCE,0}$ = 21.5 mg/L.

near neutral pH.[107] Altered rates of decomposition were found to be dependent upon sand species present when using real sand-based Fe oxide catalysts,[105] though efforts to model the complete process were incomplete. It may also be that the surface of the sulfonated silica (Lewis base) impedes the conversion of Fe^{2+} to Fe^{3+}, which is postulated[75] to be the rate-limiting step of the catalytic cycle for H_2O_2 decomposition. However, more study in this area is needed, as recent reports suggest faster and complete decomposition using silica-based iron oxide catalysts, and also incomplete oxidation using soil-based Fe catalysts.

The silica-based iron particles may also be used for reductive degradation of TCE. Recent work[71] shows that unfunctionalized silica containing iron nanoparticles dechlorinated TCE. In the case of partially hydrophobized silica, there was an immediate decrease in the bulk concentration of TCE due to absorption (partitioning of TCE to the hydrophobized surface) followed by quantitative conversion to product after 96 hours reaction. This study also reports the same immediate decrease in bulk TCE concentration, but without destruction, when hydrophobized silica is used without iron.

8.8 Reductive Dechlorination

The overall reductive dechlorination is modeled as a pseudo-first order heterogeneous reaction, and the reaction constant determined by (8.11) and results are shown in Figure 7.11.

$$-\frac{dC_{TCE}}{dt} = k_{obs}C_{TCE} = k_{SA}A_s\rho_m C_{TCE} \quad (8.11)$$

where A_s is specific surface area and ρ_m is the loading of particles. In the case of very small particles (such as those ascorbic acid synthesized particles at near-neutral pH), the specific surface area (A_s) is calculated as surface-to-volume ratio (8.1) divided

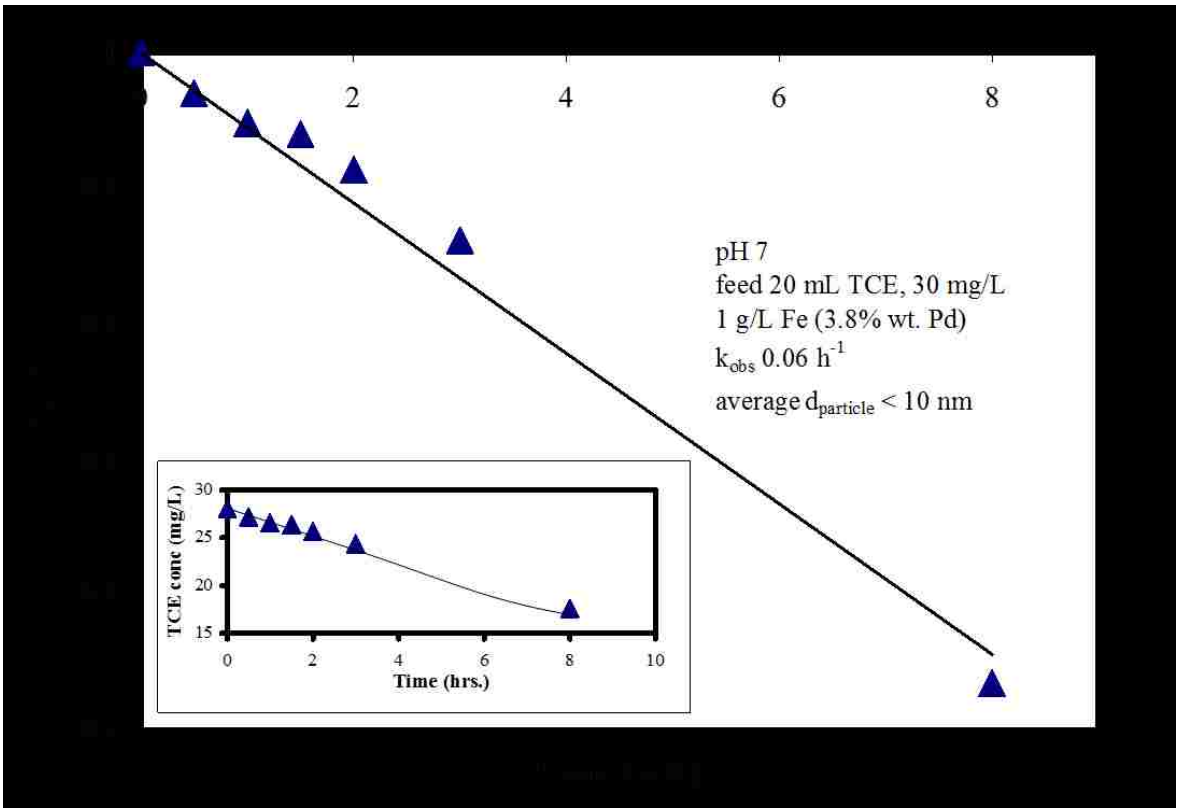

Figure 8.11 Reductive degradation of trichloroethylene by Fe/Pd NP.
Particles synthesized by reduction with ascorbic acid. $C_{TCE,0}$ = 27 mg/L

by the intrinsic density of the material (ρ_{Fe} = 7.9 g/cm^3 and ρ_{Pd} = 12.0 g/cm^3). Based on weighted average of Fe/Pd composition (3.8 wt% Pd), the density (ρ) of the Fe/Pd NP is 8.1 g/cm^3. A_s for the ascorbic acid-synthesized Fe/Pd NP (r = 5 nm) are 74.1 m^2/g. Under the reaction conditions described in Figure 11, the k_{SA} is calculated to be 8.1 x10^{-4} L/m^{2}h. A recent study using Fe/Pd bimetallic particles (stabilized with carboxymethylcellulose) indicated k_{SA} of 64 x10^{-4} L/m^{2}h for particles with diameter of 4.3 nm.[79] Although the reaction rate is lower than some reported values, these small stable particles may be more useful for reductive dechlorination in dilute TCE-contaminated groundwater plumes, where stability and dispersion of particles is an important consideration.

8.9 Conclusions

The stabilization of Fe and Fe/Pd bimetallic NP through use of covalently functionalized sulfonated silica platforms was demonstrated, as well as the use of non-toxic, natural product ascorbic acid as a reducing agent. The silica has a number of advantages including the dispersion of particles to prevent agglomeration and the versatility of surface functionalization. NP were effectively synthesized either in the pore mouths or on the surface of silica with different morphologies (colloidal and porous silica gel). The synthesis of stable Fe/Pd NP was also achieved through the use of ascorbic acid as a reducing agent, where the ascorbate and dehydroascorbic acid inhibit agglomeration and the excess ascorbic acid protects the surface from oxidation. Both strategies yielded nanoparticles which were reactive toward the detoxificiation of trichloroethylene (TCE), a widespread persistent and toxic water pollutant. TCE detoxification can occur through reduction with Fe NP. However, it was also

demonstrated that the Fe NP is intentionally oxidized to form iron/iron oxide particles, which are used for the oxidative detoxification of TCE through the heterogeneous decomposition of hydrogen peroxide.

9. Chapter Nine: Conclusions and Scientific Advancements

The research work has led to the development of advanced functionalized materials for toxic metal and organic remediation. The successful synthesis of functionalized silica and mixed matrix membranes for environmental applications has been achieved. These applications include the sorption of mercury (both elemental and aqueous) and the use of silica as a support for metal nanoparticles with significant environmental applications.

The key scientific advancements of these studies:

- quantification of silica functionalization with sulfur-containing silanes
- functionalization of a silica-coated carbon material for aqueous mercury sorption and development of mixed matrix membranes for this application
- development of regenerable sorbents for aqueous mercury removal
- synthesis of high-capacity chemisorptive materials for elemental mercury vapor sorption with key advantages over conventional materials
- development of functionalized silica platforms for nanoparticle synthesis, and the demonstration of stabilized nanoparticles towards TCE degradation

References

1. Vansant, E. F.; Voort, P. V. D.; Vracken, K. C., *Characterization and Chemical Modification of the Silica Surface*. 1 ed.; Elsevier: New York, 1995.
2. (a) Harris, M. T.; Brunson, R. R.; Byers, C. H., The Base-Catalyzed-Hydrolysis and Condensation-Reactions of Dilute and Concentrated Teos Solutions. *Journal of Non-Crystalline Solids* **1990,** *121* (1-3), 397-403; (b) Ng, L. V.; McCormick, A. V., Acidic sol-gel polymerization of TEOS: Effect of solution composition on cyclization and bimolecular condensation rates. *Journal of Physical Chemistry* **1996,** *100* (30), 12517-12531.
3. Everett, D. H., Manual of Symbols and Terminology for Physicochemical Quantities and Units, Appendix II: Definitions, Terminology and Symbols in Colloid and Surface Chemistry. *Pure and Applied Chemistry* **1972,** *31* (4), 578-638.
4. Lowell, S.; Shields, J. E.; Thomas, M. A.; Thommes, M., *Characterization of Porous Solids and Powders: Surface Area, Pore Size, and Density*. Kluwer Academic Publishers: Boston, 2004.
5. Barrett, E. P.; Joyner, L. G.; Halenda, P. P., The Determination of Pore Volume and Area Distributions in Porous Substances .1. Computations from Nitrogen Isotherms. *Journal of the American Chemical Society* **1951,** *73* (1), 373-380.
6. Brunauer, S.; Emmett, P. H.; Teller, E., Adsorption of gases in multimolecular layers. *Journal of the American Chemical Society* **1938,** *60*, 309-319.
7. Jelinek, L.; Kovats, E. S., True Surface-Areas from Nitrogen Adsorption Experiments. *Langmuir* **1994,** *10* (11), 4225-4231.
8. Wei, C.; Mccown, M., Effect of Alkyl Chain-Length on Surface Silanization of Silica. *J Chromatogr* **1985,** *318* (2), 173-185.
9. Boccuzzi, F.; Coluccia, S.; Ghiotti, G.; Morterra, C.; Zecchina, A., Infrared study of surface modes on silica. *Journal of Physical Chemistry* **1978,** *82* (11), 1298-1303.
10. Yoshinaga, K.; Yoshida, H.; Yamamoto, Y.; Takakura, K.; Komatsu, M., A Convenient Determination of Surface Hydroxyl Group on Silica-Gel by Conversion of Silanol Hydrogen to Dimethylsilyl Group with Diffuse Reflectance Ftir Spectroscopy. *Journal of Colloid and Interface Science* **1992,** *153* (1), 207-211.
11. (a) Ashtekar, S.; Hastings, J. J.; Barrie, P. J.; Gladden, L. F., Quantification of the number of silanol groups in silicalite and mesoporous MCM-41: Use of FT-Raman spectroscopy. *Spectroscopy Letters* **2000,** *33* (4), 569-584; (b) Ramirez, A.; Lopez, B. L.; Sierra, L., Study of the acidic sites and their modifications in mesoporous silica synthesized in acidic medium under quiescent conditions. *Journal of Physical Chemistry B* **2003,** *107* (35), 9275-9280.
12. Zhuravlev, L. T., Surface Characterization of Amorphous Silica - a Review of Work from the Former Ussr. *Colloids and Surfaces a-Physicochemical and Engineering Aspects* **1993,** *74* (1), 71-90.
13. Iler, R. K., *The Chemistry of Silica*. Wiley: New York, 1979.
14. Walcarius, A.; Delacote, C., Mercury(II) binding to thiol-functionalized mesoporous silicas: critical effect of pH and sorbent properties on capacity and selectivity. *Anal Chim Acta* **2005,** *547* (1), 3-13.

15. Park, D. H.; Nishiyama, N.; Egashira, Y.; Ueyama, K., Enhancement of hydrothermal stability and hydrophobicity of a silica MCM-48 membrane by silylation. *Industrial & Engineering Chemistry Research* **2001,** *40,* 6105-6110.
16. Ma, Y. R.; Qi, L. M.; Ma, J. M.; Wu, Y. Q.; Liu, O.; Cheng, H. M., Large-pore mesoporous silica spheres: synthesis and application in HPLC. *Colloids and Surfaces a-Physicochemical and Engineering Aspects* **2003,** *229* (1-3), 1-8.
17. Galli, B.; Gasparrini, F.; Misiti, D.; Natile, G.; Palmieri, G., Thin-Layer Chromatography of Metal-Complexes on Glycidoxypropyl Functionalized Silica Plates. *J Chromatogr* **1987,** *409,* 377-382.
18. Revillon, A.; Leroux, D., Functional silica supported polymer .5. 'Onto' versus 'from' grafting processes. *Reactive & Functional Polymers* **1995,** *26* (1-3), 105-118.
19. Iiskola, E. I.; Timonen, S.; Pakkanen, T. T.; Harkki, O.; Seppala, J. V., Functional surface groups for single-site heterogeneous alpha-olefin polymerization catalysts. *Applied Surface Science* **1997,** *121,* 372-377.
20. Mal, N. K.; Fujiwara, M.; Tanaka, Y., Photocontrolled reversible release of guest molecules from coumarin-modified mesoporous silica. *Nature* **2003,** *421* (6921), 350-353.
21. Hoffmann, F.; Cornelius, M.; Morell, J.; Froba, M., Silica-based mesoporous organic-inorganic hybrid materials. *Angew Chem Int Edit* **2006,** *45* (20), 3216-3251.
22. Liu, Y. H.; Lin, H. P.; Mou, C. Y., Direct method for surface silyl functionalization of mesoporous silica. *Langmuir* **2004,** *20* (8), 3231-3239.
23. Deng, G.; Markowitz, M. A.; Kust, P. R.; Gaber, B. P., Control of surface expression of functional groups on silica particles. *Mat Sci Eng C-Bio S* **2000,** *11* (2), 165-172.
24. Impens, N. R. E. N.; van der Voort, P.; Vansant, E. F., Silylation of micro-, meso- and non-porous oxides: a review. *Microporous and Mesoporous Materials* **1999,** *28* (2), 217-232.
25. Sutra, P.; Fajula, F.; Brunel, D.; Lentz, P.; Daelen, G.; Nagy, J. B., Si-29 and C-13 MAS-NMR characterization of surface modification of micelle-templated silicas during the grafting of organic moieties and end-capping. *Colloids and Surfaces a-Physicochemical and Engineering Aspects* **1999,** *158* (1-2), 21-27.
26. Kim, S.; Gavalas, G. R., Kinetic-Study of the Reactions of Chlorosilanes with Porous Vycor Glass. *Journal of Colloid and Interface Science* **1993,** *161* (1), 6-18.
27. Rubinsztajn, S.; Cypryk, M.; Chojnowski, J., Condensation of Model Linear Siloxane Oligomers Possessing Silanol and Silyl Chloride End Groups - the Mechanism of Silanol Silylation by a Chlorosilane in the Presence of Neutral Nucleophiles. *J Organomet Chem* **1989,** *367* (1-2), 27-37.
28. Lazghab, M.; Saleh, K.; Guigon, P., A new solventless process to hydrophobize silica powders in fluidized beds. *Aiche Journal* **2008,** *54* (4), 897-908.
29. Bogart, G. R.; Leyden, D. E., Investigation of Amine-Catalyzed Gas-Phase Adsorption Silylation Reactions with Alkoxysilanes. *Journal of Colloid and Interface Science* **1994,** *167* (1), 27-34.
30. Sigel, A.; Sigel, H., *Mercury and Its Effects on Environment and Biology*. Marcel Dekker, Inc: New York, 1997; Vol. 34, p 604.

31. (a) Gkika, E.; Troupis, A.; Hiskia, A.; Papaconstantinou, E., Photocatalytic reduction and recovery of mercury by polyoxometalates. *Environ Sci Technol* **2005,** *39* (11), 4242-4248; (b) Lopez-Munoz, M. J.; Aguado, J.; Arencibia, A.; Pascual, R., Mercury removal from aqueous solutions of HgCl(2) by heterogeneous photocatalysis with TiO(2). *Appl Catal B-Environ* **2011,** *104* (3-4), 220-228.
32. (a) Meagher, R. B., Phytoremediation of toxic elemental and organic pollutants. *Curr Opin Plant Biol* **2000,** *3* (2), 153-162; (b) Raskin, I.; Smith, R. D.; Salt, D. E., Phytoremediation of metals: Using plants to remove pollutants from the environment. *Curr Opin Biotech* **1997,** *8* (2), 221-226; (c) McGrath, S. P.; Zhao, F. J.; Lombi, E., Phytoremediation of metals, metalloids, and radionuclides. *Adv Agron* **2002,** *75*, 1-56; (d) Hussein, S.; Ruiz, O. N.; Terry, N.; Daniell, H., Phytoremediation of mercury and organomercurials in chloroplast transgenic plants: Enhanced root uptake, translocation to shoots, and volatilization. *Environ Sci Technol* **2007,** *41* (24), 8439-8446.
33. (a) Lovley, D. R.; Coates, J. D., Bioremediation of metal contamination. *Curr Opin Biotech* **1997,** *8* (3), 285-289; (b) Barkay, T.; Schaefer, J., Metal and radionuclide bioremediation: issues, considerations and potentials. *Curr Opin Microbiol* **2001,** *4* (3), 318-323; (c) Wagner-Dobler, I., Pilot plant for bioremediation of mercury-containing industrial wastewater. *Appl Microbiol Biot* **2003,** *62* (2-3), 124-133.
34. (a) Kiyono, M.; Pan-Hou, H., Genetic engineering of bacteria for environmental remediation of mercury. *J Health Sci* **2006,** *52* (3), 199-204; (b) Chen, S. L.; Kim, E. K.; Shuler, M. L.; Wilson, D. B., Hg2+ removal by genetically engineered Escherichia coli in a hollow fiber bioreactor. *Biotechnol Progr* **1998,** *14* (5), 667-671.
35. (a) Matlock, M. M.; Howerton, B. S.; Atwood, D. A., Irreversible precipitation of mercury and lead. *J Hazard Mater* **2001,** *84* (1), 73-82; (b) Matlock, M. M.; Howerton, B. S.; Henke, K. R.; Atwood, D. A., A pyridine-thiol ligand with multiple bonding sites for heavy metal precipitation. *J Hazard Mater* **2001,** *82* (1), 55-63; (c) Wasay, S. A.; Arnfalk, P.; Tokunaga, S., Remediation of a Soil Polluted by Mercury with Acidic Potassium-Iodide. *J Hazard Mater* **1995,** *44* (1), 93-102.
36. Blue, L. Y.; Van Aelstyn, M. A.; Matlock, M.; Atwood, D. A., Low-level mercury removal from groundwater using a synthetic chelating ligand. *Water Res* **2008,** *42* (8-9), 2025-2028.
37. (a) Atwood, D. A., *Recent Developments in Mercury Science*. Springer-Verlag: 2006; Vol. 120; (b) Wang, Q. R.; Kim, D.; Dionysiou, D. D.; Sorial, G. A.; Timberlake, D., Sources and remediation for mercury contamination in aquatic systems - a literature review. *Environ Pollut* **2004,** *131* (2), 323-336; (c) Babel, S.; Kurniawan, T. A., Low-cost adsorbents for heavy metals uptake from contaminated water: a review. *J Hazard Mater* **2003,** *97* (1-3), 219-243.
38. Hollerman, W.; Holland, L.; Ila, D.; Hensley, J.; Southworth, G.; Klasson, T.; Taylor, P.; Johnston, J.; Turner, R., Results from the low level mercury sorbent test at the Oak Ridge Y-12 Plant in Tennessee. *J Hazard Mater* **1999,** *68* (3), 193-203.
39. Nakayama, M.; Chikuma, M.; Tanaka, H.; Tanaka, T., A Chelate-Forming Resin Bearing Mercapto and Azo Groups and Its Application to the Recovery of Mercury(Ii). *Talanta* **1982,** *29* (6), 503-506.

40. Feng, X.; Fryxell, G. E.; Wang, L. Q.; Kim, A. Y.; Liu, J.; Kemner, K. M., Functionalized monolayers on ordered mesoporous supports. *Science* **1997,** *276* (5314), 923-926.
41. Sugii, A.; Ogawa, N.; Hagiwara, Y., Synthesis and Properties of a Chelating Resin Containing Triazolethiol Groups. *Talanta* **1984,** *31* (12), 1079-1082.
42. Smuleac, V.; Butterfield, D. A.; Sikdar, S. K.; Varma, R. S.; Bhattacharyya, D., Polythiol-functionalized alumina membranes for mercury capture. *J Membrane Sci* **2005,** *251* (1-2), 169-178.
43. Ahn, J. Y.; Chung, W. J.; Pinnau, I.; Guiver, M. D., Poly sulfone/silica nanoparticle mixed-matrix membranes for gas separation. *J Membrane Sci* **2008,** *314* (1-2), 123-133.
44. (a) Mahajan, R.; Koros, W. J., Factors controlling successful formation of mixed-matrix gas separation materials. *Industrial & Engineering Chemistry Research* **2000,** *39* (8), 2692-2696; (b) Chung, T. S.; Jiang, L. Y.; Li, Y.; Kulprathipanja, S., Mixed matrix membranes (MMMs) comprising organic polymers with dispersed inorganic fillers for gas separation. *Prog Polym Sci* **2007,** *32* (4), 483-507.
45. Ladhe, A. R.; Frailie, P.; Hua, D.; Darsillo, M.; Bhattacharyya, D., Thiol-functionalized silica-mixed matrix membranes for silver capture from aqueous solutions: Experimental results and modeling. *J Membrane Sci* **2009,** *326* (2), 460-471.
46. Srivastava, R. K.; Hutson, N. D.; Martin, B.; Princiotta, F.; Staudt, J., Control of mercury emissions from coal-fired electric utility boilers. *Environmental Science & Technology* **2006**.
47. Lee, J. Y.; Ju, Y. H.; Keener, T. C.; Varma, R. S., Development of cost-effective noncarbon sorbents for Hg-0 removal from coal-fired power plants. *Environmental Science & Technology* **2006,** *40* (8), 2714-2720.
48. Hall, B.; Schager, P.; Weesmaa, J., The Homogeneous Gas-Phase Reaction of Mercury with Oxygen, and the Corresponding Heterogeneous Reactions in the Presence of Activated Carbon and Fly-Ash. *Chemosphere* **1995,** *30* (4), 611-627.
49. Lu, A. H.; Salabas, E. L.; Schuth, F., Magnetic nanoparticles: Synthesis, protection, functionalization, and application. *Angew Chem Int Edit* **2007,** *46* (8), 1222-1244.
50. Huber, D. L., Synthesis, properties, and applications of iron nanoparticles. *Small* **2005,** *1* (5), 482-501.
51. Tratnyek, P. G.; Nurmi, J. T.; Sarathy, V.; Baer, D. R.; Amonette, J. E.; Pecher, K.; Wang, C. M.; Linehan, J. C.; Matson, D. W.; Penn, R. L.; Driessen, M. D., Characterization and properties of metallic iron nanoparticles: Spectroscopy, electrochemistry, and kinetics. *Environ Sci Technol* **2005,** *39* (5), 1221-1230.
52. Wang, C. B.; Zhang, W. X., Synthesizing nanoscale iron particles for rapid and complete dechlorination of TCE and PCBs. *Environ Sci Technol* **1997,** *31* (7), 2154-2156.
53. Nadagouda, M. N.; Varma, R. S., A greener synthesis of core (Fe, Cu)-shell (An, Pt, Pd, and Ag) nanocrystals using aqueous vitamin C. *Cryst Growth Des* **2007,** *7* (12), 2582-2587.

54. Smuleac, V.; Varma, R.; Sikdar, S.; Bhattacharyya, D., Green synthesis of Fe and Fe/Pd bimetallic nanoparticles in membranes for reductive degradation of chlorinated organics. *J Membrane Sci* **2011,** *379* (1-2), 131-137.
55. Virkutyte, J.; Varma, R. S., Green synthesis of metal nanoparticles: Biodegradable polymers and enzymes in stabilization and surface functionalization. *Chem Sci* **2011,** *2* (5), 837-846.
56. Zhao, D. Y.; He, F.; Liu, J. C.; Roberts, C. B., Stabilization of Fe-Pd nanoparticles with sodium carboxymethyl cellulose for enhanced transport and dechlorination of trichloroethylene in soil and groundwater. *Ind Eng Chem Res* **2007,** *46* (1), 29-34.
57. Liu, J. C.; He, F.; Durham, E.; Zhao, D. Y.; Roberts, C. B., Polysugar-stabilized Pd nanoparticles exhibiting high catalytic activities for hydrodechlorination of environmentally deleterious trichloroethylene. *Langmuir* **2008,** *24* (1), 328-336.
58. Lowry, G. V.; Phenrat, T.; Saleh, N.; Sirk, K.; Kim, H. J.; Tilton, R. D., Stabilization of aqueous nanoscale zerovalent iron dispersions by anionic polyelectrolytes: adsorbed anionic polyelectrolyte layer properties and their effect on aggregation and sedimentation. *Journal of Nanoparticle Research* **2008,** *10* (5), 795-814.
59. Tilton, R. D.; Sirk, K. M.; Saleh, N. B.; Phenrat, T.; Kim, H. J.; Dufour, B.; Ok, J.; Golas, P. L.; Matyjaszewski, K.; Lowry, G. V., Effect of Adsorbed Polyelectrolytes on Nanoscale Zero Valent Iron Particle Attachment to Soil Surface Models. *Environ Sci Technol* **2009,** *43* (10), 3803-3808.
60. Muller, R. N.; Laurent, S.; Forge, D.; Port, M.; Roch, A.; Robic, C.; Elst, L. V., Magnetic iron oxide nanoparticles: Synthesis, stabilization, vectorization, physicochemical characterizations, and biological applications. *Chemical Reviews* **2008,** *108* (6), 2064-2110.
61. Mirkhalaf, F.; Paprotny, J.; Schiffrin, D. J., Synthesis of metal nanoparticles stabilized by metal-carbon bonds. *J Am Chem Soc* **2006,** *128* (23), 7400-7401.
62. Li, D.; Kaner, R. B., Shape and aggregation control of nanoparticles: Not shaken, not stirred. *J Am Chem Soc* **2006,** *128* (3), 968-975.
63. Bhattacharyya, D.; Xu, J., Modeling of Fe/Pd nanoparticle-based functionalized membrane reactor for PCB dechlorination at room temperature. *J Phys Chem C* **2008,** *112* (25), 9133-9144.
64. Choi, H.; Al-Abed, S. R.; Agarwal, S.; Dionysiou, D. D., Synthesis of reactive nano-Fe/Pd bimetallic system-impregnated activated carbon for the simultaneous adsorption and dechlorination of PCBs. *Chem Mater* **2008,** *20* (11), 3649-3655.
65. Sunkara, B.; Zhan, J. J.; He, J. B.; McPherson, G. L.; Piringer, G.; John, V. T., Nanoscale Zerovalent Iron Supported on Uniform Carbon Microspheres for the In situ Remediation of Chlorinated Hydrocarbons. *Acs Appl Mater Inter* **2010,** *2* (10), 2854-2862.
66. Benoit, R.; Warmont, F.; Meynen, V.; De Witte, K.; Cool, P.; Treguer-Delapierre, M.; Saboungi, M. L., Optimisation of the surface properties of SBA-15 mesoporous silica for in-situ nanoparticle synthesis. *Microporous and Mesoporous Materials* **2009,** *120* (1-2), 2-6.

67. Lim, W. T. L.; Zhong, Z.; Borgna, A., An effective sonication-assisted reduction approach to synthesize highly dispersed Co nanoparticles on SiO_2. *Chemical Physics Letters* **2009,** *471*, 122-127.
68. Seger, B.; Kongkanand, A.; Vinodgopal, K.; Kamat, P. V., Platinum dispersed on silica nanoparticle as electrocatalyst for PEM fuel cell. *Journal of Electroanalytical Chemistry* **2008,** *621* (2), 198-204.
69. Wallace, J. M.; Stroud, R. M.; Pietron, J. J.; Long, J. W.; Rolison, D. R., The effect of particle size and protein content on nanoparticle-gold-nucleated cytochrome c superstructures encapsulated in silica nanoarchitectures. *Journal of Non-Crystalline Solids* **2004,** *350*, 31-38.
70. Zhang, S. B.; Wang, J. K.; Liu, H. T.; Wang, X. L., One-pot synthesis of Ni-nanoparticle-embedded mesoporous titania/silica catalyst and its application for CO(2)-reforming of methane. *Catal Commun* **2008,** *9* (6), 995-1000.
71. Zheng, T. H.; Zhan, J. J.; He, J. B.; Day, C.; Lu, Y. F.; Mcpherson, G. L.; Piringer, G.; John, V. T., Reactivity characteristics of nanoscale zerovalent iron-silica composites for trichloroethylene remediation. *Environmental Science & Technology* **2008,** *42* (12), 4494-4499.
72. Zhan, J. J.; Zheng, T. H.; Piringer, G.; Day, C.; McPherson, G. L.; Lu, Y. F.; Papadopoulos, K.; John, V. T., Transport Characteristics of Nanoscale Functional Zerovalent Iron/Silica Composites for in Situ Remediation of Trichloroethylene. *Environmental Science & Technology* **2008,** *42* (23), 8871-8876.
73. Miyake, Y.; Sakoda, A.; Yamanashi, H.; Kaneda, H.; Suzuki, M., Activated carbon adsorption of trichloroethylene (TCE) vapor stripped from TCE-contaminated water. *Water Res* **2003,** *37* (8), 1852-1858.
74. De Laat, J.; Gallard, H., Catalytic decomposition of hydrogen peroxide by Fe(III) in homogeneous aqueous solution: Mechanism and kinetic modeling. *Environ Sci Technol* **1999,** *33* (16), 2726-2732.
75. Lewis, S.; Lynch, A.; Bachas, L.; Hampson, S.; Ormsbee, L.; Bhattacharyya, D., Chelate-Modified Fenton Reaction for the Degradation of Trichloroethylene in Aqueous and Two-Phase Systems. *Environ Eng Sci* **2009,** *26* (4), 849-859.
76. Xu, J.; Bhattacharyya, D., Membrane-based bimetallic nanoparticles for environmental remediation: Synthesis and reactive properties. *Environmental Progress* **2005,** *24* (4), 358-366.
77. Jin, S.; Fallgren, P. H.; Morris, J. M.; Edgar, E. S., Degradation of trichloroethene in water by electron supplementation. *Chem Eng J* **2008,** *140* (1-3), 642-645.
78. Tee, Y. H.; Grulke, E.; Bhattacharyya, D., Role of Ni/Fe nanoparticle composition on the degradation of trichloroethylene from water. *Ind Eng Chem Res* **2005,** *44* (18), 7062-7070.
79. Zhao, D. Y.; He, F., Hydrodechlorination of trichloroethene using stabilized Fe-Pd nanoparticles: Reaction mechanism and effects of stabilizers, catalysts and reaction conditions. *Applied Catalysis B-Environmental* **2008,** *84* (3-4), 533-540.
80. Liu, H. L.; Wang, X. Y.; Chen, C.; Ma, J., Characterization and Evaluation of Catalytic Dechlorination Activity of Pd/Fe Bimetallic Nanoparticles. *Ind Eng Chem Res* **2008,** *47* (22), 8645-8651.

81. Meeks, N. D.; Rankin, S.; Bhattacharyya, D., Sulfur-Functionalization of Porous Silica Particles and Application to Mercury Vapor Sorption. *Ind Eng Chem Res* **2010,** *49* (10), 4687-4693.
82. Sing, K. S. W.; Everett, D. H.; Haul, R. A. W.; Moscou, L.; Pierotti, R. A.; Rouquerol, J.; Siemieniewska, T., Reporting Physisorption Data for Gas Solid Systems with Special Reference to the Determination of Surface-Area and Porosity (Recommendations 1984). *Pure and Applied Chemistry* **1985,** *57* (4), 603-619.
83. Cestari, A. R.; Airoldi, C., A New Elemental Analysis Method Based on Thermogravimetric Data and Applied to Alkoxysilane Immobilized on Silicas. *Journal of Thermal Analysis* **1995,** *44* (1), 79-87.
84. Hohne;, G. W. H.; Hemminger;, W. F.; Flammersheim, H.-J., *Differential Scanning Calorimetry*. Second ed.; Springer-Verlag: New York, 2003; Vol. 1, p 298.
85. Meyer, D. E.; Meeks, N.; Sikdar, S.; Hutson, N. D.; Hua, D.; Bhattacharyya, D., Copper-doped silica materials silanized with bis-(triethoxy silyl propyl)-tetra sulfide for mercury vapor capture. *Energy & Fuels* **2008,** *22* (4), 2290-2298.
86. Cestari, A. R.; Airoldi, C., Chemisorption on thiol-silicas: Divalent cations as a function of pH and primary amines on thiol-mercury adsorbed. *J Colloid Interf Sci* **1997,** *195* (2), 338-342.
87. Aguado, J.; Arsuaga, J. M.; Arencibia, A., Adsorption of aqueous mercury(II) on propylthiol-functionalized mesoporous silica obtained by cocondensation. *Ind Eng Chem Res* **2005,** *44* (10), 3665-3671.
88. Meyer, D. E.; Sikdar, S. K.; Hutson, N. D.; Bhattacharyya, D., Examination of sulfur-functionalized, copper-doped iron nanoparticles for vapor-phase mercury capture in entrained-flow and fixed-bed systems. *Energy & Fuels* **2007,** *21* (5), 2688-2697.
89. (a) Bustard, J.; Durham, M.; Starns, T.; Lindsey, C.; Martin, C.; Schlager, R.; Baldrey, K., Full-scale evaluation of sorbent injection for mercury control on coal-fired power plants. *Fuel Process Technol* **2004,** *85* (6-7), 549-562; (b) Jones, A. P.; Hoffmann, J. W.; Smith, D. N.; Feeley, T. J.; Murphy, J. T., DOE/NETL's phase II mercury control technology field testing program: Preliminary economic analysis of activated carbon injection. *Environmental Science & Technology* **2007,** *41* (4), 1365-1371.
90. Senior, C.; Bustard, C. J.; Durham, B.; Baldrey, K.; Michaud, D., Characterization of fly ash from full-scale demonstration of sorbent injection for mercury control on coal-fired power plants. *Fuel Process Technol* **2004,** *85* (6-7), 601-612.
91. Christy, A. A.; Egeberg, P. K., Quantitative determination of surface silanol groups in silicagel by deuterium exchange combined with infrared spectroscopy and chemometrics. *Analyst* **2005,** *130* (5), 738-744.
92. Haynes, J. S.; Sams, J. R.; Thompson, R. C., Synthesis and Structural Studies of Iron(Ii) and Iron(Iii) Sulfonates. *Can J Chem* **1981,** *59* (4), 669-678.
93. Ulman, A.; Yee, C.; Kataby, G.; Prozorov, T.; White, H.; King, A.; Rafailovich, M.; Sokolov, J.; Gedanken, A., Self-assembled monolayers of alkanesulfonic and -phosphonic acids on amorphous iron oxide nanoparticles. *Langmuir* **1999,** *15* (21), 7111-7115.
94. Subramanian, P.; Clark, N. B.; Spiccia, L.; MacFarlane, D. R.; Winther-Jensen, B.; Forsyth, C., Vapour phase polymerisation of pyrrole induced by iron(III) alkylbenzenesulfonate salt oxidising agents. *Synthetic Met* **2008,** *158* (17-18), 704-711.

95. Bukur, D. B.; Lang, X. S., Highly active and stable iron Fischer-Tropsch catalyst for synthesis gas conversion to liquid fuels. *Industrial & Engineering Chemistry Research* **1999,** *38* (9), 3270-3275.
96. Nath, M.; Satishkumar, B. C.; Govindaraj, A.; Vinod, C. P.; Rao, C. N. R., Production of bundles of aligned carbon and carbon-nitrogen nanotubes by the pyrolysis of precursors on silica-supported iron and cobalt catalysts. *Chem Phys Lett* **2000,** *322* (5), 333-340.
97. Wielers, A. F. H.; Kock, A. J. H. M.; Hop, C. E. C. A.; Geus, J. W.; Vanderkraan, A. M., The Reduction Behavior of Silica-Supported and Alumina-Supported Iron Catalysts - a Mossbauer and Infrared Spectroscopic Study. *J Catal* **1989,** *117* (1), 1-18.
98. Bukur, D. B.; Lang, X.; Mukesh, D.; Zimmerman, W. H.; Rosynek, M. P.; Li, C. P., Binder Support Effects on the Activity and Selectivity of Iron Catalysts in the Fischer-Tropsch Synthesis. *Industrial & Engineering Chemistry Research* **1990,** *29* (8), 1588-1599.
99. Varma, R. S.; Hoag, G. E.; Collins, J. B.; Holcomb, J. L.; Hoag, J. R.; Nadagouda, M. N., Degradation of bromothymol blue by 'greener' nano-scale zero-valent iron synthesized using tea polyphenols. *J Mater Chem* **2009,** *19* (45), 8671-8677.
100. Liu, J. C.; He, F.; Gunn, T. M.; Zhao, D. Y.; Roberts, C. B., Precise Seed-Mediated Growth and Size-Controlled Synthesis of Palladium Nanoparticles Using a Green Chemistry Approach. *Langmuir* **2009,** *25* (12), 7116-7128.
101. De Corte, S.; Hennebel, T.; Fitts, J. P.; Sabbe, T.; Bliznuk, V.; Verschuere, S.; Van der Lelie, D.; Verstraete, W.; Boon, N., Biosupported bimetallic Pd--Au nanocrystals for dechlorination of environmental contaminants. *Environ Sci Technol* **2011**.
102. (a) Varma, R. S.; Nadagouda, M. N., Green synthesis of Ag and Pd nanospheres, nanowires, and nanorods using vitamin B(2): Catalytic polymerisation of aniline and pyrrole. *J Nanomater* **2008**; (b) Varma, R. S.; Nadagouda, M. N.; Polshettiwar, V., Self-assembly of palladium nanoparticles: synthesis of nanobelts, nanoplates and nanotrees using vitamin B(1), and their application in carbon-carbon coupling reactions. *J Mater Chem* **2009,** *19* (14), 2026-2031.
103. (a) Kitajima, N.; Fukuzumi, S.; Ono, Y., Formation of Superoxide Ion during Decomposition of Hydrogen-Peroxide on Supported Metal-Oxides. *Journal of Physical Chemistry* **1978,** *82* (13), 1505-1509; (b) Lin, S. S.; Gurol, M. D., Catalytic decomposition of hydrogen peroxide on iron oxide: Kinetics, mechanism, and implications. *Environmental Science & Technology* **1998,** *32* (10), 1417-1423.
104. Yeh, C. K.-J.; Chen, W.-S.; Chen, W.-Y., Production of hydroxyl radicals from the decomposition of hydrogen peroxide catalyzed by various iron oxides at pH 7. *Practice Periodical of Hazardous, Toxic, and Radioactive Waste Management* **2004,** *8* (3).
105. Miller, C. M.; Valentine, R. L., Hydrogen-Peroxide Decomposition and Quinoline Degradation in the Presence of Aquifer Material. *Water Res* **1995,** *29* (10), 2353-2359.
106. Watts, R. J.; Jones, A. P.; Chen, P. H.; Kenny, A., Mineral-catalyzed Fenton-like oxidation of sorbed chlorobenzenes. *Water Environment Research* **1997,** *69* (3), 269-275.

107. Doyle, F. M.; Pham, A. L. T.; Lee, C.; Sedlak, D. L., A Silica-Supported Iron Oxide Catalyst Capable of Activating Hydrogen Peroxide at Neutral pH Values. *Environ Sci Technol* **2009,** *43* (23), 8930-8935.

Vita

Noah Daniel Meeks was born August 6, 1983, in Lexington, Kentucky. He grew up in Fairmount, Indiana, and graduated from Madison Grant High School, class of 2001. He received B.S. in chemistry (cum laude) from Northern Kentucky University, Highland Heights, Kentucky, in May 2005. In August 2005, he began graduate school in chemical engineering at University of Kentucky, under the direction of Dr. Dibakar Bhattacharyya (Alumni Professor of Chemical Engineering).

Publications:

Meeks, N.D., Rankin, S., Bhattacharyya, D. "Sulfur Functionalization of Porous Silica Particles and Application to Mercury Vapor Sorption" *Ind Eng Chem Res* **2010**, *49*, 4687–4693

Meyer, D.E., Meeks, N., Sikdar, S., Hutson, N.D., Hua, D., Bhattacharyya, D. "Copper-Doped Silica Materials Silanized with Bis-(Triethoxy Silyl Propyl)-Tetra Sulfide for Mercury Vapor Capture" *Energy & Fuels* **2008**, *22* (4), 2290-2298

Meeks, N.D., Stevens, C., Bhattacharyya, D. "Iron Nanoparticles for Toxic Organic Degradation" submitted to *Industrial and Engineering Chemistry Research*

Meeks, N.D., Davis, E., Bhattacharyya, D. "Aqueous Mercury Sorption and Regeneration Using a Novel Metal Oxide-Carbon Sorbent and Mixed Matrix Membranes" submitted to *Environmental Progress & Sustainable Energy*

Selected Presentations:

Noah D. Meeks, D. Bhattacharyya. "Silica-Polymer Mixed Matrix Membranes for Mercury and Silver Sorption" **AIChE Annual Meeting 2011**, Minneapolis

Noah D. Meeks, Vasile Smuleac, Chris Stevens and D. B. Bhattacharyya. "Synthesis of Metal Nanoparticles in Various Platforms for Detoxification of Chloroorganics From Water" **AIChE Annual Meeting 2010**, Salt Lake City

Noah D. Meeks, V. Smuleac, S. Hampson, L. Ormsbee, L. Bachas, D. Bhattacharyya. "Reduction of Immobilized Metal Ions to Nanoparticles on Silica and other Platforms, for Dechlorination" **AIChE Annual Meeting 2009**, Nashville

Noah D. Meeks, D.E. Meyer, D. Bhattacharyya. "Functionalized Silica Particles for Mercury Vapor Sorption and Catalytic Nanoparticle Synthesis" **The 5th Sino-US Joint Conference of Chemical Engineering**, October 2009, Beijing, China

Noah D. Meeks, D.E. Meyer, D. Bhattacharyya. "Sulfur Functionalization of Non-Carbon Materials with Applications In Mercury Sorption" **AIChE Annual Meeting 2008**, Philadelphia

Noah D. Meeks, D.E. Meyer, D. Bhattacharyya. "Synthesis and Characterization of Sulfur-Functionalized Amorphous Mesoporous Silica Particles" **AIChE Annual Meeting 2007**, Salt Lake City

Leadership, Service, & Professional Associations:

UK Engineering Residential College Mentor	2007-2011
UK Chemical & Materials Graduate Student Association	
President	2008-2011
Engineering Student Council Rep	2005-2008
UK University Appeals Board Member	2007-2010
UK Graduate Student Council	
Vice President	2009-2010
Interdisciplinary Conference Chairman	2008, 2009
UK Student Government, *Grad Student Rep*	2007-2009
American Institute of Chemical Engineers, Member	2005-present
Separations and Environmental Divisions, Member	2006-present
Virtual Local Section	
Director & Young Professionals Chair	2011-present
Society for Biological Engineering, Member	2009-present
Nanoscale Science and Engineering Forum, Member	2010-present
American Chemical Society, Member	2005-present

Awards:

Kentucky Research Challenge Trust Fellow	2005-2006
Chemical & Materials Engineering Dept Poster Session	
Materials & Energy Division Winner	2011